DOCTORAL THESIS

Predictive modelling of gas assisted electron and ion beam induced etching and deposition

A thesis submitted in fulfilment of the requirements
for the degree of Doctor of Philosophy

School of Physics and Advanced Materials
University of Technology Sydney

Author
Alan Stephen BAHM

Supervisors
Prof. Milos TOTH
Associate Prof. Michael FORD

July 2016

Certificate of Original Authorship

I, Alan Stephen BAHM, certify that the work in this thesis titled, 'Predictive modelling of gas assisted electron and ion beam induced etching and deposition' has not previously been submitted for a degree nor has it been submitted as part of requirements for a degree except as fully acknowledged within the text.

I also certify that the thesis has been written by me. Any help that I have received in my research work and the preparation of the thesis itself has been acknowledged. In addition, I certify that all information sources and literature used are indicated in the thesis.

Signature of Student:

Date: 28 July 2016

Acknowledgements

The work presented in this dissertation was carried out under the supervision of Prof. Milos Toth and Prof. Michael Ford, at the Microstructural Unit, Faculty of Science, University of Technology Sydney, New South Wales, Australia. The work was performed within the Advanced Technology Group, Beam Technology R&D, FEI Company, Hillsboro, Oregon, U.S.A.

I am extremely grateful to FEI Company for making this work possible through its financial and scientific support. Dr. Michael Lysaght supported this work through the ups and downs of business cycles. Dr. Mark Utlaut and Dr. Mostafa Maazouz envisioned the collaboration. Greg Schwind's support and flexibility helped greatly. Dr. Lynwood Swanson was an inspiring mentor who demonstrated how to approach rigorous research. Dr. Mostafa Maazouz first engaged me in simulation of FIB surface evolution by allowing me to build on the research by Dr. Heung-Bae Kim on the level set method. I benefited from many useful discussions over the years with Dr. Mark Utlaut, Dr. Marcus Straw, Dr. Mostafa Maazouz and Dr. William Parker.

At the University of Technology Sydney (UTS), many people also made this research possible. I'm especially appreciative for my advisor, Prof. Milos Toth, who was key throughout the definition and focussing of the work, and also challenged me to improve. Prof. Michael Ford advised, acted as a sounding board and provided feedback. Collaborations and interactions with Prof. Charlene Lobo and Prof. Igor Aharonovich always improved the work at hand.

I would like to thank many remote collaborators including Dr. Branislav Radjenovic, Prof. David Chopp, Prof. Ian Mitchell and Prof. Colin Macdonald for emails and discussions on etch interpolation models, level set method and closest point methods. Additionally valuable were discussions with Dr. Sloan Lindsey, Prof. Gerhard Hobler on ion-solid interactions as well as general discussions with Dr. Utlaut, Dr. Maazouz, Greg Schwind and Prof.dr.ir. Peter Kruit. I had a wonderful group of scientists and students to work with at FEI and UTS: my thanks to my co-authors Dr. Aurelian Botman, Dr. Steven Randolph, Dr. Aiden Martin, Dr. Marcus Straw, Dr. Chad Rue, Dr. Jared Cullen, Chris Badawi, Toby Shanley, and James Bishop.

I was truly lucky to have support from my family and friends. My wife 潘恒彦 (Heng-Yen Pan) and son William Bahm gracefully supported me through the upheaval in our family life over the last three and a half years. My parents and sister were loving and wonderfully supportive, as was

our adoptive family Joel Godbey, Kelly Morrow, Eric Miller and Missy Yungclas. Finally, a big thank you to Keith Wilson who gave me lab space in which to work, feedback and companionship.

Contributing Publications

Peer-reviewed publications that contributed to this work:

- Spontaneous Growth of Gallium-Filled Microcapillaries on Ion-Bombarded GaN, Aurelien Botman, **Alan Bahm**, Steven Randolph, Marcus Straw, and Milos Toth *Physical Review Letters* 111, 135503 - Published 25 September 2013
- Dynamic Pattern Formation in Electron-Beam-Induced Etching, Aiden A. Martin, **Alan Bahm**, James Bishop, Igor Aharonovich, and Milos Toth *Physical Review Letters* 115, 255501 - Published 18 December 2015

Non-Contributing Publications

Peer-reviewed publications not featured in this work containing research undertaken during the PhD program:

- Localized Probing of Gas Molecule Adsorption Energies and Desorption Attempt Frequencies, Jared Cullen, **Alan Bahm**, Charlene J. Lobo, Michael J. Ford, and Milos Toth, *Journal of Physical Chemistry C*, 2015, 119 (28), pp 15948-15953

Contents

Certificate of Original Authorship ii

Acknowledgements iii

Contributing Publications v

Non-Contributing Publications vi

List of Figures xi

List of Tables xiii

Abbreviations xv

Physical Constants xvii

Symbols xix

Abstract xxi

1 Motivation and background 1
- 1.1 What is EBIED / IBIED? . . . 1
- 1.2 Modelling of EBIED / IBIED with a gas precursor . . . 2
- 1.3 Experimental EBIED / IBIED . . . 3
- 1.4 Outline of thesis . . . 4

2 Gallium fluoride pillar modelling 5
- 2.1 Spontaneous growth of gallium-filled microcapillaries on ion-bombarded GaN . . . 6
- 2.2 Model implementation . . . 15
  - 2.2.1 Model results . . . 17
- 2.3 Self-ordering cycle . . . 19
- 2.4 Conclusions . . . 22

3 Surface evolution modelling 23
- 3.1 Dynamic pattern formation in electron beam induced etching . . . 24
- 3.2 Level set method . . . 30
  - 3.2.1 Concept . . . 32

3.2.2 Reinitialization . . . 35
3.2.3 Non-convex Hamiltonian . . . 35
3.2.4 Discretization and choice of scheme . . . 35
3.2.5 Sparse field . . . 37
3.2.6 Fast marching method . . . 37
3.2.7 Extension velocity . . . 38
3.3 Implementation and verification . . . 38
3.4 Diamond etch model implementation . . . 40
3.4.1 Etch rate anisotropy . . . 40
3.4.2 Simulation verification . . . 41
3.4.3 Determination of anisotropic etch rates . . . 43
3.5 Conclusions . . . 44

4 Adsorbate kinetics modelling **45**
4.1 EBIED / IBIED PDE definition . . . 46
4.2 Techniques for solving PDEs on surfaces . . . 47
4.2.1 Explicit surface techniques . . . 47
4.2.2 Implicit surface techniques . . . 47
4.2.3 The closest point method technique . . . 48
4.2.4 Other applications of CPM . . . 48
4.2.5 Recent developments with CPM . . . 48
4.3 Closest point method . . . 49
4.4 Implementation and verification of CPM . . . 51
4.4.1 Implementation of diffusion . . . 54
4.4.2 Implementation of sources and sinks . . . 54
4.5 Simulating adsorbate deposition . . . 56
4.5.1 Steady state assumption . . . 57
4.5.2 Deriving closest points on implicit surface from ϕ . . . 57
4.5.3 Ghost widths . . . 58
4.5.4 Results . . . 61
4.6 Conclusions . . . 63

5 General conclusions and future directions **65**
5.1 Including sample interactions . . . 65
5.2 Conclusions . . . 67

A Ion solid interactions modelling **69**
A.1 Overview . . . 70
A.2 Ion solid collision theory . . . 71
A.2.1 Total stopping . . . 71
A.2.2 Electronic stopping . . . 72
A.2.3 Nuclear stopping . . . 75
A.2.4 Classical scattering event . . . 75

A.2.4.1 Derivation of kinetic energy as a function of scattering angle . 76
A.2.4.2 Derivation of scattering integral . . . 79
A.2.4.3 Screened coulomb potential . . . 80
A.2.4.4 Implications of mass mismatch . . . 80
A.3 Binary collision algorithm . . . 81
A.3.1 Biersack's "scattering triangle" . . . 83
A.3.2 Implementation . . . 85
A.3.3 Validation and Results . . . 86
A.3.3.1 Flat surfaces . . . 88
A.3.3.2 Curved surfaces . . . 89
A.4 Conclusions . . . 90

B Framework for EBIED / IBIED adsorbate continuum equations 93
B.1 Species i . . . 94
B.2 Species concentration N . . . 94
B.3 Flux of electrons, ions, and neutrals . . . 96
B.4 Transport $\mathcal{T}$ . . . 98
B.5 Addition $\mathcal{A}$ . . . 100
B.5.1 Adsorption . . . 100
B.5.2 Thermal dissociation . . . 101
B.5.3 Stimulated dissociation . . . 102
B.5.4 Fragment combination . . . 103
B.5.5 Thermal chemisorption . . . 103
B.5.6 Stimulated chemisorption . . . 103
B.5.7 Redeposition of sputtered material . . . 104
B.5.8 Volume evolution . . . 104
B.5.9 Total addition . . . 104
B.6 Removal $\mathcal{R}$ . . . 104
B.6.1 Thermal desorption . . . 105
B.6.2 Stimulated desorption . . . 105
B.6.3 Associative desorption . . . 105
B.6.4 Fragment combination . . . 106
B.6.5 Thermal dissociation . . . 106
B.6.6 Stimulated dissociation . . . 106
B.6.7 Thermal etching . . . 106
B.6.8 Stimulated etching . . . 107
B.6.9 Thermal chemisorption . . . 107
B.6.10 Stimulated chemisorption . . . 107
B.6.11 Sputtering . . . 107
B.6.12 Consumption in surface reactions . . . 107
B.6.13 Total removal . . . 108
B.7 Conclusions . . . 108

C Modelling code 109

D Arrhenius form **111**

Bibliography **113**

List of Figures

1.1 EBIED and IBIED surface schematic 1

2.1 Ga droplets and GaF pillars 8
2.2 Growth of a pillar 9
2.3 Evolution of pillar geometry and material distribution 10
2.4 Cross-sectional compositional maps 11
2.5 Coalescence of pillar caps 11
2.6 Gallium concentration on substrate 14
2.7 Numerical implementation of the model 16
2.8 Sheath volume calcuation 18
2.9 Example model output 20
2.10 Self-ordering cycle schematic 21

3.1 Pattern formation by H_2O on diamond 26
3.2 Pattern formation by NH_3 on diamond 28
3.3 Temperature dependence of EBIE rate 29
3.4 Level set image segmentation 31
3.5 Level set method publications 31
3.6 Illustration of level set in two dimensions 33
3.7 Non-convex Hamiltonian from sputter yield 36
3.8 Level set implementation verification convex scheme 39
3.9 Level set implementation verification non-convex scheme 40
3.10 Etch rate regions 41
3.11 Etching of spheres and voids 42
3.12 Diamond etching scheme 44

4.1 Illustration of locally oriented basis on surface 50
4.2 Role of Cartesian points in the closest point method 51
4.3 Illustration of closest point operator on local grid 52
4.4 Illustration of L and G bands 53
4.5 Sparse matrices of the closest point method 54
4.6 Stabilization of M matrix 55
4.7 Demonstration of heat diffusion 56
4.8 Demonstration of adsorbate diffusion 57
4.9 Demonstration of adsorbate diffusion 58
4.10 Illustration of CPM-LSM improvement by reinitialization domain 59

4.11 Illustration of ghost width for CPM initialization from ϕ 60
4.12 Illustration of mass transfer limited surface evolution 2D 62
4.13 Illustration of mass transfer limited surface evolution 3D 64

5.1 Computing sample interaction, adsorbate kinetics and surface evolution 66

A.1 Ion solid interactions 71
A.2 Nuclear, electronic and total stopping cross sections 72
A.3 Silicon stopping cross sections 73
A.4 Silicon stopping cross section models 74
A.5 Scattering event 76
A.6 Lab and centre of mass reference frames 78
A.7 Screened potentials 81
A.8 Implications of mass mismatch 82
A.9 Definition of scattering triangle 85
A.10 Comparison of scattering approaches 86
A.11 Example trajectories in 3D 87
A.12 Sputter yield agreement 88
A.13 Example cascades 89
A.14 Sputter yields on hemicylinders 90
A.15 Sputter yields on hemispheres 91

B.1 Map of surface processes 95
B.2 Elemental surface interactions 99
B.3 Elemental surface interactions (continued) 100
B.4 Reaction-coordinate diagram across potential barrier 102

D.1 Boltzmann distributions 111

List of Tables

2.1 Sheath volume calculation 19

3.1 Simulation etch rates 43

C.1 Simulation code statistics 110

Abbreviations

API	Application Programming Interface
BCA	Binary Collision Algorithm
BET	Brunauer-Emmett-Teller theory
BDF	Backwards Difference Formula
CM	Centre of Mass
CPM	Closest Point Method
CPU	Central Processing Unit
EBIE	Electron Beam Induced Etching
EBIED	Electron Beam Induced Etching and Deposition
EDS	Energy Dispersive X-ray Spectroscopy
FEM	Finite Element Methods
FMM	Fast Marching Method
FVM	Finite Volume Methods
GIS	Gas Injection System
GPU	Graphics Processing Unit
FIB	Focused Ion Beam
HJE	Hamilton-Jacobi Equation
iSE	Ion Generated Secondary Electrons
ISM	Ion-Solid-Modelling
ITK	Insight Segmentation and registration Toolkit
IBIED	Ion Beam Induced Etching and Deposition
LLF	Local-Lax-Friedrichs
LF	Lax-Friedrichs

LSM	Level Set Method
MC	Monte Carlo
MD	Molecular Dynamics
MTL	Mass Transport Limited
PDE	Partial Differential Equation
RD	Reaction Diffusion
SEM	Scanning Electron Microscope
SIMD	Single Instruction Multiple Data
SRIM	Stopping and Range of Ions in Matter (software program)
TEM	Transmission Electron Microscope
TRIM	Transport and Range of Ions in Matter (software program)
TRIDYN	Transport of Ions (Dynamic)
UV	Ultraviolet
1D	One Dimensional
2D	Two Dimensional
3D	Three Dimensional

Physical Constants

Bohr radius	a_0	$=$	5.291 772 109... $\times 10^{-11}$ m
Electron rest mass	m_e	$=$	9.109 382 15... $\times 10^{-31}$ kg
Vacuum permittivity	ϵ_0	$=$	8.854 187 817... $\times 10^{-12}$ F/m
Pi	π	$=$	3.14159...
Euler's number	e	$=$	2.71828...

Symbols

R^3	real coordinate space of three dimensions
∇	gradient
∇^2 or Δ	Laplacian a.k.a. Laplace operator
∇_S	intrinsic gradient
∇_S^2 or Δ_S	intrinsic Laplacian a.k.a. Laplace-Beltrami operator
Δ	discrete difference
∂x	partial derivative of x
dx	total derivative of x
$t \to 0$	"as t goes to zero"
$\boldsymbol{x}, \boldsymbol{v}, \boldsymbol{n}, \boldsymbol{t}$	vector position, velocity, normal, tangent
κ	curvature
ϕ_t	time derivative of ϕ
$\hat{H}$	exact Hamiltonian
H	discretized approximation of the Hamiltonian
max	maximum
$O(N)$	big O notation
$F_{ext}(\phi = 0) = F$	"extension velocity at $\phi = 0$ is F"
log	logarithm base 10
ln	natural logarithm
$\approx$	approximately equal to
$\equiv$	definition
cos, tan, cot	cosine, tangent, cotangent function
$cp()$	closest point operator

Abstract

While the field of experimental micrometre scale EBIED / IBIED ("electron beam chemistry" or "ion beam chemistry") has been growing in recent years, the 3D simulation of these systems at real scales has been non-existent. This type of simulation is important for it is only in three dimensions that interesting asymmetric and patterning phenomena can be tracked.

There are a couple of difficulties in these types of simulations. One is solving the diffusion of adsorbate concentrations in the system. Accurate simulation of diffusion on general 2D surfaces is non-trivial, (even on 1D curves), and can require unnatural re-parametrization of the surface (re-meshing). Another difficulty is that simulations have generally been atomistic and limited in scale. The key to providing large scale 3D simulations comes from applying new, mathematically robust, computer-science methods based on implicit surfaces to this field.

In this thesis, the issues above are addressed in a couple of different ways. In one case, diffusion over a complex surface was reduced to piecewise axially symmetric equations. Later, implicit methods for solving adsorbate kinetics continuum equations and evolving the surface are implemented, the closest point method and the level set method respectively. The development of the tools themselves is a non-trivial exercise as there are few software libraries for the level set method and none for the closest point method. These tools were then used independently to simulate etching and diffusion, as well as in concert to demonstrate the ability to simulate 3D deposition in the mass transport limited and reaction rate limited regimes.

Chapter 1

Motivation and background

1.1 What is EBIED / IBIED?

Electron and ion beam induced etching and deposition (EBIED and IBIED) are a set of techniques which can modify a substrate with high spatial resolution by a charged particle beam incident onto a substrate in the presence of an adsorbate gas, see Figure 1.1.

Several physical processes are ongoing simultaneously in this system. An ion beam incident on the surface will result in a collision cascade which damages the bulk and causes sputtering from the surface. For an electron beam, damage and sputtering are often negligible. Lower energy

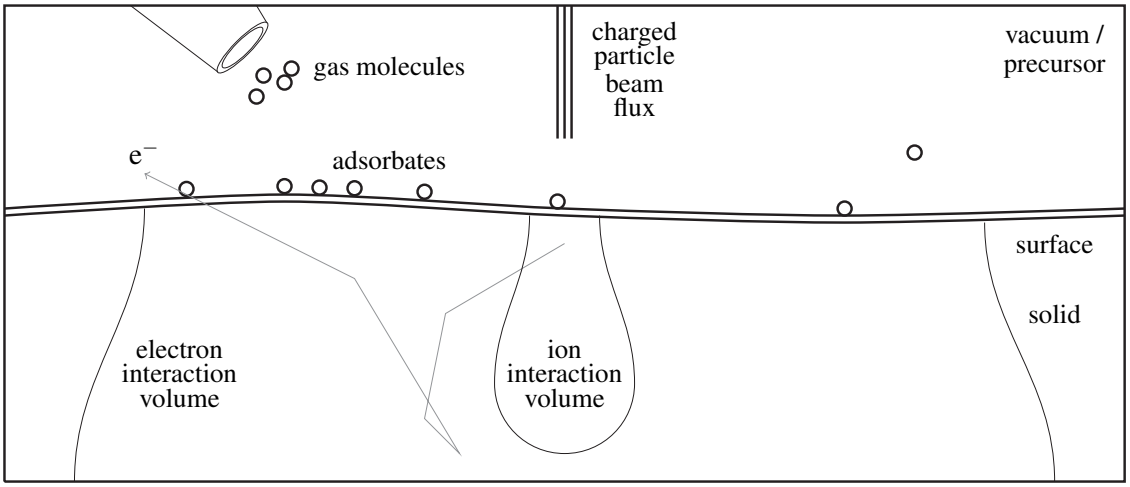

FIGURE 1.1: EBIED and IBIED surface schematic.

"secondary" electrons are generated in all cases, and can escape the solid if they are close enough to the vacuum-surface interface. Meanwhile, a gaseous precursor is delivered into the system. Molecules adsorb onto the surface, diffuse along the surface, and desorb from the surface back into the vacuum with some characteristic residence time. Depending on the adsorbate, a multitude of things can happen. Adsorbates might spontaneously etch the surface away or build up the surface. Additionally, adsorbates have an energy dependent interaction with a primary or secondary particle flux through the surface. In this interaction, the adsorbate might be fragmented into new species. The surface evolves as a net result of some or all of these EBIED / IBIED processes.

This entire set of processes is surface dependent. Depending on the shape of the surface: 1) adsorption, diffusion, and desorption can be affected, 2) ion-solid and electron-solid interactions will vary, and 3) surface evolution itself will be altered. Prior research provides no framework for modelling this in 3D over micrometre scales, as will be discussed in Section 1.2. This thesis will focus on the simulation of the surface physics and solving the fundamental problems of interaction, evolution, and diffusion which arise. The goal is to provide new tools for three dimensional micro scale simulation of electron and ion beam chemistry.

1.2 Modelling of EBIED / IBIED with a gas precursor

Modelling literature of adsorbate kinetics and surface evolution in EBIED and IBIED dates back to the 1980s.

For IBIED, generally only adsorbate kinetics or surface evolution was modelled. Many investigations treated adsorbate kinetics as a steady-state coverage model [1–11], or assumed coverage was uniform and unity [12, 13]. Surface evolution by the level set method for ion beam sputtering was modelled by [14, 15].

For EBIED, a dynamic Monte Carlo simulation was used to track deposits in 2D [16–18] and 3D [19, 20] and eventually added adsorbate diffusion by tracking atomic hops over a nanometre sized area. Another approach developed was to track coverage [21, 22] and then concentration over the surface [23–27], sometimes tracking two populations of adsorbate [23, 25, 28–30]. Modelling of both adsorbate kinetics and surface evolution by a hybrid continuum and Monte Carlo model [31, 32] were two-dimensional, relying on axial symmetry.

Modelling concepts have been shared by EBIED and IBIED, advancing both. But neither supports the larger (micro) scale 3D continuum models. This capacity would be useful both because it is on the scale of the experiment, but also because 3D is interesting when exploring patterns and asymmetric phenomena. This work applies new techniques to overcome this limitation, and demonstrates that general surfaces and evolving surfaces can be simulated in concert with modelling electron / ion solid interactions and solving the adsorbate continuum equation to steady state.

1.3 Experimental EBIED / IBIED

Experimental research in EBIED / IBIED is very active and productive. A number of different interesting effects and results have been published since 2008, all depending on adsorbate kinetics driven by electron or ion beams. New 3D pattern formation effects include: pattern formation induced by ion beam driven atomic surface currents [33], ordered nanodroplets [34], pillar growth [35], and pyramidal pits [36]. New physical effects include activated chemisorption [30]. Further control of surface changes include: patterned Pt deposits by activated chemisorption [37], nitrogen vacancy (NV) charge state switching by fluorination of H-terminated diamond [38] and nanosynthesis by pulsed electron beam which tunes deposition between two adsorbates with differing electron impact cross-sections [39].

Electron beam induced deposition (EBID) is a room temperature, direct-write nanofabrication technique that requires only a single processing step [40]. It has been used to fabricate nanoscale 3D plasmonic helix arrays [41], optical nanoantennas [42, 43], nano-scale tunneling electrodes [44], magnetic nanowires [45], catalytic seeds for site-specific growth of nanowires [46], and electrodes for controlling domain wall motion in ferroelectric films [47].

Gas-mediated electron beam-induced etching (EBIE) is a direct-write, subtractive nanofabrication technique in which an electron beam and a precursor gas are used to realize chemical dry etching with a spatial resolution of ≈ 10 nm. EBIE is typically performed using electron microscopes that are equipped with gas injectors and enable in situ imaging and analysis of the features fabricated by an electron beam. Historical overviews and reviews of the EBIE technique and the underlying

chemical pathways can be found in references [18, 25, 40, 48, 49]. Recently, EBIE has been used for engineering quantum emitters in hexagonal boron nitride (hBN) [50].

IBIED uses a focused ion beam to process the substrate allowing for implantation of defects, doping, deposition, stress induced bending, milling, and gas-enhanced etching, [51–56]. All these processes make IBIED a great tool for constructing micro- and nano-scale structures.

1.4 Outline of thesis

This thesis presents new contributions to modelling in gas assisted ion and electron situations, with a focus on surface evolution and surface diffusion. Chapter 2 describes the first example of a Focused Ion Beam (FIB) chemistry process driven by self-assembly producing gallium pillars, and solves the problem of surface evolution and diffusion in an elegant, efficient way that exploits the symmetry of this novel system. Chapter 3 reviews the implementation of a state-of-the-art generic surface evolution algorithm that is topologically robust and 3D and demonstrates the technique of applying this implicit surface method to track evolution in the case of electron beam etching of diamond. Chapter 4 incorporates a reaction-diffusion partial differential equation (PDE) solver with the surface evolution method of Chapter 3 and final results are presented with this new state-of-the-art EBIED / IBIED modelling method. Finally, conclusions and future directions are presented in Chapter 5.

Chapter 2

Gallium fluoride pillar modelling

This chapter reviews the first known focused ion beam (FIB) chemistry process which is driven by self-assembly, and the gallium concentration diffusion model which tracks the growth kinetics. Here surface diffusion is complicated by the geometries involved, and is solved by division of the simulation surface into two well-chosen surfaces with simple coordinate systems. Boundary conditions were chosen so that the two diffusion equations are coupled together, driving evolution of the pillar.

In 2013, Botman, Bahm, et al. published *Spontaneous growth of gallium-filled microcapillaries on ion-bombarded GaN* [35]. All experimental work was performed by Aurelien Botman. The first analytic model of the growth kinetics, (2.1) created by Milos Toth, approximated the growth deceleration. Alan Bahm defined and implemented a more exact model which simulates the evolution of Ga surface concentration (2.2), and is necessary to provide convincing evidence for the growth mechanism. This second, more exact model involved a implementation of diffusion across different geometries alongside a droplet and sheath volume tracking model. The result matched the experimental geometric measurements at both short and long times, and gave a reasonable estimate for the sheath density.

Section 2.1 is the publication [35] in its entirety. This gives the context, covers the background and experimental results, and includes portions of the experimental and theoretical work for conciseness. Section 2.2 covers the model implementation and its results in detail. Section 2.3 illustrates

the self-ordering process. Section 2.4 reviews this contribution and it's relationship to surface topics in this thesis.

2.1 Spontaneous growth of gallium-filled microcapillaries on ion-bombarded GaN: Published in [35]

Abstract of publication [35]: Bottom-up growth of microscopic pillars is observed at room temperature on GaN irradiated with a Ga^+ beam in a gaseous XeF_2 environment. Ion bombardment produces Ga droplets which evolve into pillars each comprised of a spherical Ga cap atop a Ga-filled, gallium fluoride tapered tube (sheath). The structures form through an interdependent, self-ordering cycle of liquid cap growth and solid sheath formation. The sheath and core growth mechanisms are not catalytic, but are instead consistent with a model of ion-induced Ga and F generation, Ga transport through surface diffusion, and heterogeneous sputtering caused by self-masking of the tapered pillars.

Emergent phenomena such as spontaneous pattern formation, self-assembly and self-organization [33, 34, 57–60] have stimulated much research into the underlying mechanisms and applications in bottom-up growth [59, 60] at length scales ranging from the atomic to macroscopic. Here we report a spontaneous, room temperature growth mechanism that yields microscopic pillars each comprised of a solid, tapered, gallium fluoride sheath and a Ga core that protrudes from the sheath and forms a liquid spherical cap at the pillar tip. The growth process was observed on GaN irradiated by a Ga^+ beam in a gaseous XeF_2 environment. Pillar growth is initiated by the formation of a spherical liquid Ga droplet and concurrent growth of a solid sheath, caused by chemical conversion of liquid Ga to gallium fluoride. Tapered pillars emerge from an interdependent, self-ordering cycle of Ga droplet (i.e., pillar cap) growth and sheath formation. The underlying mechanisms are non-catalytic and physically distinct from others reported in the literature, such as vapor-liquid-solid, solid-liquid-solid, and solution-liquid-solid growth [61].

It is well known that ion bombardment in vacuum of III-V semiconductors such as GaN [25, 62, 63], GaAs, InN, InAs, and InP can give rise to the formation of metallic droplets on the substrate surface [34, 64, 65]. Preferential sputtering of the group V element and ion beam induced decomposition and restructuring of the surface cause the group III species to accumulate [66–

69], and droplets to form through nucleation, growth and ripening mechanisms [34, 64, 65, 70]. In some instances, the droplets have very narrow size distributions, and can be ordered through spontaneous or directed processes such as off-normal ion irradiation [34] and pre-patterning of droplet nucleation sites [64].

Droplets generated by the irradiation of GaN in vacuum by a normal incidence, focused, rastered, 30 keV Ga^+ beam are shown in Figure 2.1(a-b). The droplets nucleate preferentially at surface steps (Figure 2.1(b)), consistent with a mechanism that involves diffusion and pinning at free-energy-minimising loci. In a gaseous XeF_2 environment, ion irradiation also gives rise to the formation of Ga droplets. However, the droplets act as nucleation sites for the formation of pillars that grow antiparallel to the ion beam. Figure 2.1(c-d) shows two frames from Supplementary Video 1, a movie produced by real time secondary electron imaging of the growth process.[1] The movie reveals that the droplets nucleate in random locations and that the growth of each individual pillar starts, decelerates and terminates spontaneously as the ion beam is scanned repeatedly over the substrate.

The observed pillar growth is highly atypical in that XeF_2 normally acts as a precursor for chemical etching of ion-irradiated substrates [25]. XeF_2 is also known to contribute to swelling caused by ion irradiation, and top-down (subtractive) structure formation caused by heterogeneous etching [63, 71]. Such processes are, however, clearly different from the pillar growth reported here.

The pillars in Figure 2.1(d) are aligned vertically, but distributed randomly along the substrate. Ordered arrays (Figure 2.1(e)) and individual pillars (Figure 2.2) can be fabricated by pre-patterning Ga droplet nucleation sites using the focused Ga^+ beam. The time-evolution of a single pillar is demonstrated in Figure 2.2 by 9 frames from Supplementary Video 2, a movie of the growth process. The images show (at 6 seconds): a hole that had been made by a stationary Ga^+ beam and acts as a droplet nucleation site; (at 6-31 seconds): droplet nucleation and growth occurring while the ion beam is scanned repeatedly over the rectangle seen in the images; (at 80-524 seconds): pillar formation; ($\sim$ 400 seconds): droplet nucleation at the edge of the scan rectangle; (at 400-554 seconds) pillar growth termination; and (at 554 seconds): droplet nucleation and growth observed to occur at the pillar base and the edge of the scan rectangle immediately after pillar growth has terminated. Figure 2.3(a) shows plots of the pillar cap diameter d_1, the corresponding volume V,

[1] For electron image movies of the growth process and detailed descriptions of the experimental methods, see the electronic publication `http://dx.doi.org/10.1103/PhysRevLett.111.135503`

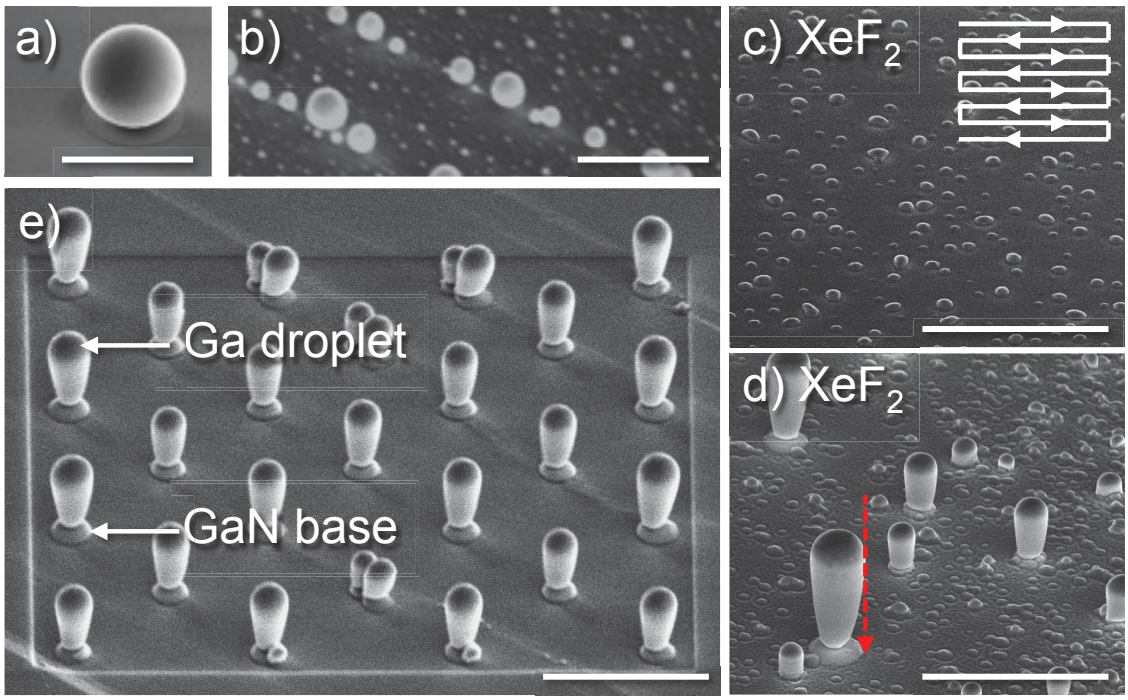

FIGURE 2.1: **(a-b)** Electron images of Ga droplets on GaN formed during ion beam irradiation in vacuum, and two frames from a movie of droplets **(c)** growing to form pillars **(d)** in XeF_2. **(e)** Pillar array grown on a pre-patterned GaN substrate. Each scale bar represents 5 μm. The ion beam was scanned in the serpentine pattern shown in (c).

and the pillar base diameter d_2 as a function of time (t). Vertical growth terminated at $\sim$ 530 seconds, where $\partial V/\partial t = 0$.

Pillar composition and internal structure were determined by cross-sectional electron imaging and energy dispersive x-ray spectroscopy (EDS). EDS maps of pillars that had been grown for 60, 420 and 1200 s are shown in Figure 2.4(a-c), where each time stamp corresponds to the growth time of a different pillar. Ga and F (but no Xe, N or O) were detected in the pillars. The maps show that each pillar is a Ga-filled, gallium fluoride microcapillary (i.e., a tapered fluorinated sheath). The most stable gallium fluoride stoichiometry is GaF_3 [72], which has a high melting point of 800°C, in contrast to that of Ga (30°C) which behaves as a supercooled liquid at room temperature. The Ga core extends beyond the sheath and forms a spherical Ga cap (shown in Figure 2.4(d)). The liquid nature of the Ga caps is illustrated by the image sequence in Figure 2.5 which shows the coalescence of two adjacent pillar caps into a single, asymmetric Ga droplet. The images also illustrate the high cohesive energy of Ga which is responsible for droplet formation.

Fluorine was detected only in the tapered sheaths (Figure 2.4(c)). The sheaths are present only

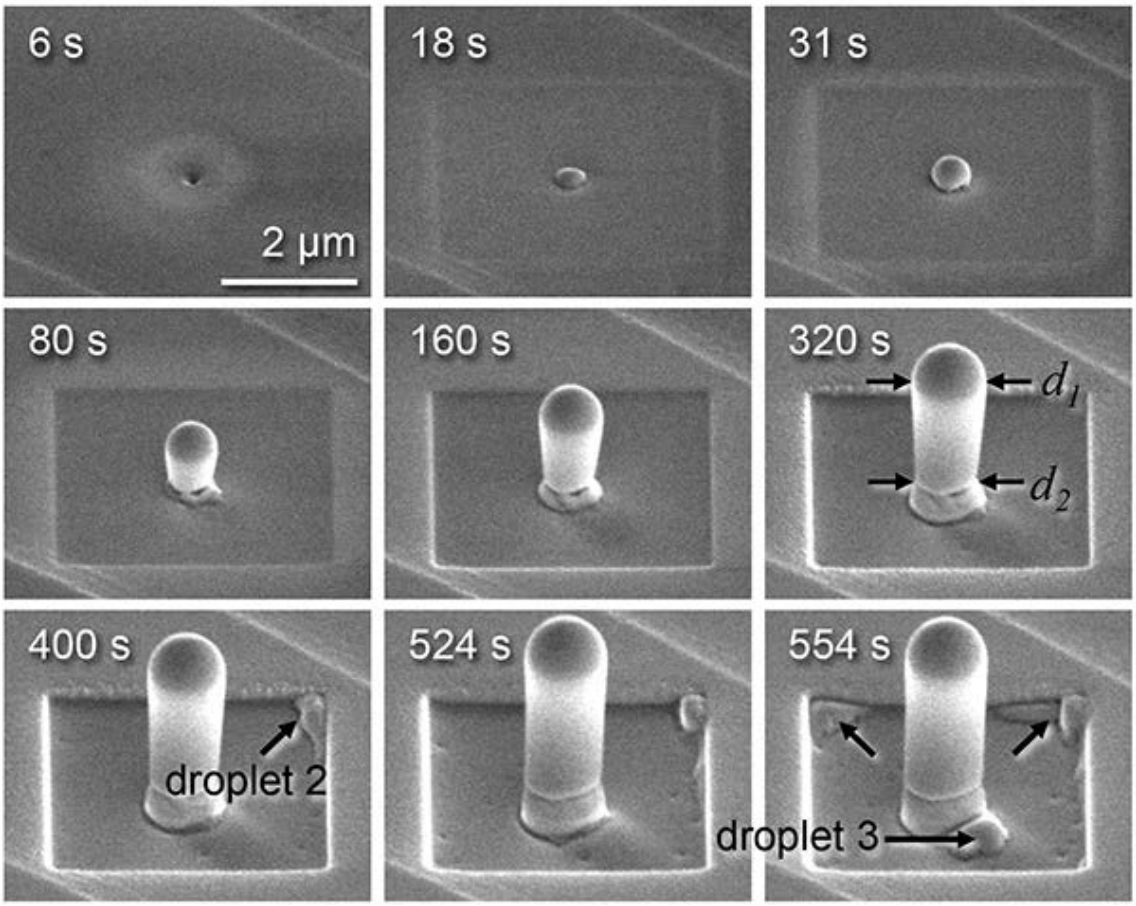

FIGURE 2.2: Electron image sequence showing the growth of a pillar and the formation of secondary Ga droplets.

in regions that were protected from sputtering through masking by the Ga caps, as indicated by an arrow in Figure 2.1(d). Masking also prevents sputtering of the underlying GaN substrate, resulting in the formation of the raised GaN features seen at the base of each pillar in Figure 2.1(e) and in Figure 2.4(c).

Figure 2.4(e) shows an EDS map of a pillar grown at the periphery of the rectangle scanned by the ion beam. The sheath is present only on the pillar surface that faces the scan rectangle, showing that the ion beam plays a direct role in sheath formation, and that F is immobile at length scales on the order of the pillar diameter. The map also shows that F is not entering the pillar from the gas phase (through the cap) and is not causing fluoride growth at the sheath-core interface through a vapor-liquid-solid mechanism.

The compositional maps in Figure 2.4 show how Ga droplets evolve into pillar caps and cores,

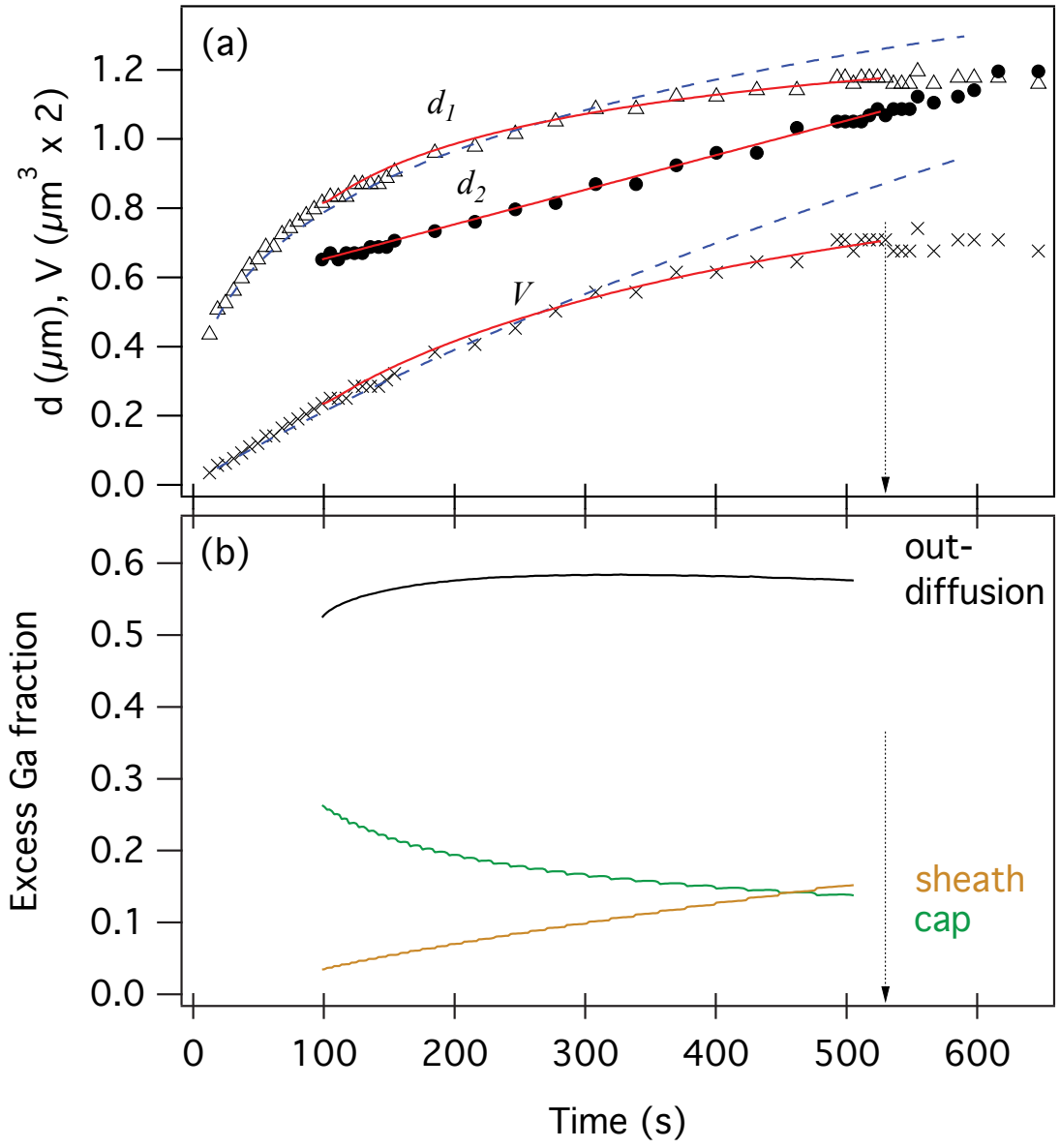

FIGURE 2.3: **(a)** Cap volume V ($\times$), cap diameter d_1 ($\triangle$) and pillar base diameter d_2 ($\bullet$) measured as a function of time, and corresponding curves calculated using (2.1) (- - - -) and (2.2) (——). **(b)** Fraction of excess Ga atoms diffusing into the the sheath, the cap and away from the pillar ('out-diffusion') calculated as a function of time. Vertical arrows show the time at which pillar growth terminated.

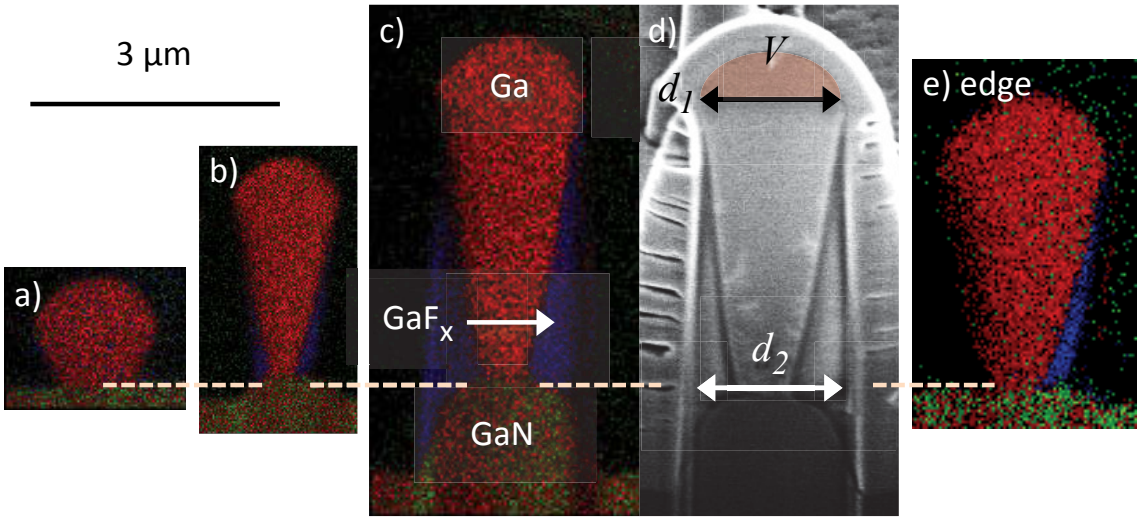

FIGURE 2.4: Cross-sectional compositional maps (Red = Ga, blue = F, green = N) of pillars that had been grown for **(a)** 60 s, **(b)** 420 s and **(c)** 1200 s, and **(d)** a secondary electron image of pillar (c). Map **(e)** shows a pillar grown at the edge of the area bombarded by Ga^+ ions. The dashed horizontal line shows the position of the GaN surface prior to ion irradiation. Each pillar is coated with a protective Pt film used to minimise cross-sectioning artifacts. The scale bar applies to all images.

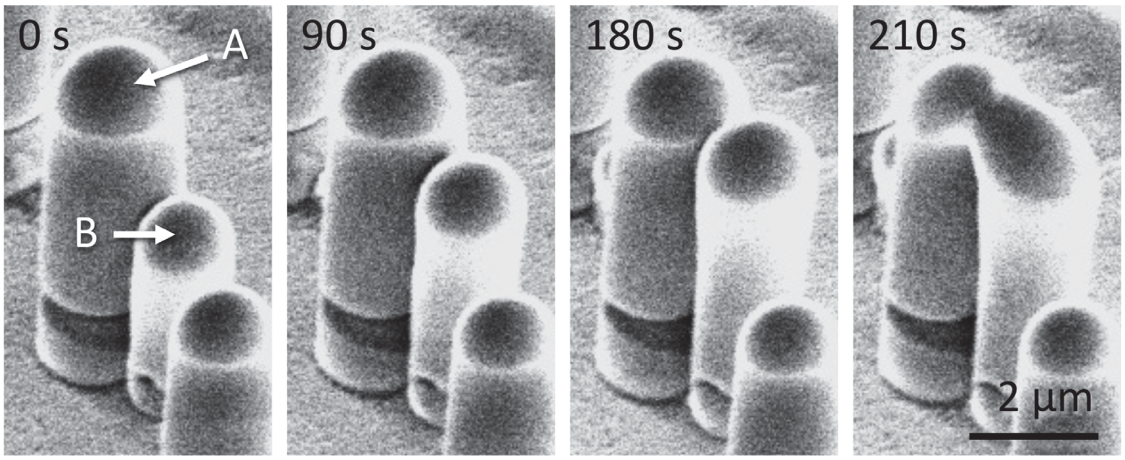

FIGURE 2.5: Image sequence showing a pillar (A) that has reached maximum height and is no longer growing, the growth of an adjacent pillar (B), and coalescence of the pillar caps into a single, asymmetric Ga droplet.

and how sheath formation is enabled by the sidewall taper which prevents sheath removal through sputtering. The maps also indicate how vertical pillars emerge from a cycle of cap growth and sheath formation. However, the maps do not explain the pillar growth kinetics. To elucidate the observed growth behaviour, we consider the isolated pillar imaged in Figure 2.2. The growth rates of the Ga cap volume (V) and diameter (d_1) decrease with time, while the pillar base diameter (d_2) scales linearly with time (see Figure 2.3(a)). This indicates that the growth is rate limited by the supply rate of Ga rather than fluorine. We therefore develop a model of growth kinetics based on excess Ga generation and consumption in the system.

In the limit of short growth times, the sheath volume is negligible, and we assume that (i) the excess Ga generation rate is proportional to the area of GaN that is bombarded by ions and acts as a source of excess Ga, (ii) a fixed fraction of the excess Ga flows into and is consumed by the pillar, which is located in the center of the Ga source, and (iii) Ga is removed from the cap through sputtering at a rate that is proportional to the cap surface area, A_s. We can therefore approximate the rate of change of the cap volume, $\partial V/\partial t$, by:

$$\frac{\partial V}{\partial t} \approx \frac{\partial V_0}{\partial t}\left(1 - \frac{A_{d1}(t)}{A_I}\right) - \frac{\partial \gamma}{\partial t} A_s(t) c, \tag{2.1}$$

where $\frac{\partial V_0}{\partial t}$ is $\frac{\partial V}{\partial t}$ in the limit $t \to 0$, A_I is the initial area of GaN irradiated by ions (i.e., the rectangle around the pillar seen in Figure 2.2), A_{d1} is the projected area of the growing Ga cap in the plane of A_I, and $\frac{A_{d1}}{A_I}$ is the fraction of A_I occupied by the growing cap. The excess Ga generation rate is proportional to $(1 - A_{d1}/A_I)$ because the Ga cap resides on top of the GaN substrate and masks it from ion irradiation. The last term, $\frac{\partial \gamma}{\partial t} A_s(t) c$, is the net volumetric Ga removal rate, expressed as a product of the flux of Ga sputtered from the cap, $\frac{\partial \gamma}{\partial t}$, $(\mathrm{atoms/m^2/s})$, A_s and the volume of a Ga atom, c.

$\frac{\partial V_0}{\partial t}$ was deduced experimentally from the slope of $V(t \to 0)$, seen in Figure 2.3(a), and $\frac{\partial \gamma}{\partial t}$ is a fitting parameter. Solutions to (2.1) yield the time-evolution of the cap volume $V(t)$ and the corresponding cap diameter $d_1(t)$. Figure 2.3(a) shows the best fit to experiment obtained by setting $\frac{\partial \gamma}{\partial t}$ to $10^7\ \mu m^{-2} s^{-1}$ which corresponds to a realistic sputter yield of ~ 11 (Ga atoms per ion incident onto the spherical cap). The calculated $V(t)$ profile is sub-linear due to two effects: (i) an increase in A_s which acts as a Ga sink, and (ii) a decrease in the size of the Ga source caused by the growth of A_{d1}. This simple time-evolution of the size of the Ga source and sink yields cap

growth kinetics that are in agreement with experiment at short growth times. However, the model overestimates the cap growth rate at long times. This divergence is hypothesized to be attributed to Ga consumption in sheath formation. The next model (2.2) includes this missing effect and successfully predicts cap growth rate at long times. Excess Ga is generated by ion irradiation of the GaN substrate and supplied to the cap through diffusion along the surface of the growing sheath. Hence, the fraction of Ga consumed in sheath formation and the Ga flow rate into the cap increases and decreases with time, respectively.

In order to account for sheath formation, we use (2.1) to define initial conditions for an explicit simulation of excess Ga generation, diffusion, consumption and removal from the system. Specifically, we calculate the time-dependent excess gallium concentration C across the sheath and the GaN substrate by solving:

$$\frac{\partial C}{\partial t} = a\widehat{f} - bC + D\nabla^2 C, \tag{2.2}$$

where a is the excess gallium generation coefficient (atoms per ion incident onto GaN), $\widehat{f}$ is the mean ion beam flux in the plane of the substrate, b is the Ga uptake rate by the sheath, and D is the Ga diffusion coefficient. The domain of (2.2) spans the substrate and the pillar (represented in two different coordinate systems). A detailed description of the model implementation is provided in Section 2.2.

Here (2.2) was solved numerically, using input parameters that are equivalent to those used in (2.1), and by using b as a fitting parameter. Figure 2.3(a) shows plots of d_1, d_2 and V calculated as a function of time. Part (b) of the figure shows corresponding plots of the fraction of excess Ga that is consumed by the sheath and the cap, and the fraction lost through out-diffusion (i.e., diffusion away from the region of GaN bombarded by Ga ions). The latter is approximately constant during growth, thereby validating assumption (ii) made in setting up (2.1).

The modelling data in Figure 2.3(a) are in excellent agreement with experiment, and were obtained by setting b to 1.1×10^6 s^{-1}, which yields a physically realistic sheath with a density that is approximately half that of single crystal GaF_3. Solutions to (2.2) consistently predict a peak in C on the GaN substrate, near the pillar base. This peak, shown in Figure 2.6, is in the vicinity of 'droplet 3' marked on Figure 2.2. Such droplets are often observed to nucleate immediately after pillar growth has terminated, and cause nucleation of neighbouring pillars, a number of which are

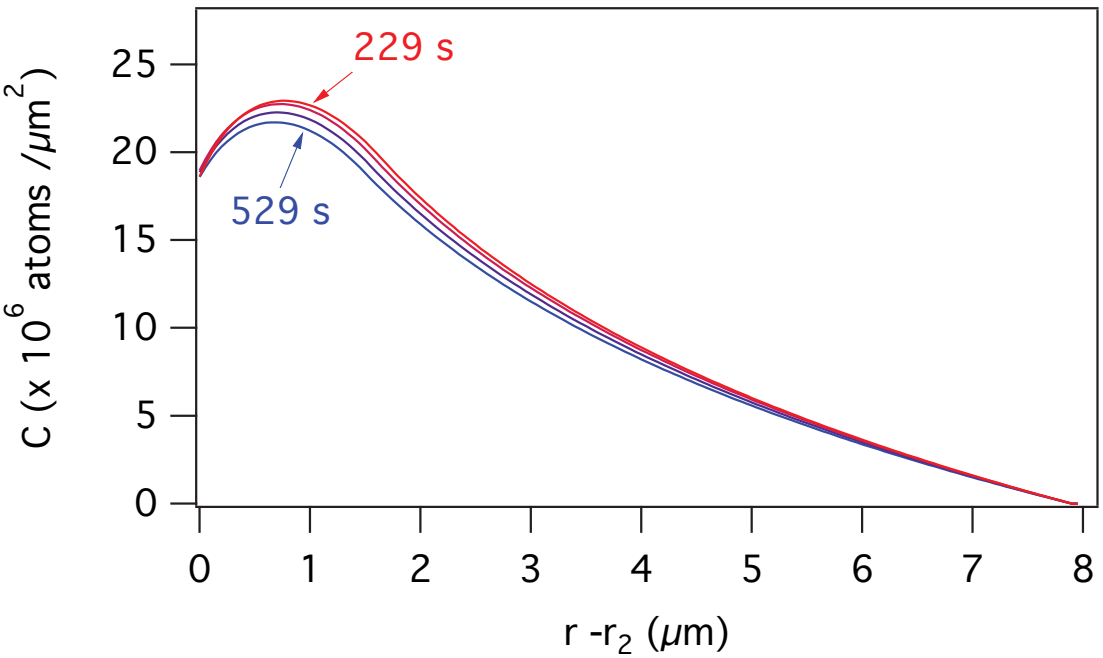

FIGURE 2.6: Excess Ga concentration (C) along the GaN substrate versus distance from the pillar base $(r - r_2)$, plotted for $t = 229$, 329, 429 and 529 s. $[r_2 = d_2/2]$

seen in Figure 2.1(e). The frequent nucleation of such droplets is likely caused by a combination of the elevated Ga concentration, and the presence of an asperity at the pillar base.

We can now combine the above experimental and simulation data to form a detailed picture of pillar growth. Liquid droplets form at the substrate, as in prior studies of III-V semiconductors performed in vacuum [34, 64, 65, 70]. XeF_2 gives rise to the formation of solid sheaths which deform the growing Ga droplets into the pillar cores seen in Figure 2.4. Pillars emerge through a self-ordering cycle of droplet growth and sheath formation, in which vertical growth occurs only when the cap diameter increases with time. Sheath formation is induced by ion bombardment of the GaN substrate. The absence of N (within the EDS detection limit) shows that the sheaths are not composed primarily of material that is sputtered from GaN and redeposited on the growing pillars. Instead, the most likely mechanism is (i) adsorption of XeF_2 gas molecules to the pillar sidewall, (ii) dissociation of the adsorbates by electrons [25] emitted from GaN due to ion impact, and (iii) formation of gallium fluoride through reactions between liquid gallium and fluorine adsorbates. The abruptness of the core-sheath interface seen in Figure 2.4(d) indicates that the sheath constituents are not soluble in Ga. Gallium is supplied through surface diffusion, and generated by ion beam decomposition of the GaN surface. The simulations show that the pillar growth rate is

given by the rates of Ga supply through surface diffusion, Ga consumption in sheath formation and Ga removal through sputtering. Sputtering also serves to remove all species, including F, N and O, through ion bombardment of unmasked regions of the pillar and the substrate. Ion beam heating may assist in maintaining the Ga in a liquid state, and may alter Ga diffusivity. It is, however, not a prerequisite for pillar formation. Ga is a supercooled liquid at room temperature [73], and our simulation results are insensitive to the exact value of D and account for pillar formation in the absence of temperature gradients caused by localized heating.

2.2 Model implementation

As mentioned above, the time- and spatially-dependent excess gallium concentration C (m^{-2}) was calculated by solving (2.2):

$$\frac{\partial C}{\partial t} = a\widehat{f} - bC + D\nabla^2 C.$$

where, a, is the excess gallium generation coefficient (atoms per ion), $\widehat{f}$ is the mean ion beam flux in the plane of the substrate (ions/m$^2 \cdot$ s), b is the Ga uptake rate by the sheath (s^{-1}), and D is the Ga diffusion coefficient. D is assumed to be the same on both surfaces.

The numerical model is axially symmetric about the z-axis. The surface was decomposed [74] into two axially symmetric, one dimensional domains (sheath and substrate) shown in Figure 2.7, with a continuity condition at the interface. Two arrays c_p for the pillar and c_s for the substrate held concentration values from the origin outward through the whole simulation. As the sheath grew, the smallest array cell on c_s and the top non-empty array cell on c_s were treated fractionally. In this way, domains never changed (and no re-meshing was required). For the purpose of simplifying simulation of diffusion, the slightly tapered sheath geometry is approximated by a uniform cylinder with a radius given by the base radius r_2. The model is then implemented by two coupled 1D models, sheath and substrate, in which diffusion is implemented using Cartesian $\left(D\nabla^2 C = D\frac{\partial^2 C}{\partial z^2}\right)$ and radial $\left(D\nabla^2 C = D\left(\frac{1}{r}\frac{\partial C}{\partial r} + \frac{\partial^2 C}{\partial r^2}\right)\right)$ coordinates, respectively. Where the sheath meets the substrate, concentration is passed between the two arrays c_p and c_s maintaining a conservation of mass.

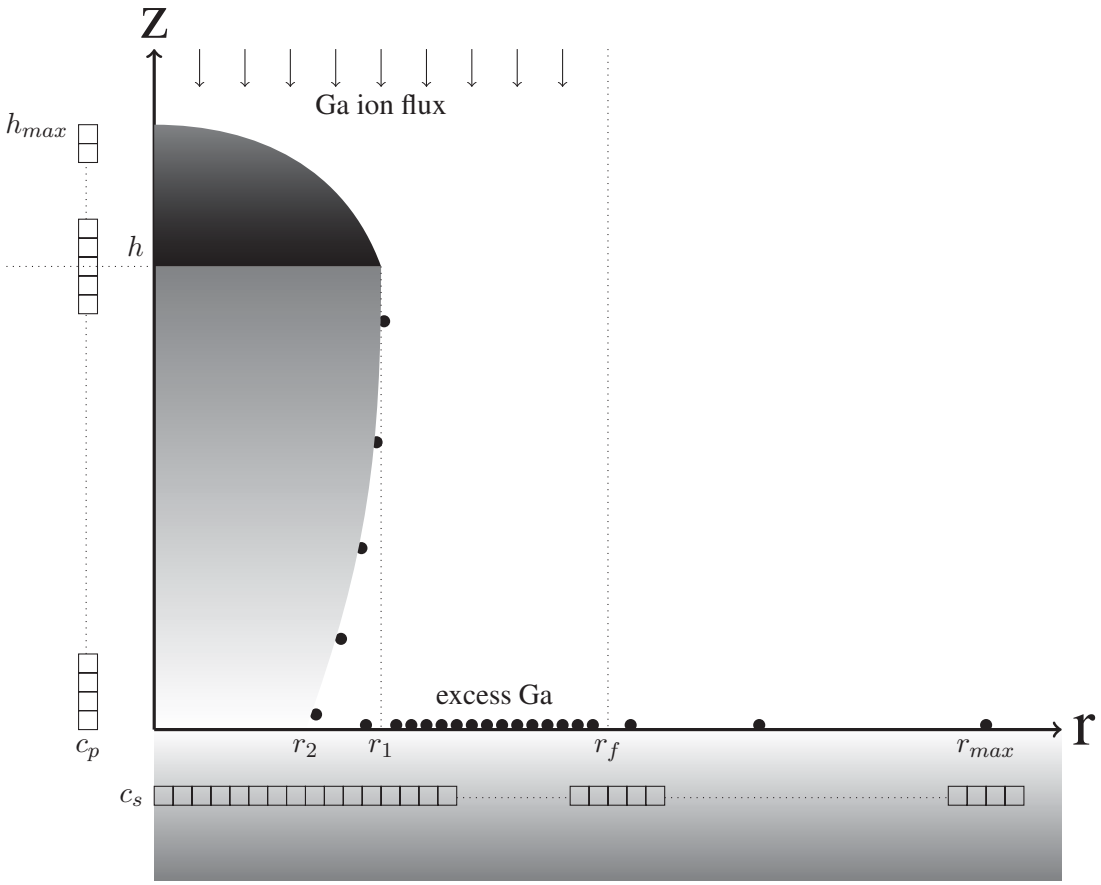

FIGURE 2.7: Numerical implementation of the model showing the substrate, and capped pillar (note the pillar physically gradually tapers from r_2 to r_1 but computationally has been approximated by a vertical cylinder). The computational domain consists of 1D arrays c_p and c_s containing the excess Ga concentration along the pillar and substrate, respectively. Excess gallium generated by the FIB diffuses out from the source region (r_1, r_f), over the substrate, and up the pillar. Dirichlet boundary conditions are implemented at the pillar height, h and substrate r_{max} where C is set to zero. All Ga removed at h is added to the droplet volume which increases the shadowed region (r_2, r_1). The droplet volume is also reduced by the FIB sputtering occurring in ratio with its apparent area. The pillar height h and base r_2 are set to increase through the simulation by a fit to measured data of the GaF sheath.

Here (2.2) was discretized using first- and second-order central-difference schemes for time and spatial derivatives respectively. The time step dt was set by the Lax-Richtmyer stability criterion [74, 75], $D\frac{dt}{dr^2} \leq \lambda$, where λ was typically set to 0.1. The model yields $C(z,t)$ and $C(r - r_2, t)$, where z is distance up the pillar sidewall (i.e., sheath), and $r - r_2$ is radial distance on the substrate from the pillar base. The excess Ga generation rate (atoms/s) is recorded as a function of time, as are the fractions of the excess Ga that are consumed by the sheath and the cap, and the fraction that is lost through out-diffusion.

The gallium generation rate, a, is only applied on the substrate region that is not masked by the pillar cap, $r_1 < r < r_f$, and is zeroed elsewhere. The gallium uptake rate, b, is only applied on the growing sheath region, $0 < z < h$, and is zeroed elsewhere. These constants are input to the simulation.

The gallium diffuses over the two geometrically distinct surfaces, and is subject to Dirichlet boundary conditions at the pillar top and a radial point sufficiently far away from the pillar base. The concentration is set to zero at these points in the model.

The volume of the droplet is also tracked. At each timestep, Ga removed by the boundary condition at the top of the pillar is added to the droplet. The droplet is assumed to be a spherical cap. The volume of the cap was determined by measuring the height and width of caps experimentally. This yielded a volume to radius radio used in computing the droplet growth. Sputtering of the droplet is handled as a boundary condition using the same value of the sputter flux ($\frac{\partial \gamma}{\partial t} = 10^7\ \mu\mathrm{m}^{-2}\mathrm{s}^{-1}$) as in (2.1). Finally, the ion flux, $\widehat{f}$, was set to $1.6 \times 10^6\ \mathrm{ions}/\mu\mathrm{m}/\mathrm{s}$, the experimental value used to generate Supplementary Video 2[2]. The changing droplet volume changes r_1.

The time-dependent values of h and r_2, which reflect growth of the GaF sheath, were supplied by fits to experimental data (see Figure 2.3 for an example of the r_2 data ($r_2 = d_2/2$) and fit).

The model was written in Python [76], and uses the scientific computing package NumPy [77] for efficiency optimizations.

2.2.1 Model results

The key achievement of the model is that it accounts for mass transport of Ga quantitatively (i.e., tracking material flux: in the droplet, sheath, vacuum, or diffusing out along the GaN surface), and it reproduces the pillar growth kinetics using realistic input parameters.

The parameter a was found by setting b to zero and fitting the calculated time-dependence of the cap volume, $V(t)$, to experiment (i.e., the cap of the pillar imaged in Supplementary Video 2). At short growth time, best fit is obtained when $a = 13$ (atoms/ion), which yields a flow rate of ~ 2.4 Ga atoms into the pillar cap per ion incident onto GaN, and corresponds exactly to the

[2]Videos are online at `http://dx.doi.org/10.1103/PhysRevLett.111.135503`

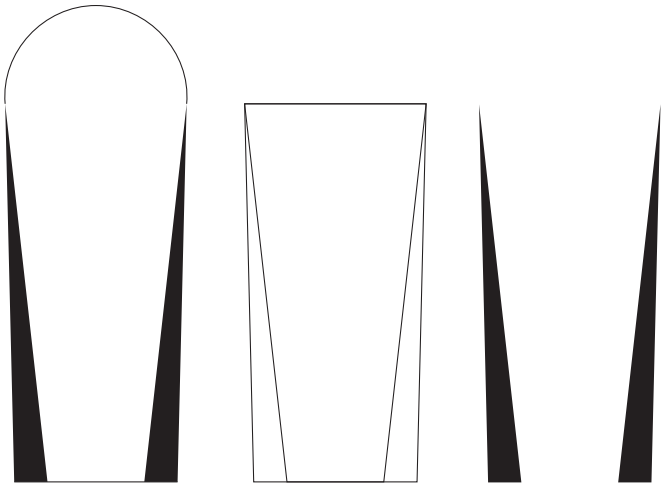

FIGURE 2.8: Schematic of sheath volume calculation as approximated by the difference between two inverted truncated cones. **Left** is a profile view of the pillar, cap, core and sheath. **Middle** is the two inverted truncated cones that define the inside and outside of the sheath. **Right** is the volume from the difference, the sheath volume.

initial volumetric excess Ga generation rate ($\partial V_0/\partial t \approx 10^{-3}\ \mu\mathrm{m}^3\mathrm{s}^{-1}$) used in (2.1). That is, the two models defined by (2.1) and (2.2) are consistent when the fraction of Ga consumed in sheath formation is ignored (i.e., $b = 0$). With this condition, both models are in good agreement with experiment at short growth times, where the sheath surface area is negligible, but overestimate the growth rates at long times, where a significant amount of excess Ga is used up in sheath formation.

Next, b was found by fixing a at 12, and by varying b so as to match the experimental $V(t)$ profile. Best fit was obtained by setting b to $1.1 \times 10^6\ \mathrm{s}^{-1}$, which yields a physically realistic sheath density (estimated from the measured sheath volume and the simulated uptake of Ga) that equals approximately half that of single-crystal GaF_3. This calculation is shown in detail next.

The sheath geometry can be approximated as the difference between two (inverted) truncated cones. One truncated cone is formed by the outside of the sheath, and the second is formed from the inside. They share the same height h, and radius r_1 at top, where the sheath comes to a point, and two different radii r_2 at the substrate, see Figure 2.8. The volume of a truncated cone is given by

$$V = \frac{1}{3}\pi h(r_1^2 + r_2^2 + r_1 r_2) \tag{2.3}$$

The experimental data for the radii and height are indicated in Table 2.1. The volume of the sheath

Volume	r_1 (μm)	r_2 (μm)	h (μm)
a	0.5918	0.3261	2.491
b	0.5918	0.5417	2.491

TABLE 2.1: Experimental data for determining the volume of the sheath.

is given by the difference of

$$V_{sheath} = V_b - V_a = 2.5153 - 1.6944 = 0.82089\mu\text{m}^3 \tag{2.4}$$

The size of a GaF_3 molecule is $V_{GaF_3} = 4.7 \times 10^{-11}\mu\text{m}^3$ so this volume could hold at most 1.75×10^{10} molecules. One Ga atom is required for every molecule of GaF_3. Integrating the simulated flux of atoms into the sheath over the time period specified (98.56 to 529.76 seconds) yielded 7.87×10^9 Ga atoms or 44%. Therefore the estimate for sheath density is reasonable, at approximately 1/2 that of a maximally packed crystal.

The Ga diffusion coefficient, D, equals $\sim$ 2000 $\mu\text{m}^2\text{s}^{-1}$ at room temperature [78, 79]. It was assumed to be constant across the pillar sidewall and the GaN substrate. The model output was insensitive to the exact value of D, which primarily affects only the amount of time it takes for $C(z,t)$ and $C(r-r_2,t)$ to reach a steady state. An example of model output is shown in Figure 2.9.

2.3 Self-ordering cycle

Finally, it is worthwhile to note that this process is a self-ordering cycle, see Figure 2.10. As a self-ordering process, many pillars can be grown in parallel, which is essential for large scale production. As a cycle it is self-limiting: as the droplet grows larger, it experiences more sputter and blocks more of the surface from generating the excess gallium. The combination of a cyclic process with self-ordering behaviour is seen in many places in natural living systems. When viewing videos of this pillar growth the eye instinctively identifies this growth as “life-like”, for just this reason, e.g., one can think of time-lapse footage of mushrooms sprouting. In the videos showing many pillars growing, one can also discern a competition for resources: larger pillars end

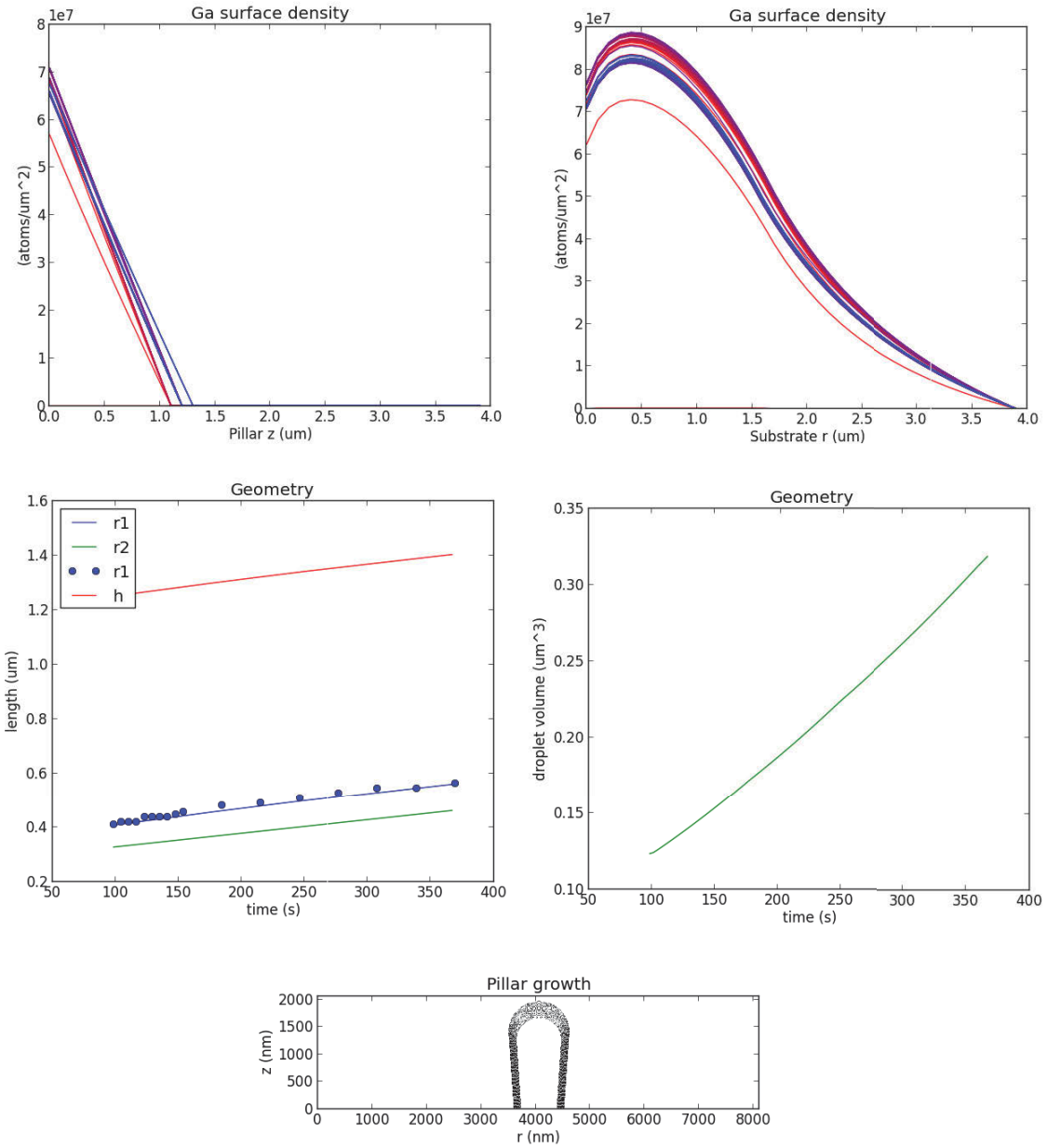

FIGURE 2.9: An example of the output generated by a simulation run showing the best value of flux to allow matching the data. **Top** graphs show concentrations on z and r over time ($t = 0$ is red curve, changing to blue at final t). **Middle** left shows data and model for the cap size, right shows droplet volume with time. **Bottom** shows reconstruction of pillar over time.

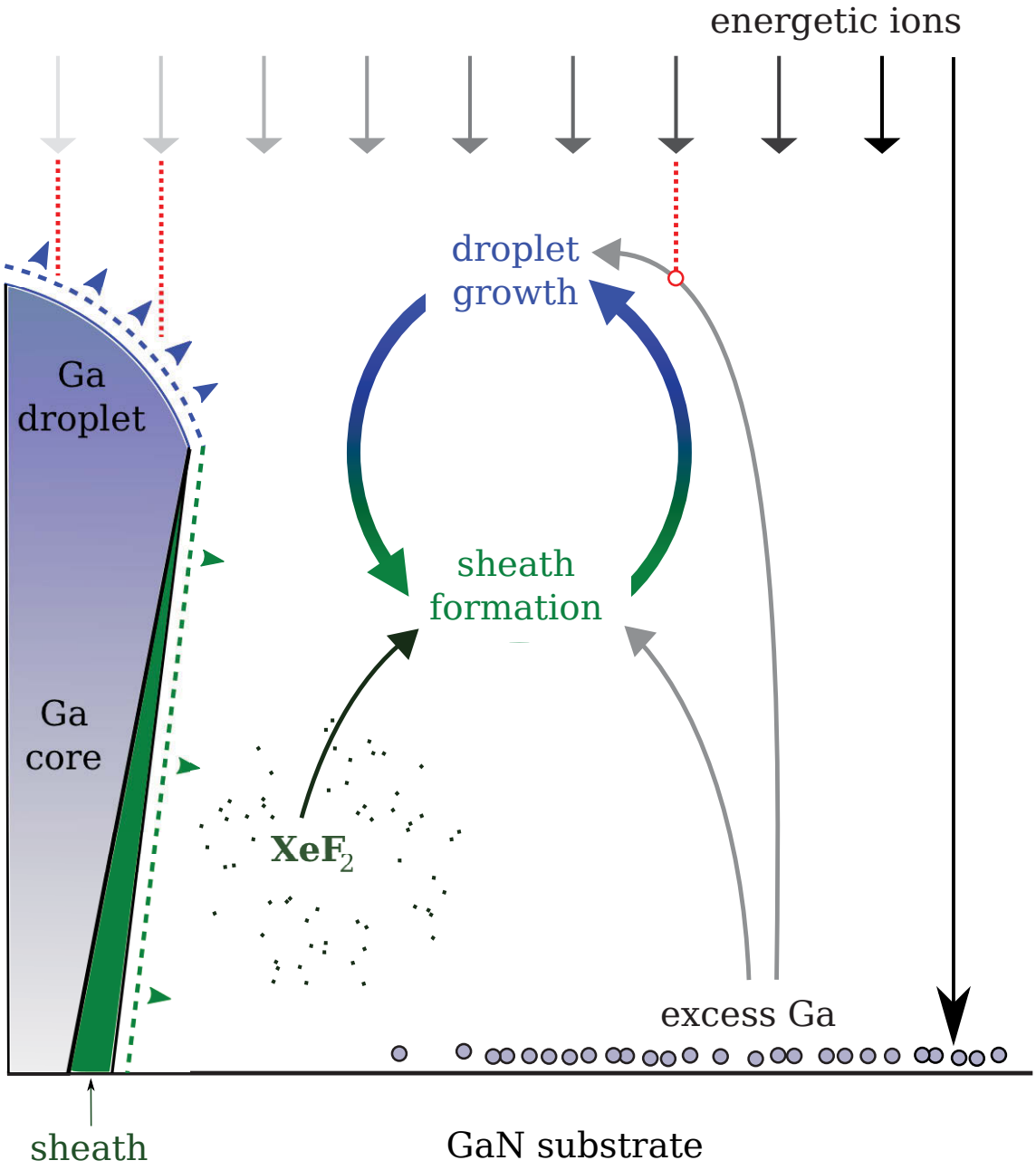

FIGURE 2.10: An interesting aspect of the pillar growth is that it is a self-ordering (and self-limiting) cycle. Sheath formation requires droplet growth (and XeF_2, secondary electrons (not shown), and excess gallium). Droplet growth requires sheath formation (and excess gallium). If any of these processes is interrupted then the growth cycle halts.

up drawing off the excess Ga so that no droplets nucleate nearby, but many smaller pillars can co-exist together as in Figure 2.1(d).

2.4 Conclusions

In this chapter, simplicity of the surface diffusion model depended on keeping the simulation in one dimension. This was achieved by: 1) approximating the sheath geometry (which physically is a gradually curving surface) as a cylinder which has a known Cartesian Laplacian, 2) careful joining of the two 1D simulations at the pillar base (to share in the flow of excess Ga), and finally, 3) exploiting the cylindrical symmetry. The resulting simulation ran in less time, consuming less memory and fewer instruction cycles, than a 2D or 3D model would. This allowed for more exploration of the parameter space of the gallium concentration kinetics, more time on the science, and less time waiting for simulation runs to complete. Not all problems provide high levels of symmetry that can be exploited. In the next two chapters full 3D simulations are required and different techniques are used.

Chapter 3

Surface evolution modelling

This chapter introduces the level set method (LSM), a technique to evolve surfaces in a topologically robust and stable fashion [80–82]. The level set method is used to demonstrate what topographic patterns are produced by different anisotropic etch rates. This work was motivated by the discovery of patterns which had not been reported in prior beam chemistry literature. By finding the correct "rule set" the simulation predicts the surface evolution on diamond from electron beam induced etching (EBIE). The anisotropic etch model, originally derived by Hubbard [83], and expanded upon by Radjenovic [84–89], is used here to explain etching conditions on diamond crystal, and shed light on the underlying etch mechanism.

In the next chapter (Chapter 4), the level set method is used to evolve surfaces based on rates obtained by solving a reaction-diffusion (RD) equations which are used to model electron and ion beam induced deposition/etching. The RD equation is solved on an embedded surface by the closest point method (CPM) [90–93], which integrates naturally with the LSM. Using these techniques the chapter demonstrates a surface evolution algorithm driven by an adsorbate kinetics model which can be used to model electron and ion-beam induced etching and deposition. This simulation is state-of-the-art in that it can easily track 3D surfaces, and can solve kinetics and compute evolution in reasonable times (minutes to hours).

All experimental work in this chapter was done by Aiden Martin and James Bishop. The experiment and model were published in *Dynamic pattern formation in electron beam induced etching* [94]. This chapter includes portions of the experimental and theoretical work to show that this type

of simulation agrees with theory and experiment, and provides broader context for simulations in Chapter 4. Aiden Martin and Alan Bahm contributed equally to the work.

Section 3.1 includes the experimental and modelling results. Section 3.2 explains the level set method technique, and Section 3.3 the implementation and the verification of the code. Applying the technique to the case of anisotropic etching is covered in Section 3.4. Finally Section 3.5 presents conclusions and implications of this work.

3.1 Dynamic pattern formation in electron beam induced etching: Published in [94]

Abstract of publication [94]: We report highly ordered topographic patterns that form on the surface of diamond, span multiple length scales and have a symmetry controlled by the precursor gas species used in electron beam induced etching (EBIE). The pattern formation dynamics reveal an etch rate anisotropy and an electron energy transfer pathway that has been overlooked by existing EBIE models. We therefore modify established theory such that it explains our results and remains universally applicable to EBIE. The patterns can be exploited in controlled wetting, optical structuring and other emerging applications that require nano and micro-scale surface texturing of a wide bandgap material.

Electron beam induced etching [40, 95] is a high resolution, single step, direct-write nanofabrication technique in which a precursor gas and an electron beam are used to realize etching. To date, EBIE has been used to study electron interactions with solids and adsorbates, and to machine a wide range of materials using etch precursors such as oxygen, water, ammonia, nitrogen trifluoride, xenon difluoride and chlorine. Key advantages of EBIE include cite-specificity, the absence of staining and severe damage inherent to focussed ion beam techniques, and the ability to etch materials such as diamond which are resistant to conventional chemical etch processes. Consequently, EBIE has recently been used to realize practical device components for use in photonics [96], plasmonics [97] and nanofluidics [98].

In this work, we report dynamic, highly ordered topographic patterns that form spontaneously on the surface of diamond during EBIE. Pattern formation is a ubiquitous process that provides

fundamental insights into the roles of symmetry breaking, anisotropy and nonlinear interactions in emergent phenomena [99–101]. Here it reveals a chemical etch rate anisotropy that can not be explained by established EBIE theory. We therefore propose a fundamental modification, whereby the critical role of energetic electrons is to transfer energy to surface atoms of the solid rather than to surface-adsorbed precursor molecules. The new EBIE model is confirmed experimentally, explains the observed patterns, and resolves long standing problems that have been identified in the EBIE literature.

Figure 3.1(a) is a schematic illustration of EBIE performed using H_2O precursor gas. Figure 3.1(b) shows images of topographic patterns that form on the surface of single crystal (001) oriented diamond during H_2O EBIE performed at room temperature (a detailed description of the experimental methods is provided in the Supporting Information). A movie showing the pattern formation and evolution dynamics is provided as Supplementary Video #1.[1] Etching initiates at scratches and other surface defects, which expand laterally during EBIE, evolving into highly symmetric rhombohedra such as the large pit seen in the top left corner of Figure 3.1(b). Similarly, the topography that is normally associated with surface roughness caused by EBIE rapidly evolves into step edges with $\{110\}$ sidewalls which propagate laterally until they reach the edge of the area scanned by the electron beam. The $\{111\}$ family of planes is absent from the resulting surface topography, the step sidewalls are comprised of $\{110\}$ planes, and 90° step corners are formed at the intercepts of the $\{110\}$ planes. Corner formation requires the (110), $(\bar{1}10)$, $(\bar{1}\bar{1}0)$ and $(1\bar{1}0)$ planes to etch slower than the (100), (010), $(0\bar{1}0)$ and $(\bar{1}00)$ planes. From these observations, we conclude that H_2O-mediated EBIE removes material from the $\{100\}$ and $\{111\}$ planes faster than from the $\{110\}$ family of planes.

In order to prove conclusively that the proposed anisotropy yields the four-fold symmetry observed in Figure 3.1(b), we used the 3D implementation of the level set method (LSM) [81]. LSM is a robust technique for evolving implicit surfaces under anisotropic velocity fields. It can be used to calculate surface shapes produced by anisotropies defined by differences between the etch rates of specific crystal planes. The simulations detailed in the Section 3.4 reveal that the calculated surfaces match experiment only if the $\{110\}$ planes that are oriented at 90° with respect to the

[1] See Supplemental Material at `http://dx.doi.org/10.1103/PhysRevLett.115.255501` for scanning electron microscope (SEM) movies of the etch process and detailed descriptions of the experimental methods. These are not included here.

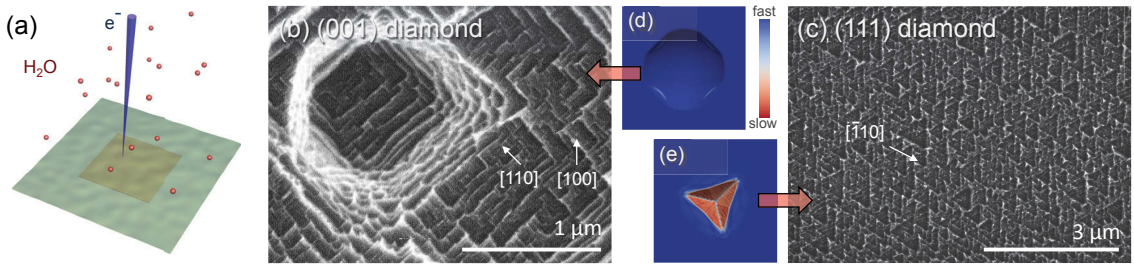

FIGURE 3.1: Topographic patterns formed during H_2O mediated electron beam induced etching of single crystal diamond. **(a)** Schematic illustration of H_2O EBIE. **(b)** Expanding rhombohedra formed on the surface of (001) oriented diamond, and **(c)** trigons on the surface of (111) diamond. **(d,e)** Corresponding simulated rhombohedra and trigons (colored by the relative local etch rate) that are expected if the $\{110\}$ planes are the slowest etching planes.

electron beam axis etch slower than all other planes. Supplementary Video #2 and Figure 3.1(d) show the resulting rhombohedral surface features[2].

The validity of the simulation was confirmed by applying the same etch rate anisotropy rule set to (111) oriented diamond. The simulation and H_2O EBIE both produced the trigons shown in Figure 3.1(c) and (e). The LSM simulations therefore support our conclusion that the geometries of patterns observed during H_2O EBIE of (001) and (111) oriented diamond is governed primarily by slow etching of specific $\{110\}$ planes. However, this anisotropy can not be explained by conventional, established EBIE theory which is based on the assumption that the key role of energetic electrons is to dissociate surface-adsorbed precursor molecules. In the case of H_2O EBIE of diamond, a possible pathway in this framework is the following [40, 95]:

$$\mathrm{H_2O_{[v]}} \leftrightarrow \mathrm{H_2O_{[p]}} \tag{3.1}$$

$$\mathrm{H_2O_{[p]}} \xrightarrow{\Xi_1} \mathrm{H_2} + \mathrm{O^*_{[c]}} \tag{3.2}$$

$$\mathrm{O^*_{[c]}} + \mathrm{C_{[s]}} \rightarrow \mathrm{C_{[s]}O_{[c]}} \tag{3.3}$$

$$\mathrm{C_{[s]}O_{[c]}} \xrightarrow{\Xi_2} \mathrm{CO_{[v]}} \tag{3.4}$$

where the subscripts [v], [s], [p] and [c] signify the vapour phase, solid phase, physisorbed and chemisorbed species, respectively. Ξ_1 represents the energy barrier for dissociation of H_2O, and Ξ_2 is the binding energy of the reaction product. According to the standard EBIE model, Ξ_1 and Ξ_2 are overcome by a transfer of kinetic energy from the electrons that drive EBIE, and thermal energy of the substrate (kT), respectively. This model has been used to explain a wide range of

[2]See videos online at `http://dx.doi.org/10.1103/PhysRevLett.115.255501`

experiments such as dependencies of etch rates on time, beam current density and pressure of the precursor gas [26, 95, 98, 102–111]. However, the model can not explain the etch rate anisotropy seen in Figure 3.1, unless different crystal planes give rise to significant variations in the electron dissociation cross-section of H_2O adsorbates, the secondary electron emission yield, or the local coverage of precursor molecule adsorbates. None of these are plausible since the precursor is H_2O, the patterns form at room temperature (and at elevated temperatures, as is discussed below), and the slowest etching planes are not consistently dark in secondary electron images.

To resolve the above issues, we propose a new mechanism, in which electrons provide the energy Ξ_2 in Reaction 3.4. That is, the critical role of electrons is not to dissociate the physisorbed precursor molecules, but to break bonds that bind surface atoms to the substrate and thus enable the desorption of the final reaction products. During etching, Reaction 3.2 can reasonably be expected to proceed spontaneously since active surface sites are generated continuously and the precursor molecules will likely dissociate on unterminated sites. In this framework, the etch rate anisotropy needed to produce the patterns seen in Figure 3.1 is not surprising since Ξ_2 (i.e., the C-C bond strength and the corresponding cross-section for scission by electrons) varies with the crystal plane.

To confirm the proposed EBIE mechanism we performed an experiment based on the fact [112] that the C-C bond strengths are modified by hydrogen which reconstructs and stabilizes the $\{111\}$ surface. We therefore performed H_2O EBIE of (001) and (111) oriented diamond in the presence of NH_3 gas, where the role of the NH_3 is to supply an excess of hydrogen radicals to terminate the (111) planes. Figure 3.2 shows that the corresponding surface patterns consist of inverted pyramids and trigons, respectively, and that these geometries are indeed expected from LSM simulations in which the $\{111\}$ planes are the slowest etching planes.

We performed one more experiment to further test the proposed EBIE mechanism. A consequence of the conventional EBIE model is that the EBIE rate is directly proportional to the concentration of physisorbed precursor molecules [40, 95]. Hence, the etch rate of diamond is expected to be negligible at a temperature of $\sim$ 400 K, as is shown in Figure 3.3 (solid curves, calculated using the rate equation model presented in the Supporting Information), irrespective of the electron flux used to perform EBIE. However, we observe significant etch rates at temperatures as high as 600 K where the measured etch rate is over three orders of magnitude higher than that predicted by the

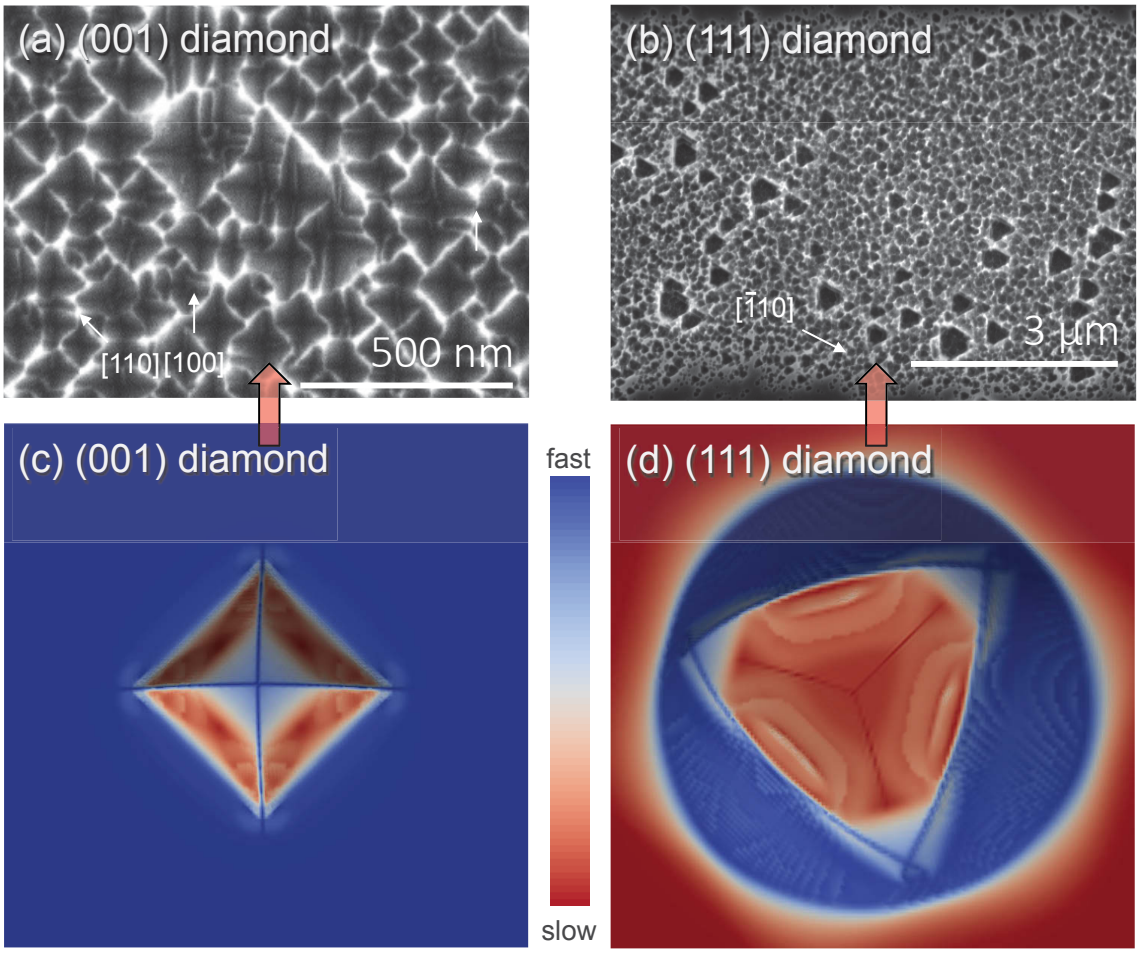

FIGURE 3.2: Topographic patterns formed during electron beam induced etching of single crystal diamond in the presence of NH_3. **(a)** Expanding inverting pyramids formed on the surface of (001) oriented diamond, and **(b)** trigons on the surface of (111) diamond. **(c,d)** Corresponding simulated pyramids and trigons (coloured by the relative local etch rate) that are expected if the $\{111\}$ planes are the slowest etching planes.

conventional EBIE model. This result is clearly inconsistent with the conventional model, but is expected from the new model in which the EBIE rate is proportional to the concentration of chemisorbed oxygen. The observed temperature dependence therefore serves as direct evidence for the new EBIE model. Furthermore, the topographic patterns were observed at all temperatures that were investigated, as is illustrated by the image shown in the inset of Figure 3.3. The abrupt step edges in the patterns generated at $\sim$ 600 K are inconsistent with any model that attempts to explain the etch rate anisotropy by spatial variations in the coverage of physisorbed adsorbates.

We note that the new EBIE model is consistent with all results in the literature that were explained successfully by the conventional EBIE model. First, both models predict the same dependence of

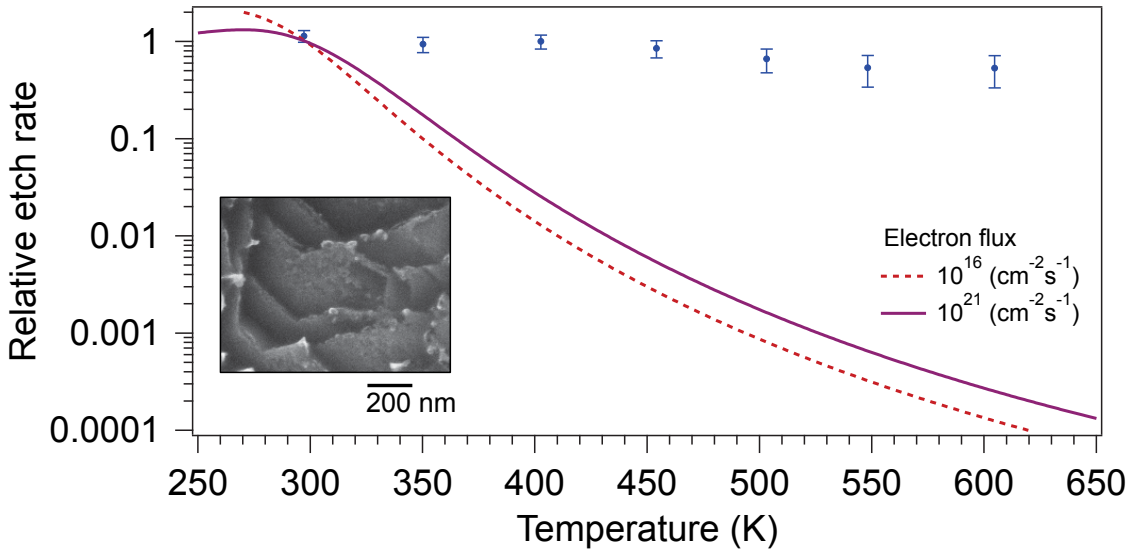

FIGURE 3.3: Temperature dependence of the rate of EBIE measured experimentally (points) and calculated using the established model of EBIE detailed in the Supporting Information (lines) using a wide range of electron fluxes. The etch rates are normalized to the EBIE rate at room temperature. The inset shows an image of surface topography generated by H_2O EBIE at $\sim$ 600 K.

EBIE rate on electron beam energy since the secondary electron yield has the same dependence on beam energy as the amount of energy that is deposited by the beam into the surface atoms of the substrate. Second, both models predict the existence of reaction rate limited and mass transport limited etching regimes (as is shown in the Supporting Information), which makes both models consistent with a large amount of experimental data available in the EBIE literature. However, the new model is unique in being consistent with reports of UV laser induced etching of diamond, that is believed to proceed through a two photon C-C bond scission mechanism [101]. The new model also provides a satisfactory explanation for the fact that single crystal diamond can be etched by EBIE in the first place. The energy barrier of Reaction 3.4 in diamond is known to be significant [113] and therefore etching observed at room temperature, or any temperature below the onset of defect generation and graphitization cannot be accounted for in the standard model.

Finally, we note that the topographic patterns cannot be explained by an anisotropic sub-surface damage generation mechanism analogous to the graphitization pathways encountered in conventional dry and wet diamond etch processes [114, 115] for a number of reasons. First, the etch rate anisotropy was modified significantly by the presence of NH_3 gas, which should not change the sub-surface damage generation rate. Second, prior studies of EBIE of single crystal diamond have

failed to produce any evidence of damage by photoluminescence and Raman spectroscopy [96, 110, 116, 117]. Third, the generation rate of damage produced by a 5 keV electron beam scales with the local energy density deposited into the substrate throughout the electron interaction volume [118]. The damage generation rate is therefore isotropic, except for special cases where the electron beam axis is parallel to a channeling axis, which should produce a strong dependence of the patterns on sample tilt, which was not observed in our experiments. We therefore conclude that sub-surface damage generation does not play a role in the observed etching and pattern formation behaviour.

To summarize, we showed several dynamic pattern formations on the surface of single crystal diamond. We proposed an amended model for the EBIE process that is based on interactions of electrons with the substrate rather than the precursor molecule adsorbates. Our results can be leveraged to engineer surface patterns controlled by electron beam irradiation conditions.

3.2 Level set method

The modelling for the preceding section makes use of the level set method, explained here in two dimensions. The next Section 3.3 demonstrates the 2D implementation and verification. After this, Section 3.4 extends the LSM to three dimensions and explains the anisotropic etching model.

The *level set method* is a technique, invented in the 1980s, for evolving a surface under a velocity field, generally attributed to Sethian and Osher. Very good overview texts include [80–82]. The level set method evolves a surface *implicitly* instead of explicitly (c.f. Subsection 3.2.1), the benefit of which is stable, topologically-robust evolution. Implicit surfaces can merge and separate seamlessly while explicit surface methods have to contend with awkward *de-looping* when evolution creates a self-intersection. Topological changes are nicely shown in 2D image segmentation examples [119], see Figure 3.4. Another advantage is that the LSM avoids the need for resampling (or re-parametrizing) the surface when nodes become spaced too far apart or too close together. Finally, the LSM is powerful in that correctly working code in 2D extends almost trivially to higher dimensions, a property lacking in any explicit (mesh-based) surface evolution algorithm.

This technique has been applied in computational physics areas such as interface tracking, deformable models, microfluidics [120], fluid flow simulations [121], image restoration, 3D medical

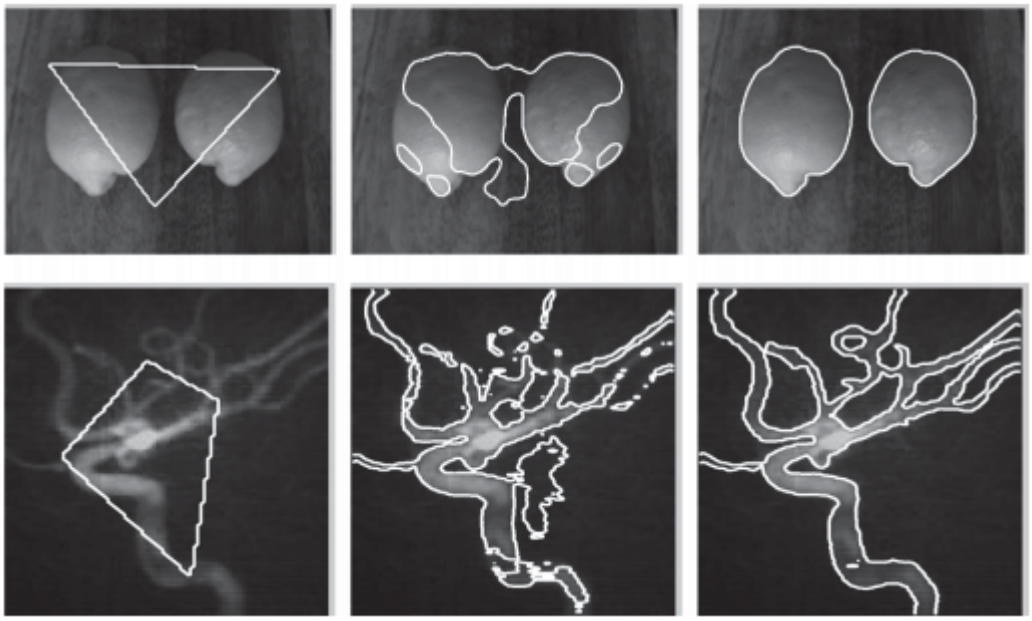

FIGURE 3.4: Image segmentation using the 2D LSM from [119] demonstrating the ability to merge and separate 1D contours on a 2D image to segment out interesting information. In this case, advancing the initial contour with speeds derived from the image allows the identification of a lemon (**top**) and blood vessel (**bottom**). The left, middle, and right columns show the initial, intermediate and final contours.

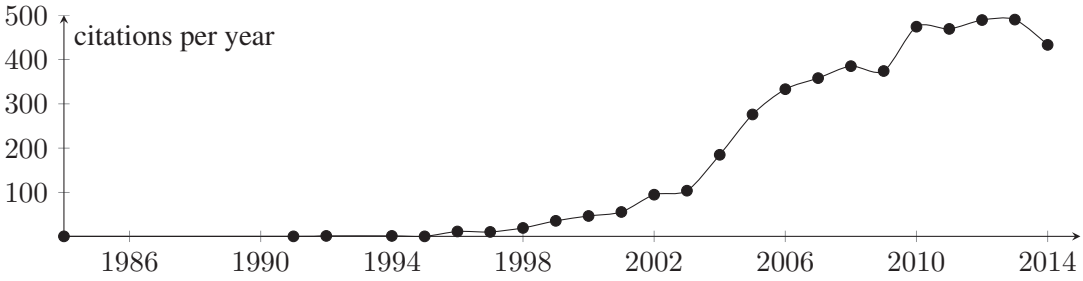

FIGURE 3.5: The level set method has been the topic of over 10,000 publications as of 2015.

imaging (MRI) [122], simulation of water and smoke [123], image segmentation [124, 125], thin film [126, 127] and crystal growth [127–131], shape optimization [132, 133], and modelling field evaporation in an atom probe [134], and is an active and growing area of research today (see Figure 3.5).

The first simulation of etching, deposition, and lithography development with the level set method was in 1997 by Sethian and Adalsteinsson [135]. Since 2000 it has been used to simulate sputtering and re-deposition in focused ion beam (FIB) simulations of amorphous materials by Kim and Hobler [14, 15, 136], wet and dry etch simulations by Radjenovic [84–89, 137–143], wafer surface

etching and deposition [144–154] and FIB milling [155]. In this thesis the level set method is used to simulate surface evolution from electron beam diamond etching (this chapter) and generalized deposition (Chapter 4).

3.2.1 Concept

Consider a surface[3] Γ moving under a velocity field, $\boldsymbol{v}$. The *level set function*, ϕ, is defined to be zero only on the surface

$$\phi(\boldsymbol{x}, t) = 0 \tag{3.5}$$

positive outside (or above) the surface and negative inside (below), referred to as Ω^+ and Ω^- respectively. The explicit surface $\partial\Omega$ (also known as Γ) is now "hidden" or *embedded* in this scalar function ϕ consequently called the *surface embedding*[4], see Figure 3.6. One of the advantages of this formulation is that characteristics of the surface geometry can be expressed simply, but in a form that extends over the whole volume. Most useful is the definition for the normal of the surface, which is given by

$$\boldsymbol{n} = \frac{\nabla\phi}{|\nabla\phi|} \tag{3.6}$$

and there are also natural definitions for curvature, κ, given in [80] and [81] which can be important when considering the additional physics of surface tension.

Evolution of ϕ advances the implicit surface. Taking the total time differential of (3.5) and applying the chain rule yields

$$\frac{\partial\phi}{\partial t} + \frac{\partial\phi}{\partial x}\frac{dx}{dt} + \frac{\partial\phi}{\partial y}\frac{dy}{dt} + \frac{\partial\phi}{\partial z}\frac{dz}{dt} = 0 \tag{3.7}$$

which can be compactly expressed in vector notation as

$$\phi_t + \boldsymbol{v}\cdot\nabla\phi = 0 \tag{3.8}$$

[3] The surface is of *codimension one* in R^3, meaning a $(3-1=2)$ two-dimensional surface in a three-dimensional space, or, a $(2-1=1)$ one-dimensional curve in a two-dimensional space.

[4] In specifying $\phi(\boldsymbol{x}, t)$ we are, for the first time, introducing a coordinate system. As Sethian noted [156], this is an unusual mathematical choice, as we have imposed an unnatural order on the problem in some sense, but we have at the same time added a dimension not previously present in the problem. Hermann Weyl famously critiqued coordinates as "the introduction of a coordinate system to geometry is an act of violence" (presumably stepping away from a purer mathematical form to a more pedantic form).

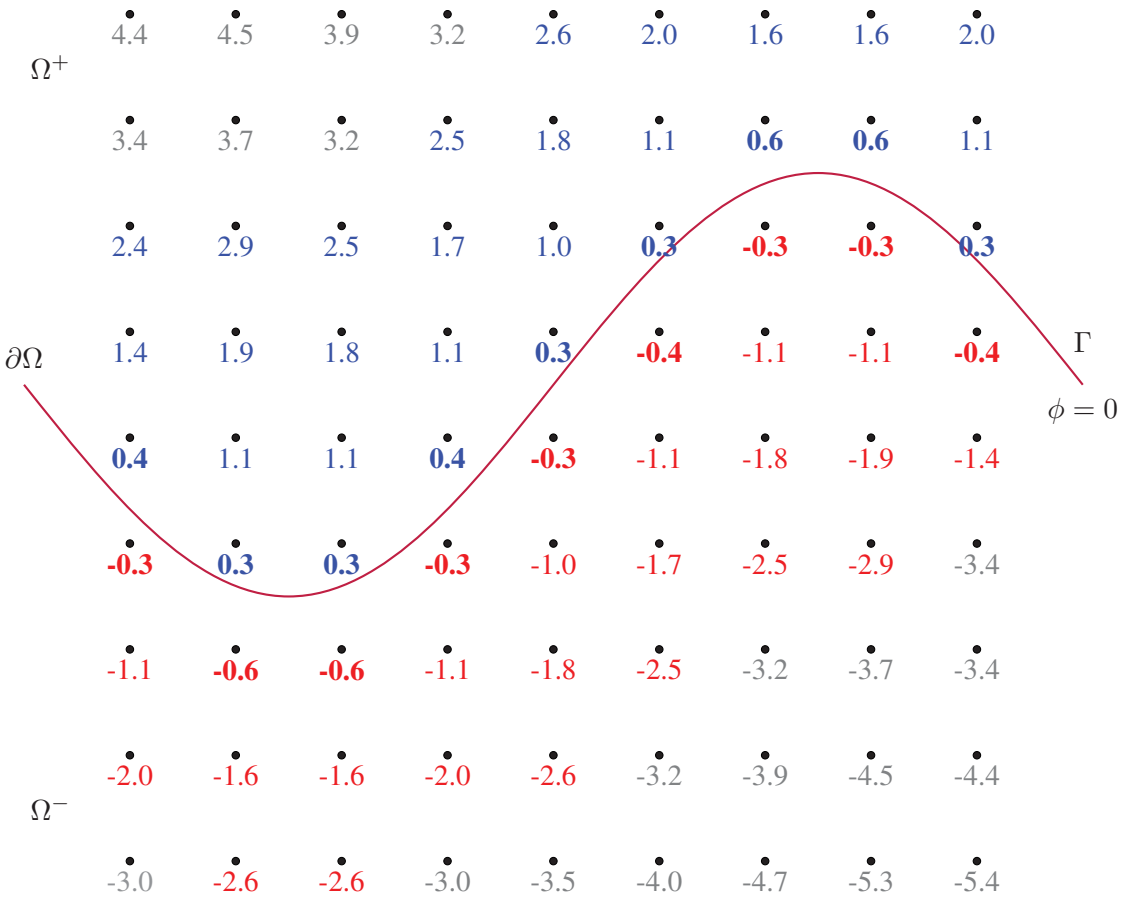

FIGURE 3.6: Two-dimensional example of a level set ϕ at regular grid points that is implicitly representing a sinusoidal surface (purple curve). The level set function, ϕ, has been initialized to the signed distance from the surface, the bold values control the location of the implicit surface. Positive (blue) and negative (red) are indicated in a narrow band around the implicit interface. Points outside the narrow band ($|\phi| > 3$) are shown in grey.

where the notation ϕ_t is the partial temporal derivative $\frac{\partial \phi}{\partial t}$, ∇ is the partial spatial derivative, and $\boldsymbol{v}$ is the total time derivative of the surface (also known as the desired velocity of the interface). The velocity field, $\boldsymbol{v}(\boldsymbol{x}, t)$, can be decomposed into normal ($v_N \boldsymbol{n}$) and tangential ($v_T \boldsymbol{t}$) vector components with respect to the surface where v_N and v_T are scalar fields specifying the speed in the normal and tangential directions respectively, that is,

$$\boldsymbol{v} \cdot \nabla \phi = (v_N \boldsymbol{n} + v_T \boldsymbol{t}) \cdot \nabla \phi \tag{3.9}$$

the tangential component vanishes, and defining $F \equiv v_N$, (3.8) becomes

$$\phi_t + F \, |\nabla \phi| = 0 \tag{3.10}$$

This is the canonical *level set equation*. What is remarkable is that we have eliminated the original boundary Γ entirely, and represented it *implicitly* in ϕ. When this partial differential equation is advanced in time, we can at any later time find our evolved surface by seeking out $\phi = 0$.

The scalar F is the speed of the surface normal to itself at all points on the surface. The functional form of F determines what kind of partial differential equation (3.10) is. For only positive $F = F(\boldsymbol{x}) > 0$, (3.10) is the *Eikonial equation* (see Sethian [80]). In this case the boundary always moves outward, and will never re-cross a specific point more than once, e.g., a fire burning in prairie will only visit each spot once. A special subcase, $F = 1$, can be used to generate a *signed distance function*

$$|\nabla\phi| = 1 \tag{3.11}$$

where every value of ϕ will reflect the distance to the surface, positive if "above" and negative if "below", referred to as Ω^+ and Ω^- respectively. For F dependant at most on first order derivatives of ϕ, i.e., $F = F(\boldsymbol{x}, \phi, \nabla\phi)$, (3.10) is a hyperbolic differential equation, the *Hamilton-Jacobi equation* (HJE)

$$\phi_t - H(t, \boldsymbol{x}, \phi, \nabla\phi) = 0 \tag{3.12}$$

Hamilton-Jacobi equations have well developed techniques for numerical integration, see Subsection 3.2.4.

The level set equation (3.10) is not generally differentiable (because of the absolute value), consequently solutions found for it are known as *weak solutions*. It was work pioneered by Crandall and Lions [157, 158] in 1983 which found viscosity solutions to HJE that allowed for the level set technique to be constructed. A viscosity solution is a technique whereby a small viscosity term, $\epsilon\Delta u$, is added to the HJE, allowing the correct solution to be reached as $\epsilon \to 0$. The level set function ϕ can be any function that conforms to (3.5), as long as it is Lipschitz continuous function, that is, it satisfies

$$\frac{\phi(x) - \phi(y)}{x - y} < C \tag{3.13}$$

for some constant C and arbitrary x and y. One natural choice is the signed distance function (sdf), which is often used in reinitialization, described next.

For more complete introductions to the level set method, there are several key books by Sethian

[80] and Osher [81, 82], as well as some useful PhD dissertations, including Ertl [152], Sheikholeslami [146] and Nielson [159].

3.2.2 Reinitialization

The level set function ϕ can drift away from a signed distance function over time, especially if artefacts creep in from boundary conditions far from the surface. Reinitialization is the process of resetting ϕ to a signed distance from the interface. Overuse of periodic reinitialization is discouraged [80] as it can affect the implicit surface. One technique implemented in the code in the present work is to avoid drift by use of a well chosen *extension velocity* [160] as discussed in Subsection 3.2.7. This successfully avoided the need for reinitialization.

3.2.3 Non-convex Hamiltonian

Sethian introduced the first case of the level set method to simulate etching, deposition and photoresist development [135]. These applications require the use of a *non-convex Hamiltonian* in the HJE formulation of the level set equation because of the surface speed driven by the sputter yield, see Figure 3.7. The Hamiltonian is non-convex if any of the second derivatives are negative, that is if

$$\frac{\partial^2 H}{\partial p_i \partial p_j} < 0 \qquad \forall i, j \in 1...3 \tag{3.14}$$

This condition has implications for the numerical discretization of the system, see Subsection 3.2.4. Radjenovic has subsequently carried out multiple studies of wet etching, plasma etching and deep reactive ion etching (DREI or Bosch process), using a non-convex Hamiltonian [84–89, 137–143, 161].

3.2.4 Discretization and choice of scheme

Given the level set equation (3.10) with a well defined speed function F the next step is *numerical discretization* for simulation. The derivatives will be approximated by *finite differences*, which can

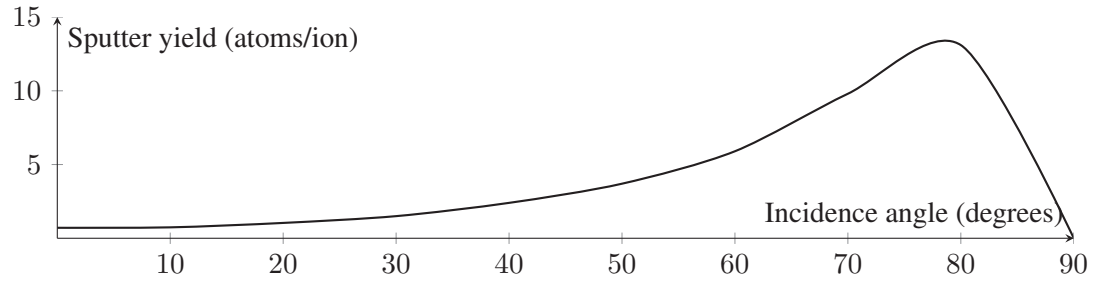

FIGURE 3.7: The speed function created from a typical atomic sputter yield (as generated by ion-soild monte carlo code, Appendix A) becomes non-convex around 70-80 degrees. This results in a non-convex Hamiltonian for the system.

be derived from a Taylor expansion. Notationally a first-order spacial derivative can be approximated by *backward, forward or central differences*

$$\phi_x^- \equiv \frac{\phi_{ijk} - \phi_{i-1,jk}}{\Delta x} \tag{3.15}$$

$$\frac{\partial \phi}{\partial x} \approx \phi_x^+ \equiv \frac{\phi_{i+1,jk} - \phi_{ijk}}{\Delta x} \tag{3.16}$$

$$\phi_x^0 \equiv \frac{\phi_{i+1,jk} - \phi_{i-1,jk}}{2\Delta x} \tag{3.17}$$

with similar expressions for ϕ_y and ϕ_z. Observe that the symmetric central difference is the average of the forward and backward differences $\phi_x^0 = (\phi_x^+ + \phi_x^-)/2$.

Depending on the form of the speed function F, different combinations of spatial discretizations can be chosen, comprising a *scheme*. Various schemes including *upwind*, *Lax-Friedrichs*, *Roe-Fix*, are all discussed in [81, 159]. The upwinding scheme, used for *convex-HJE*, selects between forward and backward differences to simulate the direction of propagation of information driven by the sign of the speed. Non-convex speed functions (common for ion-sputter yield curves) lead to non-convex Hamiltonians requiring use of a scheme such as the Lax-Friedrichs scheme [80, 135], which is given [81] in two dimensions[5] as

$$\hat{H} = H\left(\frac{\phi_x^- + \phi_x^+}{2}, \frac{\phi_y^- + \phi_y^+}{2}\right) - \alpha^x\left(\frac{\phi_x^+ - \phi_x^-}{2}\right) - \alpha^y\left(\frac{\phi_y^+ - \phi_y^-}{2}\right) \tag{3.18}$$

[5] In three dimensions the form is extended similarly.

where $\hat{H}$ is the exact Hamiltonian, and H is the discretized approximation, and the α terms are dissipation coefficients chosen by the partial derivatives of H as

$$\alpha^x = \max |H_1(\phi_x, \phi_y)| \qquad \alpha^y = \max |H_2(\phi_x, \phi_y)| \tag{3.19}$$

where $H_1 \equiv \partial H/\partial \phi_x$ and $H_2 \equiv \partial H/\partial \phi_y$. Underestimating these coefficients can lead to surface instabilities, while overestimating will over-smooth the evolution [152]. However, it is not hard to run trials to create estimates. More advanced and CPU intensive schemes exist (*Local-Lax-Friedrichs*, *Local-Local-Lax-Friedrichs*) which locally determine dissipation at every time step.

Temporal discretization can be *forward Euler*, or *Total Variation Diminishing Runge-Kutta* (TVD RK) if more accuracy is needed. The latter is notably used with many flavours in image segmentation [82]. TVDRK is also known as "Strong stability preserving RK" [162].

3.2.5 Sparse field

As described so far the 3D full-array level set method implemented on a volume of linear dimension N would be computationally expensive, as it scales as $O(N^3)$. Sethian [80] initially described a faster algorithm, the *narrow band method*, which considers only a small window of size k around the embedded surface, which scales as $O(kM^2)$ where M is the number of cells in the narrow band. This concept was taken to its limit by careful shrinking of the band to a single grid point on either side of the surface in the *sparse field method*, originated by Whitaker [163–165]. The code referenced in this thesis uses the full-array method as the simulation sizes were small enough that optimization was not required.

3.2.6 Fast marching method

For strictly positive functions, $F > 0$, the level set equation (3.10) becomes a boundary value problem, and the front-crossing time, ϕ, can be solved over the whole domain quickly by the *fast marching method* (FMM). This algorithm begins at grid points near the embedded interface and sweeps outward with the number of computational operations scaling as $O(N^3 \log N)$ in 3D. This improvement over the brute force approach, which scales as $O(N^6)$, is made possible by strategic

use of the *min-heap* data structure [166]. This method is implemented and used by the code in this thesis for initializing volumes with a given surface. The fast marching method is also important for computing the extension velocity. Other alternatives, such as the fast sweeping method [167] were not considered.

3.2.7 Extension velocity

In many physical problems, the level set speed function F has a well defined meaning on the interface, but not off the interface. However, the level set equation (3.10) requires that F be defined everywhere, sometimes called the *extension velocity*, F_{ext}. With the only constraint being that the extension velocity matches the interface speed at the interface, $F_{ext}(\phi = 0) = F$, there is considerable latitude to define F_{ext}. This flexibility can be employed to avoid periodic reinitialization, using the fast marching method as per Adalsteinsson [160]. The extension velocity is adjusted to continually maintain a signed distance function near the surface and is held as the recommended practice [80], despite the more efficient but less accurate method by Richards [168], and the more recent and accurate work by Chopp [169, 170], which does not yet extend to 3D. If further efficiency is needed, a technique for narrow-banded extension velocity can be employed by Peng [171].

3.3 Implementation and verification

A level set surface evolution algorithm was implemented in Julia, see Appendix C. It supports extension velocities, re-initialization, convex and non-convex Hamiltonians, and Lax-Friedrichs (LF) and Local-Lax-Friedrichs (LLF) dissipation schemes. This custom code allows for straightforward integration with the Ion-Solid-Interactions code (see Appendix A) and the adsorbate kinetics modelling code (Chapter 4).

Design of this core code was informed by reviewing the few existing LSM libraries. Code by Dr. Ian Mitchell for Matlab designs for the full-array method only, and does not support extension velocities or fast marching methods [172, 173]. The implementation in the Insight Segmentation and registration Toolkit (ITK) [174], is heavily aimed at medical image segmentation and lacks support for non-convex HJE necessary for FIB simulations.

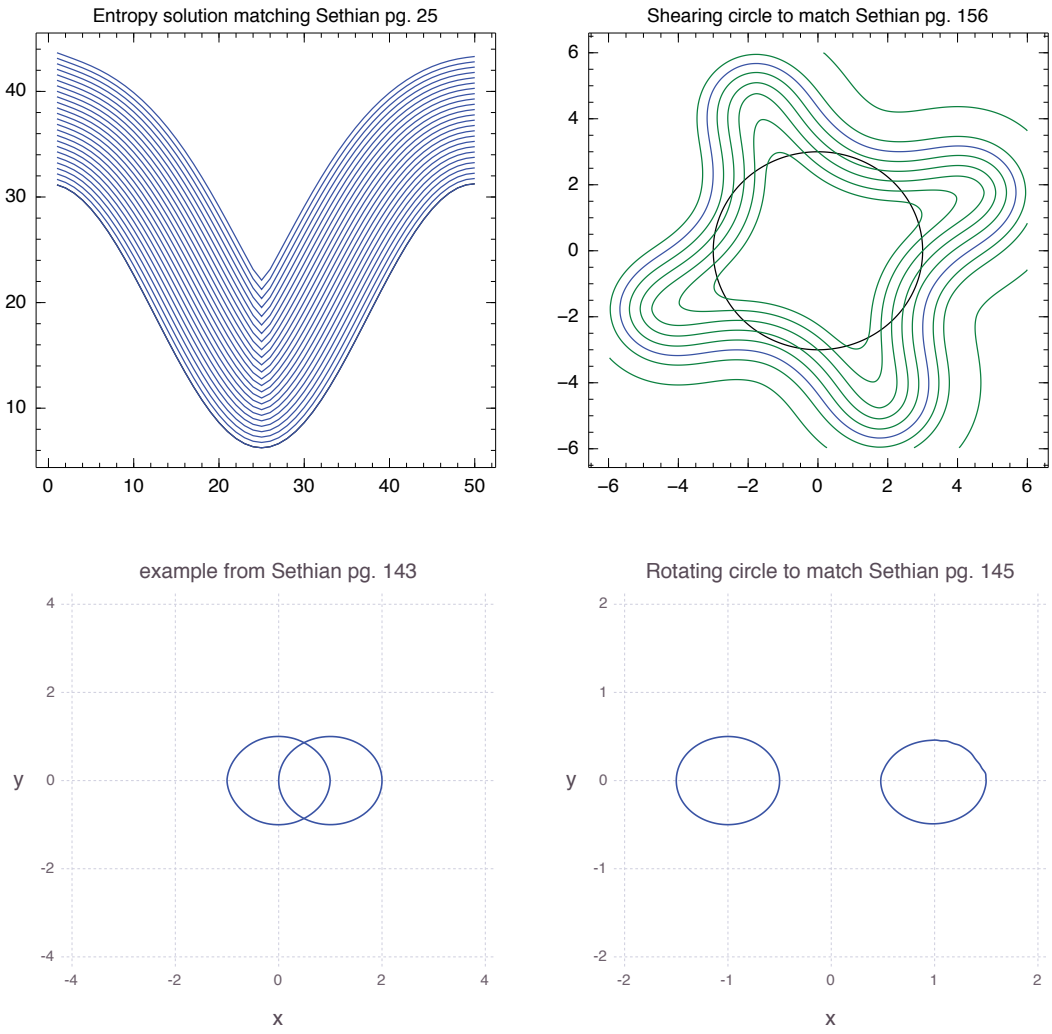

FIGURE 3.8: Verification of the implementation of the LSM using a first-order convex scheme. **Top left** shows the correct entropy solution for a cosine front evolving upward with speed $F = 1$. **Top right** shows an initially circular level set ($\phi = 0$ yields the black circle) evolving with a surface speed $F = ((R-3)^2 + 1) \cdot (2 + \sin(4\theta))$ using the extension velocity (instead of reinitialization) to correctly maintain the front (blue) and the neighbouring level sets (green). **Bottom left** shows the translation of a circle using $F = (1, 0) \cdot \frac{\nabla\phi}{|\nabla\phi|}$ from (1,0) to the origin. **Bottom right** shows solid body rotation of a circle about the origin using $F = (-y, x) \cdot \frac{\nabla\phi}{|\nabla\phi|}$ from (-1,0) to (1,0). Page numbers are listed from [166] for comparable descriptions and plots.

The 2D code was tested by duplicating known results from the literature. This included the correct evolution of a cusp, a translation and a rotation of a circular interface from [175], see Figure 3.8. A FIB sputtering example comparing the usage of convex versus non-convex Hamiltonian was also run [176, 177], see Figure 3.9.

With the 2D LSM proven, a 3D LSM was built for use in full 3D surface evolution simulations.

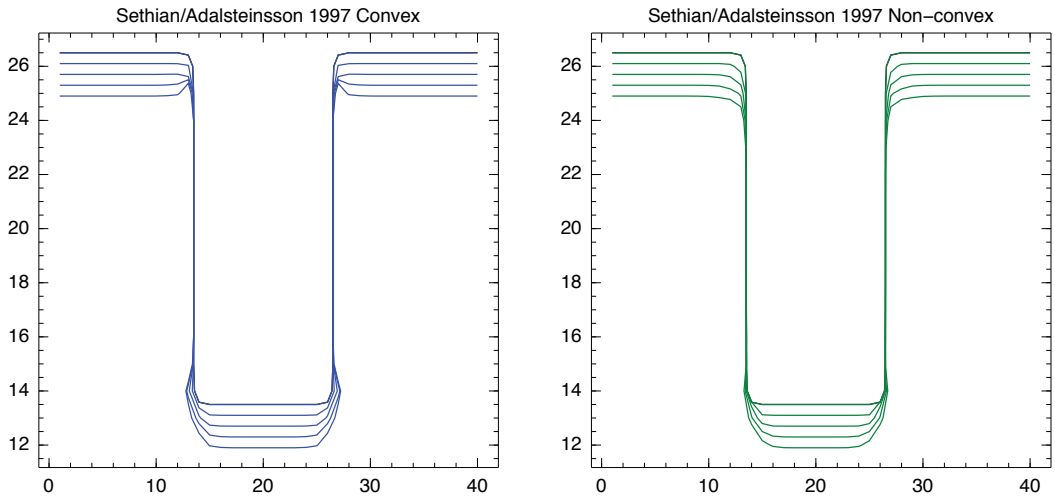

FIGURE 3.9: Verification of the implementation of LSM in the case of FIB sputtering using a first-order non-convex scheme. An analytic approximation is used for sputter yield which generates the speed $F = [1 + 4\sin^2(\theta)]\cos(\theta)$. **Left** plot shows convex scheme demonstrates the incorrect evolution (blue) while the **right** plot with a non-convex scheme demonstrates the correct evolution (green).

The first applied use was for anisotropic diamond etching, as shown in this chapter, and then to EBID (see Chapter 4). The code can easily be modified to simulate FIB milling and deposition.

3.4 Diamond etch model implementation

This section contains part of the supplemental information for the publication *Dynamic pattern formation in electron beam induced etching* [94] from Section 3.1 and explains how the speed function was developed, the etch kinetics verified, and the simulation performed.

3.4.1 Etch rate anisotropy

The level set speed F is given by the etch rate R of the diamond crystal for the normal direction of the surface

$$F = R(\theta, \Phi) \tag{3.20}$$

where the usual definitions for polar angle θ taken from the positive z-axis, and azimuthal angle Φ around the xy-plane apply. The etch rate in any direction can be determined by interpolation

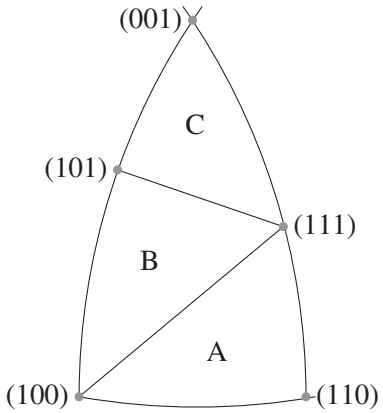

FIGURE 3.10: Etch rate regions A, B, C, defined in 1/16 of the sphere completely determine (by symmetry) the etch rate in any direction.

from a set of crystalline direction etch rates [83–89]. With the etch rates of the $\{100\}$, $\{110\}$, and $\{111\}$ planes defined as R_{100}, R_{110}, and R_{111} respectively, R becomes (see Radjenović [87])

$$R(\theta,\Phi) = \begin{cases} R_{100} - (R_{110} - R_{111})\cot(\theta)/\cos(\Phi) + (R_{110} - R_{100})\tan(\Phi) \in A \\ R_{100} + (R_{110} - R_{100})\cot(\theta)/\cos(\Phi) + (R_{111} - R_{110})\tan(\Phi) \in B \\ R_{100} + [(R_{110} - R_{100})\cos(\Phi) + (R_{111} - R_{110})\sin(\Phi)]\tan(\theta) \in C \end{cases} \tag{3.21}$$

where the regions A, B, C are defined in Figure 3.10.

3.4.2 Simulation verification

The LSM surface evolution implementation driven by interpolated etch rate is verified by simulation of crystal spheres etching inward and spherical voids etching outward. The evolution of the structures obey etch kinetic theory that states "*convex surfaces are confined by rapidly dissolving planes, and concave surfaces by slowly dissolving planes*." [178]. By setting one etch rate to be fast and all others slow, spheres etch down to the correct polyhedra defined by those planes, e.g., $\{001\}$ planes etching fast forms a cube. By reversing these conditions, i.e., setting one etch rate slow and all others fast, voids in crystal etch out to the same polyhedra, see Figure 3.11 (images and videos generated using the LSM code were rendered using ParaView [179]).

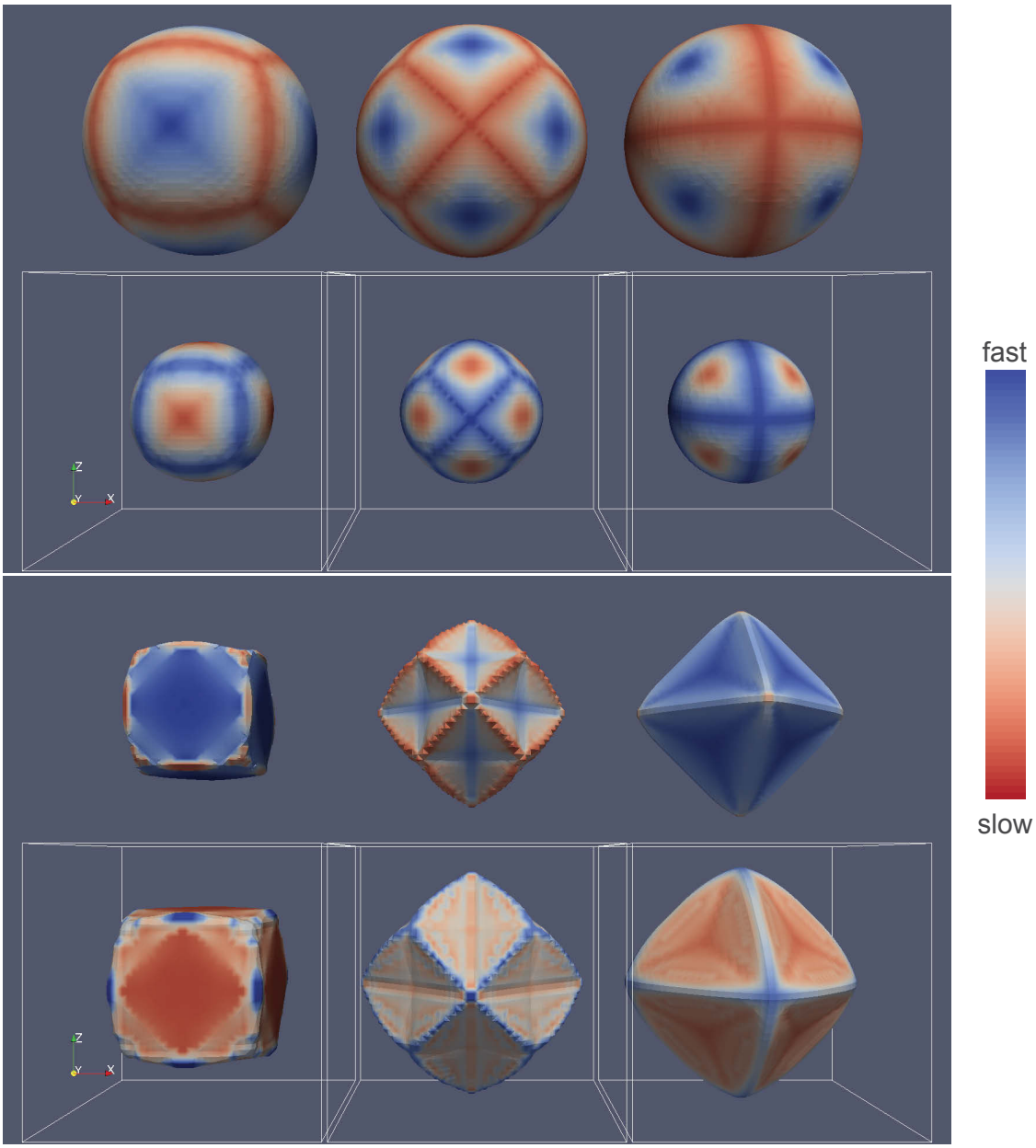

FIGURE 3.11: Verification of the implementation of LSM with etch rate interpolation on spheres etching in and spherical voids (or bubbles) etching out. **Top** the first two rows show initial conditions of spheres and voids, and **bottom** the last two rows show final conditions of the same. Red indicates slow etching and blue fast etching. The three columns of the spheres (and voids) show the $\{001\}$, $\{011\}$, and $\{111\}$ planes etching fastest (and slowest).

Precursor	Crystal orientation	Slow etch planes
H_2O	(001)	110 (at $\theta = 90°$)
H_2O	(111)	110
NH_3	(001)	111
NH_3	(111)	111

TABLE 3.1: Simulation etch rates for different diamond crystal orientation and precursors. Etch rates are either "fast" or "slow". The ratio of the fast etch rate to the slow is always 1:5 (slower ratios of 1:10, 1:100, make no significant difference).

3.4.3 Determination of anisotropic etch rates

The etch pit shapes observed experimentally were reproduced using LSM simulations only if:

- The $\{111\}$ planes etched slower than all other planes in the case of NH_3 EBIE of (100) and (111) oriented diamond (see Figure 3.10).
- The $\{110\}$ planes which are at $\theta = 45$ degrees with respect to the electron beam axis etched the slowest in the case of H_2O EBIE of (100) and (111) oriented diamond (see Figure 3.12(a)).

The above anisotropy rule set is summarized in Table 3.1.

The initial surface in each simulation was a concave hemispherical etch pit in a flat plane (Figure 3.12(b)). This isotropic starting point ensures that the final evolved surface geometry is defined purely by the etch rate anisotropy.

Note that during EBIE of (001) oriented diamond, the electron beam is incident onto two sets of (110) planes, at polar angles θ of 45°and 90°. In the case of H_2O EBIE (where the etch pit shapes are defined by the etch rate of (110) planes), the 45° planes etch slower than the 90° planes. This is likely caused by preferential defect incorporation during chemical vapour deposition of diamond [180].

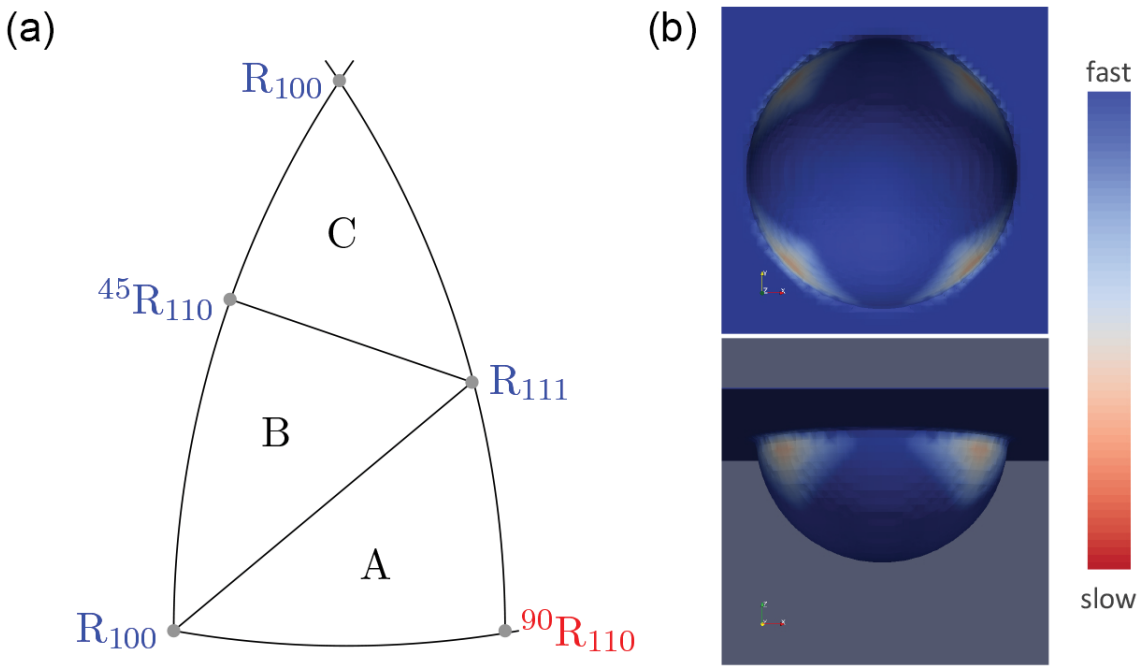

FIGURE 3.12: **(a)** The scheme used to implement H_2O EBIE of diamond. The colour red indicates slow etching direction and blue fast etching. **(b)** Corresponding initial voids coloured by relative etch speed.

3.5 Conclusions

In this chapter we have developed and verified code for a robust 2D and 3D surface evolution technique by employing the level set method. Here the level set method represents the most elegant choice for evolving the diamond etch pits under a given velocity field. Furthermore, this method can handle the difficult issues posed by merging and separation of surfaces. It works very well in three dimensions which is the natural domain of interesting surface patterns. Finally, the concept of the implicit surface is easily combined with both 1) the Ion-Solid-Interactions model (see Appendix A), which often needs to know the distance to the surface (to determine if the moving particle is inside or outside), and with 2) the closest point method, which is used to compute adsorbate kinetics to steady state as described next in Chapter 4.

Chapter 4

Adsorbate kinetics modelling

This chapter presents a new model for tracking adsorbate kinetics on general surfaces[1]. This method is built on two techniques: 1) generalizing the continuum model for adsorbate kinetics, and 2) solving the reaction-diffusion partial differential equation(s) for the adsorbates using the closest point method. At the end of this chapter these two techniques are combined with the surface evolution technique of the level set method into a new state-of-the-art electron and ion beam induced deposition (EBIED / IBIED) modelling method. This tool set shares a common implicit surface representation throughout and it solves the core problem of the thesis, that of evolving surfaces and solving EBIED / IBIED reaction-diffusion equations on surfaces. By way of example, the tool set is applied specifically to simulate surface evolution (deposition) in mass transport limited and reaction rate limited regimes.

The core idea for the continuum concentration model for adsorbates comes from the literature. The framework generalization of this model to handle various species and definitions of addition and diffusion are mine. The closest point method and algorithm come from the literature. The implementation and application to adsorbate kinetics on evolving surfaces are mine, as well as the modelling and results.

Section 4.1 introduces the continuum equation for adsorbates, and shows how it can be generalized for multiple species or surface interaction modes. Section 4.2 reviews some of the existing techniques for solving partial differential equations (PDEs) on curved surfaces. Section 4.3 focuses on

[1] By *general surface*, we mean a surface of any shape, that is, not necessarily flat, nor symmetric.

the technique chosen for evolving the adsorbate continuum equation on a general surface, and the closest point method (CPM) while Section 4.4 describes the implementation. Section 4.5 solves the issue of combining these two techniques and applying them to mass transport limited and reaction rate limited situations. The benefits of this new state-of-the-art EBIED / IBIED modelling method are concluded in Section 4.6.

4.1 EBIED / IBIED PDE definition

The typical EBIED / IBIED equation for adsorbate kinetics tracks adsorbate concentration N on a surface

$$\frac{\partial N}{\partial t} = A - R + D\nabla_S^2 N \tag{4.1}$$

where the arrival A onto the surface depends on coverage, partial pressure, and precursor gas delivery nozzle position, the removal R depends on desorption rates and ion / electron flux on parts of the surface, and the transport is given by diffusion. All of these terms have units of flux and they are dependant on the shape of the surface, which may be initially flat, but will be altered over time by etching or deposition.

Here (4.1) is a second order partial differential equation, which is *parabolic* and *inhomogeneous*. More specifically, it is a diffusion equation with source and sink terms. By including many adsorbate species and adsorption conditions, it may form a system of equations, see Appendix B.

Analytically solving PDEs on a generalized surface is a mathematical challenge, even in one dimension. By *generalized surface* we mean surfaces which may not conform to a regular coordinate system, as is generally assumed in *differential geometry*. The gradient ∇ and divergence of the gradient (Laplacian) $\nabla^2 \equiv \Delta$ are well known in Cartesian, cylindrical, spherical and other "uniform" coordinate systems. On general surfaces, the gradient is the *intrinsic gradient* ∇_S, and the Laplacian is the *intrinsic Laplacian* Δ_S also known as the Laplace-Beltrami operator. These naturally extend the regular coordinate system definition, taking the local coordinate system into account.

A further complication can be introduced by the evolution speed of the surface on which the PDE is being solved. For a *dynamic surface* evolving at a rate comparable to the time frame of the

diffusion equation, the PDE values will be affected. A *quasi-static surface* where the surface changes are slow compared to the adsorbate kinetics, allows for a two-step approach where 1) the adsorbate PDE is solved to convergence, and then 2) surface evolution is driven forward, and then the PDE is solved again, etc. In the modelling of Section 4.5 this quasi-static approach is taken.

4.2 Techniques for solving PDEs on surfaces

4.2.1 Explicit surface techniques

While there has been development of finite element methods (FEM) for solving PDEs (a good review is given by Dziuk [181], and a recent example of solving a PDE on an evolving surface is given by Madzvamuse [182]), there are still many issues. As discussed in [93], the efficient *parametrization methods* still result in complicated formulas and singularities which must be handled specially, with the cost of substantial organizational complexity. *Finite element methods* (FEM) and *finite volume methods* (FVM) define the surface as a mesh (or *polyhedral triangulation*), and require a "deceptively difficult" [93] discretization of the PDEs including complexities inherent in deciding what normal and curvature values should be. The *discontinuous Galerkin method*, which relies on a combination of both FEM and FVM, can also support surface diffusion, however, application is complicated [183, 184].

4.2.2 Implicit surface techniques

Bertalmio [185] pioneered an approach to solving a PDE on an implicit surface. Using the surface's level set and surface data extended to a Cartesian grid, the PDEs can be evolved on a regular grid. The method of extending the original data on the surface to the 3D volume is the same as used for the extension velocity by Adalsteinsson [160] (as mentioned in Subsection 3.2.7), and is attributed originally to Chen [186].

Greer [187] improved this method by a simple redefinition of the projection operator used when extending the surface data to the volume. This removed the need for reinitialization of the level set and clarified the boundary conditions necessary to solve the PDE.

4.2.3 The closest point method technique

The *closest point method* (CPM) by Ruuth and Merriman [90] (see Section 4.3) moved away from the level set embedding, with further benefits. It defines a method to simplify the solution of a PDE on a manifold by replacing the problem with another PDE in the embedding space whose solution will match on the surface. Macdonald [188] notably advanced the closest point method to handle implicit time evolution, which makes it able to handle larger time steps, speeding up simulations. Macdonald also investigated solving for interfaces on general surfaces (using the level set method PDE and embedding it via the closest point method) [91].

For its mathematical elegance and algorithmic simplicity, the closest point method was chosen to implement for evaluation of the adsorbate kinetics PDEs.

4.2.4 Other applications of CPM

The closest point method has been used to visualize flows on surfaces [189]. Biddle and Naden have demonstrated noise removal from images on curved surfaces [190, 191], and Tian demonstrated segmentation on curved surfaces [192]. Marz has investigated applications to thin film flow [193]. The principle introduced by CPM, that "standard Cartesian derivatives equal surface derivatives if the quantity of interest is constant in the normal direction" is used in the Kolahdouz model of vesicle membrane voltages [194] where tension and transmembrane potential are computed [195, 196].

4.2.5 Recent developments with CPM

Improvements to the performance of the CPM are still being made [197]. Chen has shown that for larger surfaces in 3D, a multigrid approach is available that dramatically reduces the computation time [198]. Fuseiler [199] attempted to improve upon CPM by using a kernel approach, but with an $O(N^2)$ computation penalty. Auer [200] has implemented the CPM in a graphics processing unit (GPU) application programming interface (API) (called CUDA) pipeline to simulate fluid effects on surfaces by the Navier-Stokes and wave equations.

4.3 Closest point method

The closest point method is a technique to evolve partial differential equations on general surfaces. It defines a new PDE in an embedding Cartesian space whose solutions agree on the original surface. Thus, the closest point method represents the surface implicitly, as does the level set method. The CPM originated in 2008 by Ruuth and Merriman in a time-explicit form [90], was advanced to handle implicit time[2] evolution in 2010 by Macdonald [91, 92, 188], and has since been generalized for variable coefficient and non-linear PDEs [197].

The core idea in the closest point method is that surface derivatives are simply Cartesian derivatives which drop the normal components [201]. For example, given a surface $\mathcal{S}$, for a scalar function u on this surface (say, adsorbate concentration), there exists a coordinate system (n, t_1, t_2), see Figure 4.1, such that the Cartesian gradient

$$\nabla u = \frac{\partial u}{\partial n}\vec{n} + \frac{\partial u}{\partial t_1}\vec{t_1} + \frac{\partial u}{\partial t_2}\vec{t_2} \tag{4.2}$$

and the intrinsic gradient

$$\nabla_{\mathcal{S}} u = \frac{\partial u}{\partial t_1}\vec{t_1} + \frac{\partial u}{\partial t_2}\vec{t_2} \tag{4.3}$$

agree along the surface. For a vector property $\vec{v}$ the intrinsic divergence is

$$\nabla_{\mathcal{S}} \cdot \vec{v} = \frac{\partial v_1}{\partial t_1} + \frac{\partial v_2}{\partial t_2} \tag{4.4}$$

Applying the intrinsic divergence on (4.3), yields the intrinsic Laplacian (the Laplace-Beltrami operator)

$$\Delta_{\mathcal{S}} u = \nabla_{\mathcal{S}} \cdot \nabla_{\mathcal{S}} u = \frac{\partial^2 u}{\partial t_1^2} + \frac{\partial^2 u}{\partial t_2^2} \tag{4.5}$$

The implication is that if we extend a surface function, u, in the normal direction, then solutions to differential equations of u on the surface are given by an equivalent Cartesian differential equation. The dramatic advantage of this is that in Cartesian space, all the proven tools for numerically solving PDEs are now at our disposal. Whenever we are ready to view the solution on the curve,

[2]Note that there are two uses of the words "implicit" and "explicit" now being employed. Implicit and explicit surfaces refer to the spatial representation, while implicit and explicit time integration refers to the mathematical method to solve a PDE system at a later time. PDEs that require an implicit time integration approach are generally referred to as *stiff*.

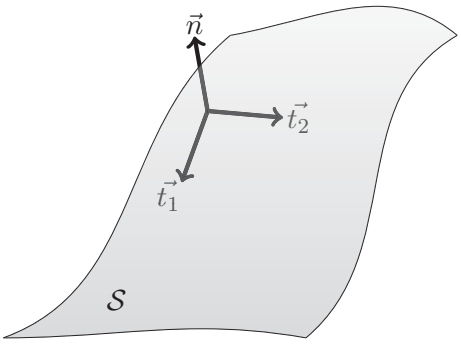

FIGURE 4.1: Schematic of surface $\mathcal{S}$ with locally oriented basis such that $\vec{t_1}$ and $\vec{t_2}$ lie locally in the surface and $\vec{n}$ is normal. Adapted from [201].

interpolation on the Cartesian grid to the surface will yield the present value of the surface function, see Figure 4.2. For full details, see [90].

Depending on the differential order of the PDE, there is a minimal degree of interpolant that is required. Above this minimum, the choice of interpolation method to use is free, however there is a natural trade off between accuracy and computation time. Studies of CPM show that a four point (which is third degree $p = 3$), dimension by dimension barycentric Lagrange interpolation is satisfactory for 3D simulations on surfaces [188]. This 4x4 interpolation stencil is implemented for this work.

The extension of surface data to the Cartesian embedding out along the normal is performed by introducing the closest point operator cp(**x**). This operator maps any point **x** to the point on the surface that is closest to **x**, see Figure 4.3. The surface function u is extended over all space by applying u(**x**) = u(cp(**x**)). The equivalent Cartesian PDE is formed by replacing all points **x** with $cp(\mathbf{x})$, and all intrinsic operators with Cartesian equivalents. For example, a simple diffusion equation on the surface (with initial condition)

$$\frac{\partial u(\mathbf{x})}{\partial t} = D\Delta_{\mathcal{S}} u(\mathbf{x}) \qquad u_0(\mathbf{x}) = u(\mathbf{x}, 0) \tag{4.6}$$

becomes

$$\frac{\partial u(cp(\mathbf{x}))}{\partial t} = D\Delta u(cp(\mathbf{x})) \qquad u_0(\mathbf{x}) = u(cp(\mathbf{x}), 0) \tag{4.7}$$

where (4.7) can be used to derive effective algorithms. These algorithms will need to ensure that u stays constant in the normal direction as the solution evolves.

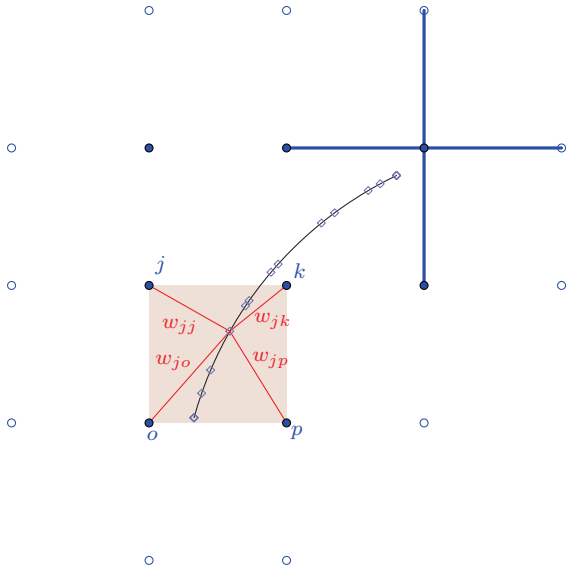

FIGURE 4.2: Illustration of a curve through space, within its computation band of Cartesian grid points. The solid grid points are used for interpolation of the solution back to the curve, the hollow points indicate the boundary required for computation of the 5-point Laplacian stencil (example shown with blue lines). The closest points on the curve for all grid points are shown as diamonds. A 2x2 interpolation stencil is illustrated in red. The value of function u on the curve is determined by interpolation of the values of u on the points (j,k,o,p) and their weights. Specifically the closest point on the curve to j, denoted cp(j), is determined by the weights $(w_{jj}, w_{jk}, w_{jo}, w_{jp})$ as indicated by the red lines.

Every grid point **x** derives its value from the corresponding mapped point on the curve cp(**x**). Every point on the curve can be determined by interpolation from the local grid. This combination of relationships can be mathematically captured in a sparse matrix, called the *extension matrix* E, see the next section.

4.4 Implementation and verification of CPM

To implement the integration of a surface PDE, a *computational band* must be identified in the Cartesian space that encompasses the surface. It must be large enough to support the interpolation desired and any discretized spatial differential operators, e.g., the 5 (7) point stencil for the 2D (3D) Laplacian. Macdonald specifies one algorithm for discovering the minimum set of points needed to carry out the computation [188]. By beginning with a list of grid points comprised initially of one point x_1 known to be close to the surface, the algorithm progressively finds the closest point

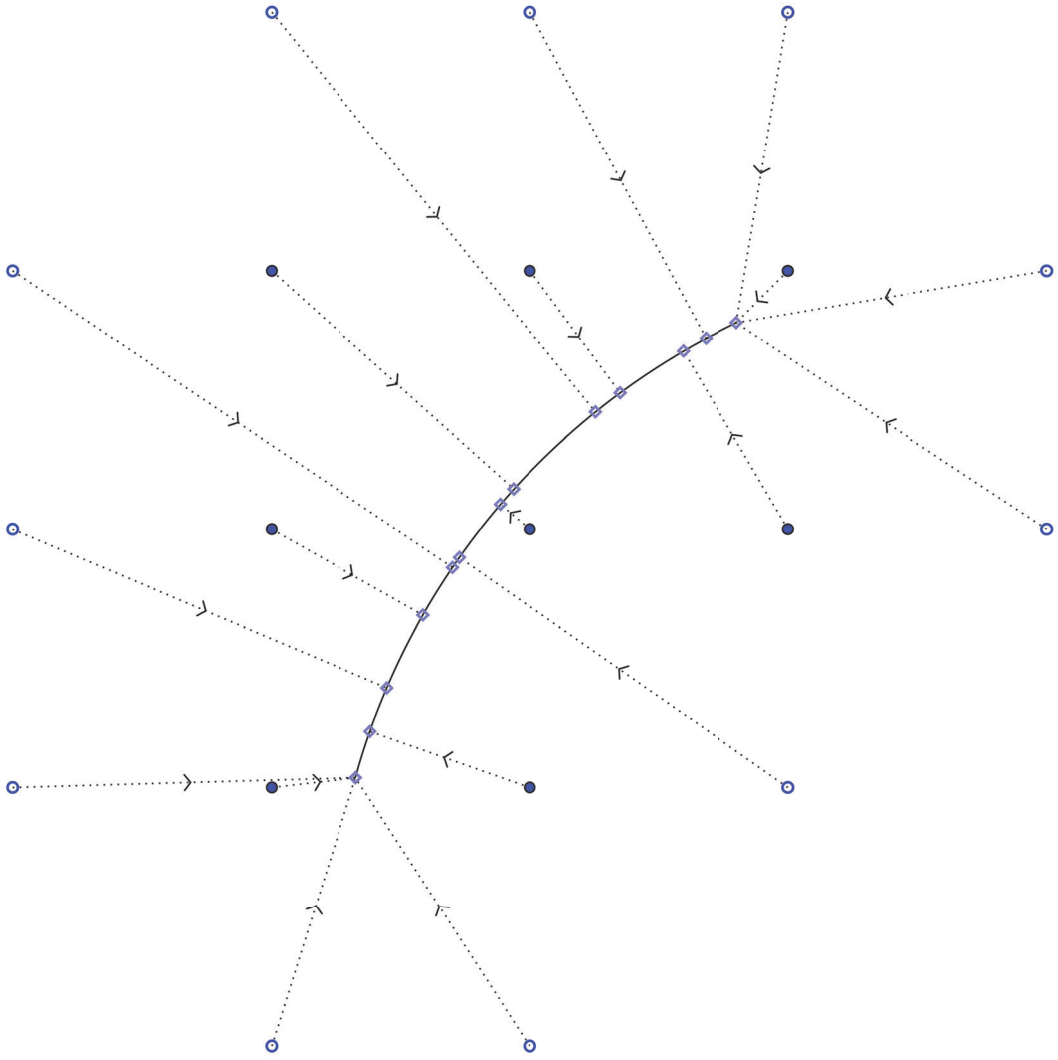

FIGURE 4.3: Example of the closest point operator cp(**x**) on several local grid points in the computation band (a.k.a. a "porcupine" plot). Note that all extensions from **x** on the interior of the curve are normals of the curve at cp(**x**).

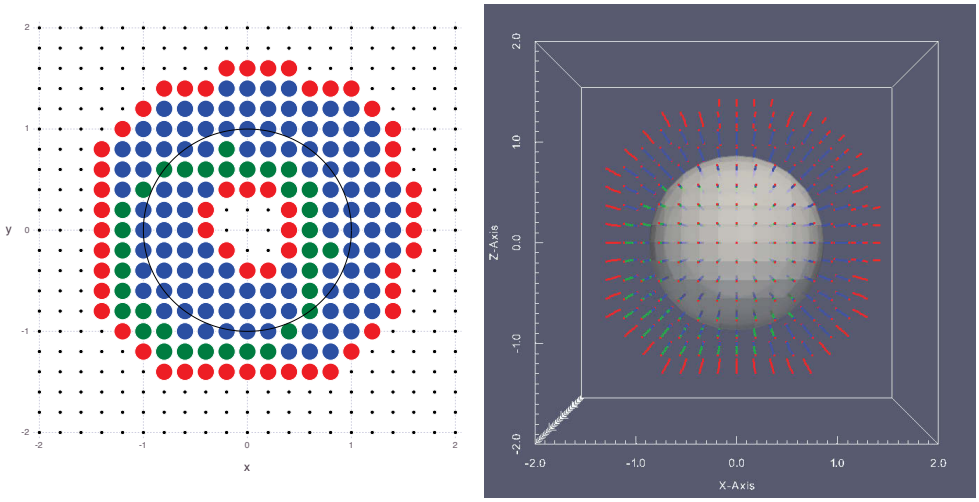

FIGURE 4.4: Intermediate results from the simulation correctly identify the computation band. It encompasses the surface (**left** 2D circle and **right** 3D sphere) and is comprised of two sets of points, set L has m points (blue and green) and set G has n points (red). The base points (green) are the lower corners of the 4x4 interpolation stencil.

$cp(x_1)$ on the surface, and adds to the list all the (new) grid points needed to interpolate properly to that closest point. The process is repeated until no new points are added. This forms the band of points L. Additionally, a set of "ghost" points that are required for any second order central difference are added, band G. The computational band is comprised of the union of two sets of points, named L with m members and G with n members, see Figure 4.4.

In an approach that is similar to any implicit time method for the heat equation (e.g. the Crank-Nicolson method), the relationships arising from the discretized Laplacian can be arranged into a sparse matrix of size $(m+n)\times m$ named Δ_h. The closest point mapping and interpolation are also expressed in a sparse matrix $m \times (m+n)$ named E, the *extension matrix*. The product of these two matrices is $m \times m$ matrix $\Delta_h \times E = \widetilde{M}$, see Figure 4.5. This matrix can then be integrated forward in time to solve the diffusion equation.

However, one adjustment must happen first. The matrix $\widetilde{M}$ was shown to be unstable by eigenvalue analysis. It has also been shown that this instability can be eliminated without compromising the correct solution by removing an unnecessary re-mapping in the Laplacian [188]. (This method was reformulated recently by von Glehn et al. [197] in a form that allowed for clearer analysis of convergence.) The former approach has been taken in the implementation, and to verify, eigenvalue analysis for numerical stability is performed, see Figure 4.6.

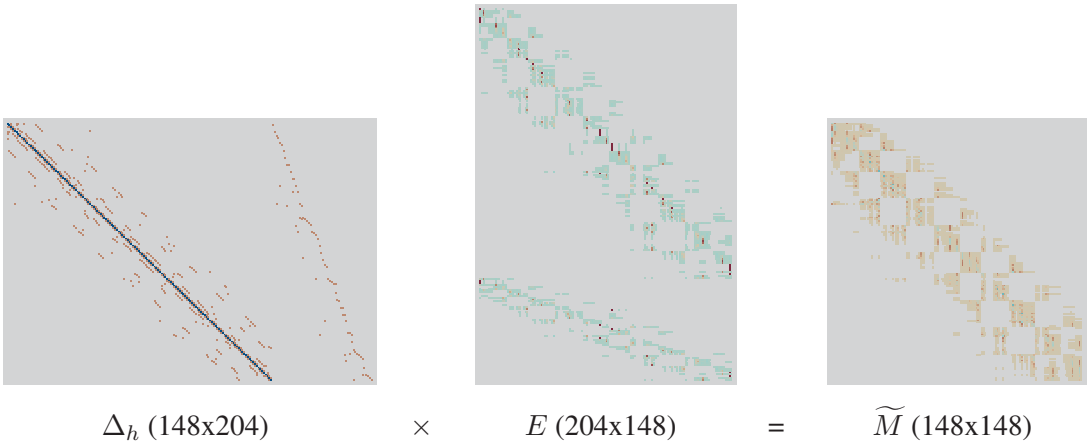

FIGURE 4.5: Visualization of the matrix equation $\Delta_h \times E = \widetilde{M}$. Intermediate results from the simulation correctly produce sparse matrices with many near-diagonal entries. The matrices capture the discretized Laplacian, Δ_h, the extension matrix, E, and their product $\widetilde{M}$ (148x148). The matrix visualization shows zeros as a uniform grey background, and non-zero values with colour. These match well with matrices from Macdonald's work, figure 3.1 in [188].

By stabilizing this stiff matrix for implicit time stepping, we have freedom to chose an algorithm for large time steps. Backward difference formulas (BDF) of order 1, 2, and 4 have all been shown to work [188], and BDF4 is implemented for best combination of accuracy and speed.

4.4.1 Implementation of diffusion

The code is implemented in Julia [202], see Appendix C. The performance is limited by the surface evolution loop, which repeatedly multiplies large sparse matrices with vectors. The Julia package `IterativeSolvers` has been used with the `gmres()` function to perform a generalized minimization of residuals. This optimizes the speed of performing the computation of $Ax = b$ (solving for x).

The results of the Julia code match the analytical results for the cases of heat diffusion on a 2D circle (shown) given in [187] and a 3D sphere (not shown), see Figure 4.7.

4.4.2 Implementation of sources and sinks

The implementation was tested with idealised sources and sinks such as might occur in adsorbate kinetics situations. Two simulations were run, one with a flat surface, and one with a Gaussian

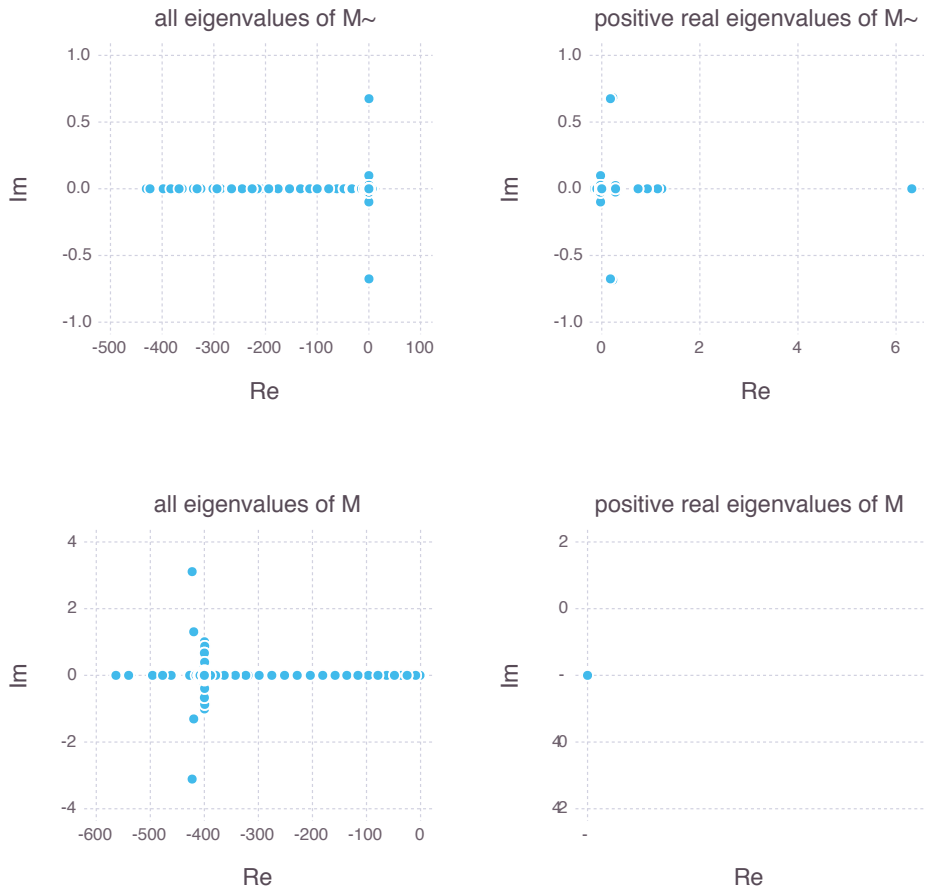

FIGURE 4.6: Plots of eigenvalues in the complex plane at differing scales show intermediate results from the matrix stabilization process. **Top** plots show eigenvalues for the unstable matrix $\widetilde{M}$ and a close-up of the positive real eigenvalues which are responsible for increasing instability. **Bottom** plots show results of the stabilized matrix M (because it has no positive real eigenvalues) by rewriting of the cp(**x**) mapping along the diagonal, c.f. Macdonald's figure 3.5 in [92], and see [92, 188] for details.

"etch pit". First on a flat surface it was demonstrated that diffusion from a source spread out evenly, until it encountered the domain edge (see Subsection 4.5.3 for details on boundary conditions), and then a sink was added to show the difference in concentration in the steady state, see Figure 4.8. Material which reached the domain edge was removed at a rate equivalent to the net flux into the system, allowing an equilibrium to be reached. Thereafter, the surface was altered so that a Gaussian pit (an etch pit) corresponded to the sink location, and the simulation was run again to a steady state, see Figure 4.9. In both cases, the concentration profiles at the steady state were as expected. The addition of a sink to the flat surface pinched the contours around the sink. The

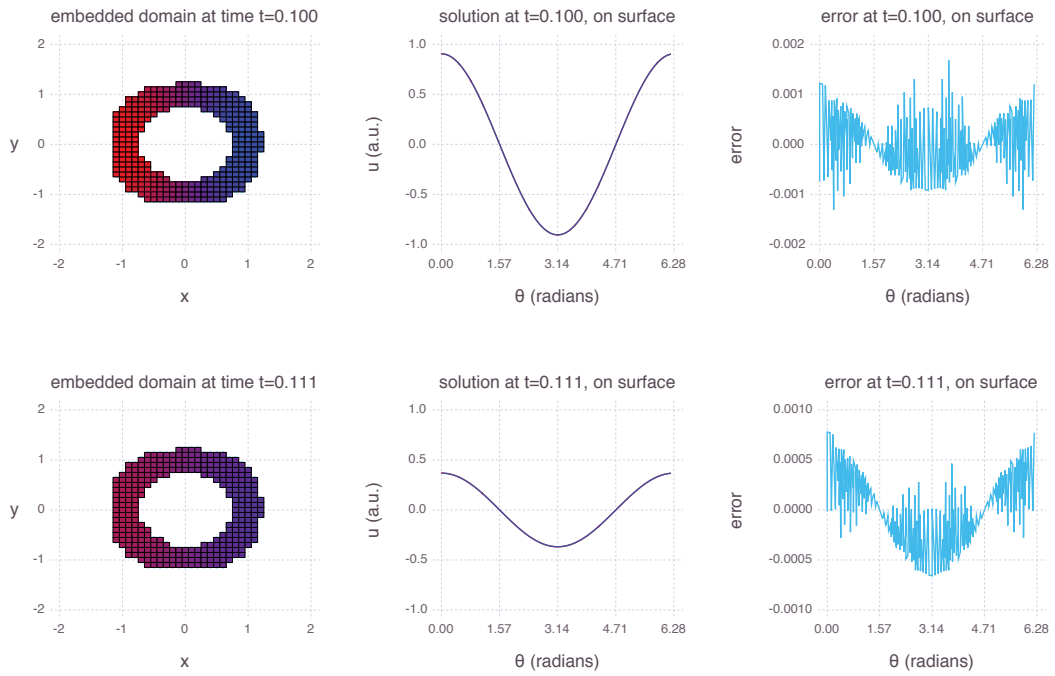

FIGURE 4.7: Validation of the CPM implementation by solving for heat diffusion on a circle. **Top** shows the beginning and **Bottom** shows the ending heat distribution on a unit circle. **Left** shows the computational grid surrounding the circle, with each point coloured by its heat value. **Middle** plot compares the computed u (red) with analytic solution $e^{-t}\cos(\theta)$ (blue), however they lie so close as to be indistinguishable. **Right** plots the difference between computed and analytic as a measure of the error.

warping of the surface eased the pinching, as there was now more surface area on which diffusion could take place.

Having verified the CPM implementation for solving reaction-diffusion problems of adsorbate kinetics on fixed general surfaces, it can now be used in conjunction with surface evolution to simulate deposition on evolving surfaces.

4.5 Simulating adsorbate deposition

By now combining the tool to compute (4.1) for adsorbate surface diffusion (CPM) with that to compute surface evolution (LSM), a model can be built to simulate deposition.

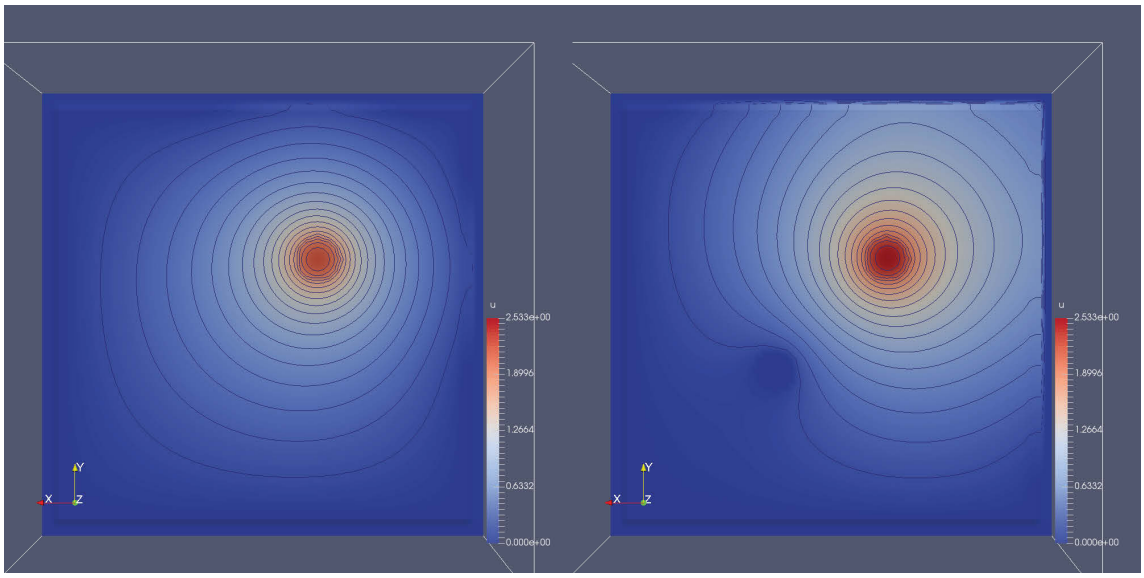

FIGURE 4.8: Modelling of diffusion of adsorbates on a flat surface to the steady state by the closest point method. **Left** with only a source of adsorbates (uniform flux 20 a.u. in a circular region radius of 0.2 a.u.). **Right** with the addition of a sink for adsorbates (uniform flux -10 a.u. in a circular region radius of 0.2 a.u.). Colour and contours indicate the relative concentration of the adsorbates. Boundary conditions were set such that in the steady state, the net flux into the simulation was zeroed. These simulations are on a grid of 80x80 and take about 5 minutes to run on a 2012 MacBook Pro.

4.5.1 Steady state assumption

Modelling the mass transport limited regime requires modelling surface evolution with adsorbate kinetics. One key assumption is necessary, that the surface is moving slowly compared with the evolution of the adsorbate's PDE. In other words, the adsorbate PDE is always assumed to reach a steady state before the surface is evolved by one step. The simulation then proceeds by alternating between modelling adsorbate kinetics and modelling surface evolution by first computing diffusion with the CPM to a steady state and then evolution for a short time period (one time step) with the LSM.

4.5.2 Deriving closest points on implicit surface from ϕ

Initializing the closest point method requires computing the closest point on the implicit surface for every grid point in the computational band using the values of the level set function ϕ. As long as ϕ is well-maintained as the signed distance function during evolution (as can be accomplished

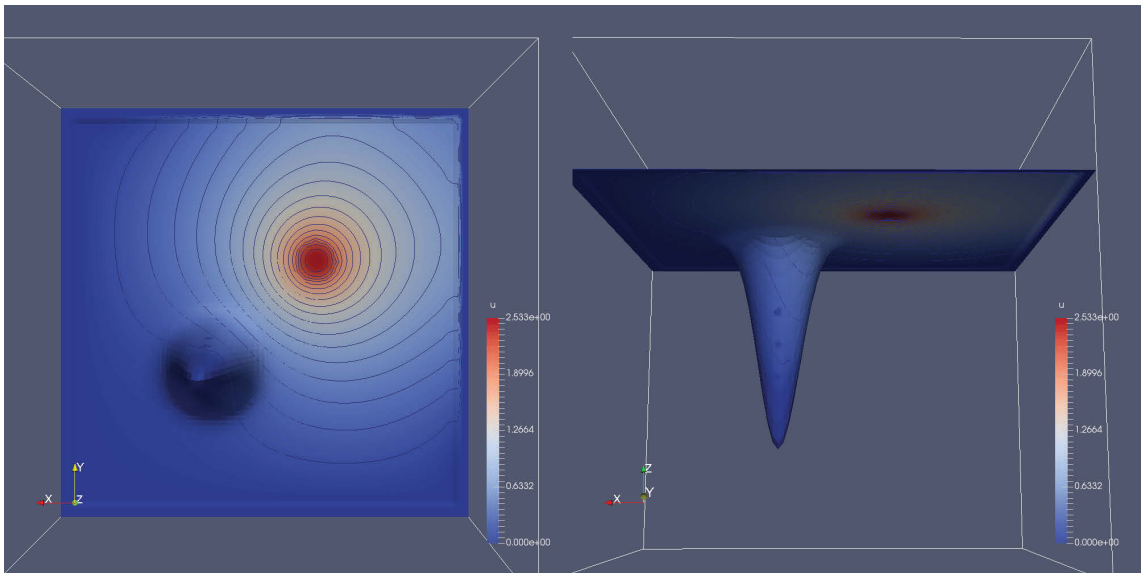

FIGURE 4.9: Modelling of diffusion of adsorbates on a flat surface with a Gaussian pit to the steady state by the closest point method. The source is a uniform flux 20 a.u. in a circular region radius of 0.2 a.u. and the sink is a uniform flux -10 a.u. in a circular region radius of 0.2 a.u. **Left** shows a top-down view. **Right** shows an angled view from underneath. Colour and contours indicate the relative concentration of the adsorbates. Boundary conditions were set such that in the steady state, the net flux into the simulation was zeroed. This simulation is on a grid of 80x80 and takes about 5 minutes to run on a 2012 MacBook Pro.

by the extension velocity, Subsection 3.2.7), the closest points can be computed from the normal $\nabla\phi$ and the distance to the surface ϕ. Evaluating these gives a vector from every grid point back to the closest point on the surface. The normal $\nabla\phi$ is computed by second-order central difference.

Experimentation shows that re-initialization of ϕ may also be required. Over time, the evolved level set produces a spread in the extrapolated closest points found for the implicit surface. The spread is within a single grid spacing and is a result of discretization artefacts creeping into the signed distance function. Testing found that the spread can be reduced by increasing the grid resolution and by reinitialization of the level set function ϕ, see Figure 4.10.

4.5.3 Ghost widths

At each CPM initialization step, when the computational band is determined, it is most convenient to inset the simulation so that the computational-band-seeking-algorithm never runs off the simulation domain edges. At the lateral edges of the simulation domain a number of ghost cells are added

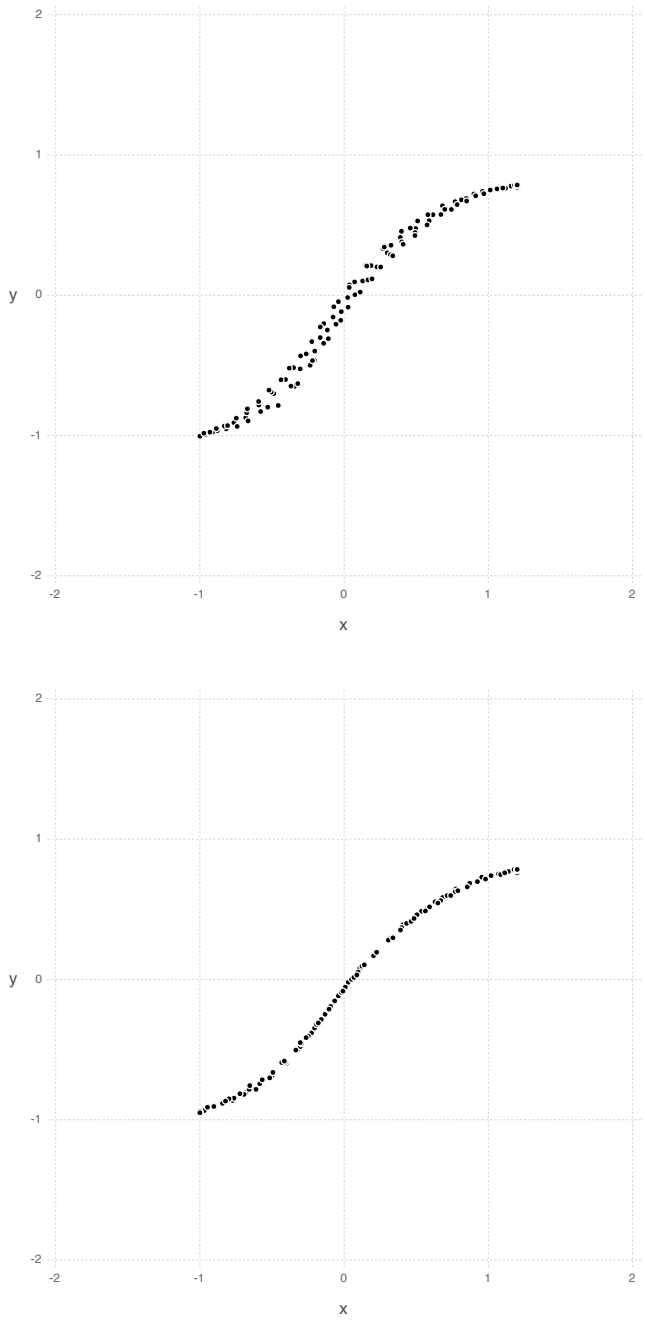

FIGURE 4.10: Illustration of the improvement of the CPM-LSM technique by reinitialization of ϕ after every surface evolution step. This example had an initially flat surface (at $y = -1$, not shown) that rose up asymmetrically producing a sinusoidal surface after many time steps (shown). **Top** without any reinitialization, the approximation of the closest points on the surface by ϕ exhibit a small spread over approximately one grid spacing. **Bottom** including reinitialization of ϕ before each CPM step maintains the surface sharpness. (As specified in Subsection 4.5.3 the surface and ϕ are defined over all x and the closest points of the surface do not extend into the ghost widths at $x < -1$ and $x > 1$.)

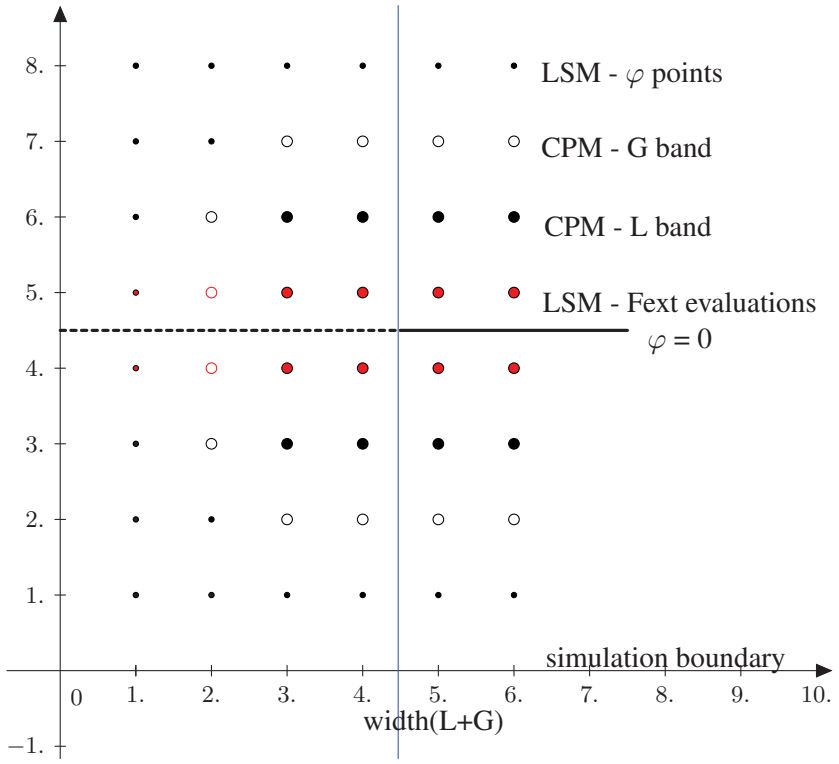

FIGURE 4.11: Illustration of ghost width for CPM initialization from ϕ in 2 dimensions. In our application, we assume the surface to extend and intersect the y-axis through the whole simulation. The level set ϕ must be extended so that the full L and G bands can be constructed and evaluated. In 3D ϕ is extended in both x and y, that is, we assume the simulated surface to reach the edges of the simulation.

to accommodate the CPM on ϕ. This ghost width is determined by the number of cells needed by the CPM interpolation, plus one for the CPM ghost band. By lateral edge, we mean the simulation domain walls which the surface intersects, e.g., in 2D with a flat simulation surface along y=1, the lateral edges are the two minimum and maximum x lines, in 3D with a flat simulation surface along z=1, the lateral edges are the four xy planes at x,y extrema.

In the ghost cells the value of ϕ is filled outward by copying it laterally. The closest point initialization is then also forced to laterally translate in by the ghost width, preventing any closest points to be found in the ghost width, see Figure 4.11.

4.5.4 Results

With the above adjustments, the CPM and LSM can be run serially (i.e., over and over), evolving surfaces based off of the steady state solution of a reaction-diffusion PDE. As an example to illustrate this proof-of-concept a beam induced deposition will now be run.

The simulation starts with a flat surface. A Gaussian beam which will "consume" adsorbates and create surface deposits is directed normal onto the surface, slightly off centre, so as to introduce an interesting asymmetry. The gas arrival rate determines the flux of adsorbates onto the surface. For simplicity, the conversion rate of the adsorbates to deposits under the beam is set to unity. Every time step, CPM computes the steady state concentration of adsorbates according to the arrival rate distribution (source) and beam conversion / consumption (sink). The steady state is determined *ad hoc* by performing false-time iterations. The LSM then advances the surface based on the conversion distribution, and the algorithm repeats. Some tuning of the size of the CPM false-time steps was done to insure that steady state was reached.

Three different distributions of gas arrival are run. First is a high uniform flux, which always provides more than enough adsorbates for the beam to deposit - this is known as the *reaction rate limited* regime. Second is a low uniform flux, which does not provide enough adsorbates for the beam flux. All adsorbates under the beam are immediately deposited, and diffusion allows an additional flow of adsorbates in from elsewhere in the domain. This is known as the *mass transport limited* regime. The third gas distribution is an off-centre Gaussian distribution which does not coincide with the beam (this is also mass transport limited). This asymmetric situation will cause deposition to happen only when adsorbates diffuse from the arrival site to a region with appreciable beam flux.

In two dimensions, results show the expected trends in behaviour. The first two deposits are symmetric, and the last asymmetric. The volume of the deposits decreases as the allowed consumption of adsorbates decreases, see Figure 4.12.

This example can also be run in three dimensions. This is one aspect where the power of the implicit methods shines - extending working 2D code to handle 3D is relatively trivial, compared with mesh-based methods.

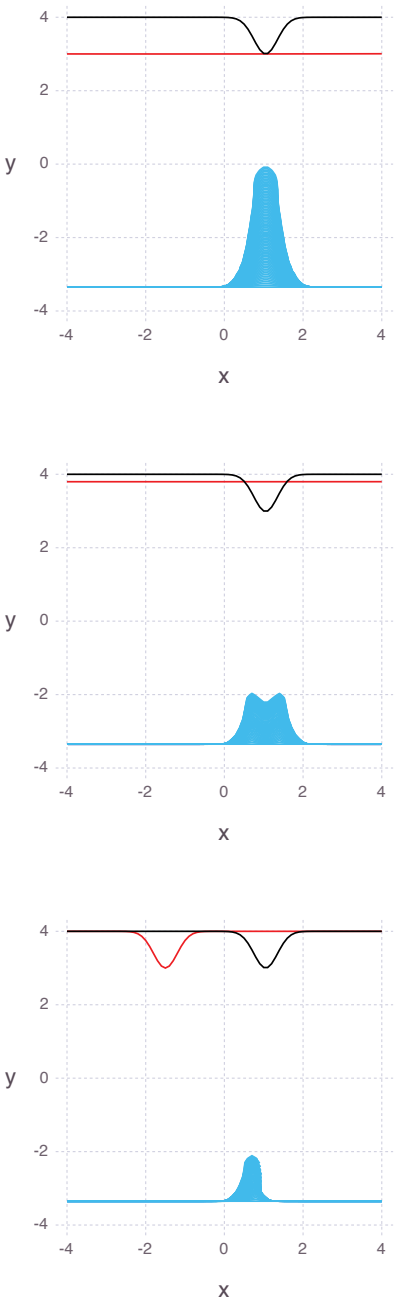

FIGURE 4.12: 2D illustration of deposit growth (blue) under different conditions of gas flux (red) and beam (black). **Top** a uniform gas flow and beam which does not deplete the adsorbates results in a symmetric deposit. **Centre** a condition where the beam is depleting the available precursor shows growth farther out due to adsorbates arriving via diffusion. **Bottom** an offset localized arrival of the gas (which could be a simulation of GIS arrival itself [102]) results in an asymmetric deposit. Domains here are 81x81 and all simulations ran in less than 10 seconds on a 2012 MacBook Pro.

In 3D, the results again show the expected trends in behaviour. Now however, in the asymmetric case, the deposit can be seen to form an even more interesting (and intuitive) crescent shape, see Figure 4.13.

4.6 Conclusions

This successful proof-of-concept demonstrates the natural capability of this approach. Etching could just as simply be performed as deposition. Features can be added on without much difficulty. More realistic beam profiles and gas arrival profiles are simply a matter of defining the distributions. Adding beam rastering is only a matter of shifting the location of the conversion around the surface. More complex adsorbate situations can be added into the PDE (see Appendix B). Non-local effects from the electron / ion interaction volume could be added with the appropriate Monte Carlo simulation (see Appendix A for ion solid interactions, also see Chapter 5).

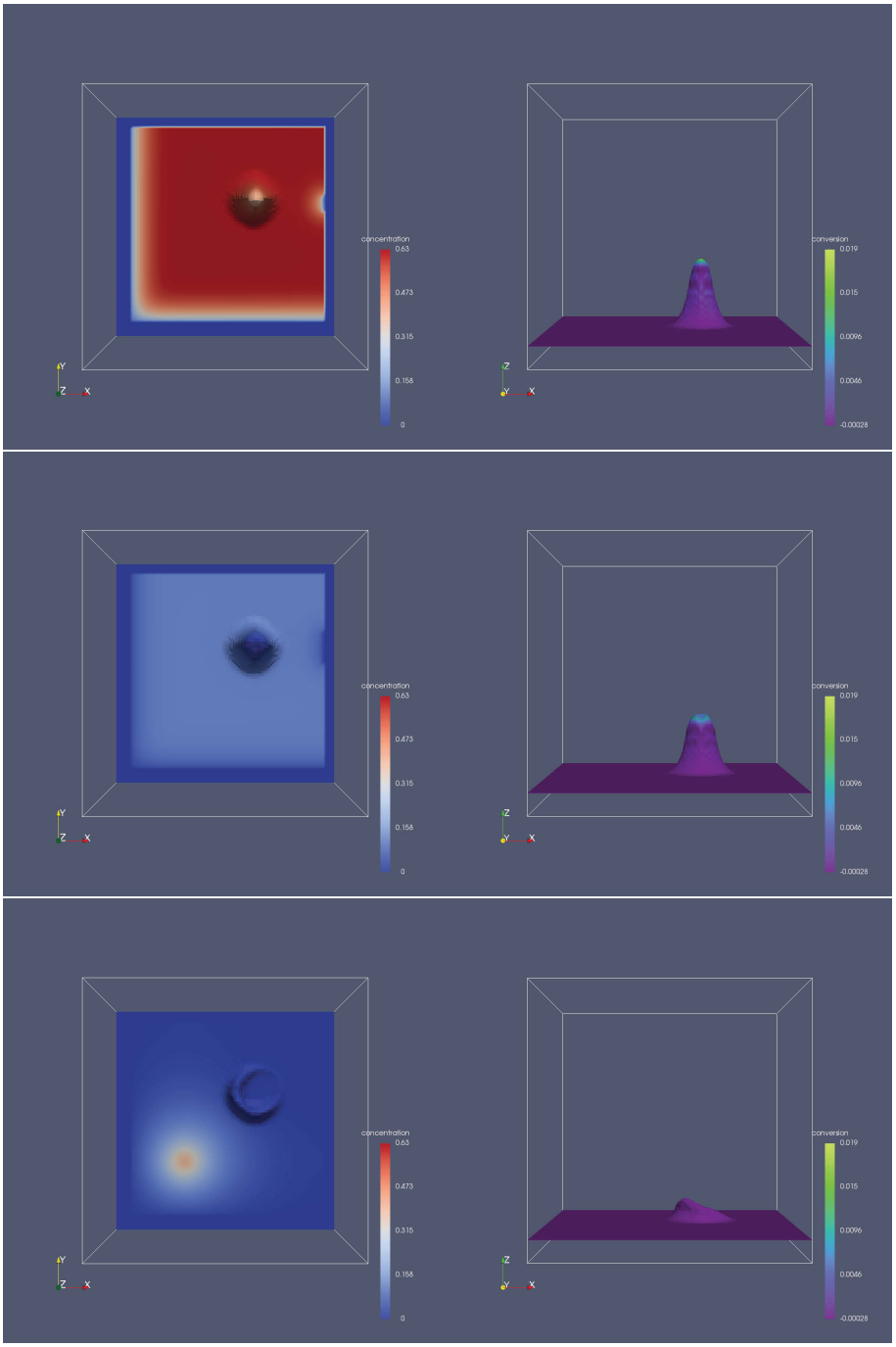

FIGURE 4.13: 3D illustration of deposit growth under different conditions of gas flux and beam. Each row of images shows the same surface and deposit coloured **left** by concentration of adsorbate on the surface and **right** by amount of adsorbate under the electron beam being converted to deposited material. (The border seen on simulations in the left view is an artefact from the rendering software). **Top** a uniform gas flow and beam which does not deplete the adsorbates results in a symmetric deposit. **Centre** a condition where the beam is depleting the available precursor shows growth farther out. **Bottom** an offset localized arrival of the gas (which could be a simulation of GIS arrival itself [102]) results in an asymmetric deposit.

Chapter 5

General conclusions and future directions

This chapter proposes an addition to the surface evolution and adsorbate continuum model outlined in the previous chapter, by including a Monte Carlo model (see Appendix A for details) which computes the electron / ion solid interaction as an input to the adsorbate kinetics partial differential equation (PDE).

Section 5.1 introduces the complete model, and Section 5.2 finishes with general conclusions.

5.1 Including sample interactions

Having demonstrated the closest point method (CPM) implementation for solving the problem of adsorbate kinetics PDEs in Chapter 4, it can now be used in conjunction with surface evolution (Chapter 3) and beam-sample interactions (Appendix A) to refine the tool set for simulating deposition and etching with a gas precursor on changing surfaces.

Simulations can be built using all three of the models implemented, in a cycle, each providing inputs to the next step. 1) The ion / electron sample interactions can be evaluated to determine the flux of particles across the surface and its effects on the adsorbates on the surface. This provides the source and sink terms in the adsorbate kinetics PDE(s). 2) For the solution of the PDE on

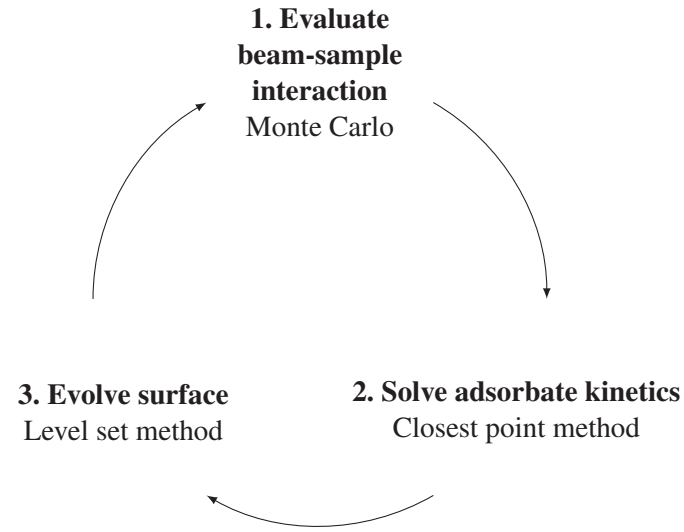

FIGURE 5.1: Schematic of approach for computing surface diffusion and evolution for electron and ion beam induced etching and deposition (EBIED / IBIED) over the whole surface. Fluxes from the beam and beam sample interaction are calculated to a "steady state" (until the statistics are significant) by a Monte Carlo based method (Appendix A). Adsorbate addition and removal due to fluxes (Appendix B), as well as diffusion, are calculated to the steady state by the closest point method (Chapter 4). Finally, an iteration can be made to evolve the surface subject to some limit using the level set method (Chapter 3). Then the cycle is repeated.

a surface, use the closest point method to transform the PDE into an easily solvable PDE on a Cartesian mesh, and integrate to a steady state. 3) Once the adsorbate kinetics are known, the surface can be evolved by etching or deposition using the level set method. The process then loops back to step 1, with a new surface, see Figure 5.1.

The implicit surface representation can be shared through all three models and provides a distinct advantage to this entire process. (The closest point method creates a slightly different embedding than the level set method (LSM), but this is not a significant penalty.) The implicit surface provides mathematically natural definitions for normals and curvatures, which are necessary for various physical computations. The evolution of implicit surfaces is topologically robust, allowing for the merging and separation of surfaces. The beam-sample interaction model benefits from the signed distance function representation of the implicit surface, in that as scattering is tracked, the algorithm always has a precise sense of distance from the surface. This is useful, for example, in truncating trajectories early, if one is only interested in surface flux, and in computing electron emission only within the electron escape depth of the material. Redeposition can be computed with

ray-tracing mechanics easily [148]. Implicit surfaces avoid "work-arounds" needed with evolving meshes, such as re-meshing [32], and de-looping [80].

Computationally, the MC step will be the most expensive. This can be ameliorated by techniques such as building cached tables, designing algorithms to be single instruction multiple data (SIMD), or running parallel code on graphics processing units (GPUs)[1]. The LSM step will be the most expensive in storage. This may be partially improved by a non-uniform grid which is refined in areas of higher detail, however this is complicated by the fact that changing the implicit surface representation impacts all three steps in the simulation.

5.2 Conclusions

The state today of simulation of electron or ion beam chemistry is lagging behind experimental work. Diffusion can be an important component to simulation. This thesis has shown that surface diffusion can drive surface evolution in several ways, such as growing the Ga droplet in Chapter 2, and deposition in Chapter 4. Electron and ion beam induced etching and deposition share common problems of surface evolution and adsorbate surface concentrations.

By moving away from mesh methods (also known in 1D as "string" methods) towards a new implicit surface representation, we could produce more powerful models. Furthermore, additional physics can be added such as surface tension / stress, curvature driven flow, etc. These implicit surface techniques simplify and empower the simulation of continuum adsorbate kinetics on a surface and the evolution of that surface by deposition or etching in three dimensions.

The implicit surface level set method has been utilized for many types of physics simulations since its invention, and have even been used for focused ion beam (FIB) deposition and etching. The closest point method, a much more recent development, is used in a few but growing number of research areas.

However, no work has been done to apply the implicit surface closest point method to adsorbate reaction-diffusion kinetics, nor to couple it with surface evolution via the level set method. In this

[1] Monte Carlo methods are easy to parallelize since every run is independent.

thesis it is shown that these two implicit surface methods can be made to work in concert, proving they can be used as a basis for EBIED and IBIED simulations.

During the course of this research, a considerable effort went into understanding the mathematics of and approaches to working with implicit surfaces. Further effort went into using this understanding to implement LSM and CPM algorithms and test them against published use cases. These verification steps were essential, and so, were documented in detail (LSM verification in Section 3.3, etch verification in Section 3.4.2, CPM verification in Section 4.4). The code development was a non-trivial exercise. At the time of writing, the level set method offers few libraries and the closest point method none.

With the addition of a beam-substrate Monte Carlo method, the proposed tool set enables exploration of phenomena and patterns with details at the scale of the interaction volume, over a micron range domain, in three dimensions.

Appendix A

Ion solid interactions modelling

This appendix implements a model for computing ion-solid interactions within a solid. While there are many software packages for simulating ion trajectories in solids, none are freely available, easily modifiable, and support generalized surfaces and materials. Only one package has very recently claimed to provide these features [203], but a central library is currently missing. The most widely used model, SRIM by Ziegler [204], uses the binary collision algorithm, and has undergone much comparison with experimental results. While it does not support a general surface[1], SRIM does document its physical assumptions, physics and algorithms. Thus it provides one template from which to construct a better surface-sensitive model, as well as a benchmark to test against.

The new code developed is called the Ion-Solid-Model (ISM), and is used to produce all plots in this chapter. Its novel feature is that multiple solids of any shape can be specified for modelling. All modelling results are my own.

This chapter covers some background and definitions (Section A.1) and the theory and models of ion solid interactions (Section A.2). The binary collision algorithm, its limitations and some decisions made in its implementation are reviewed in (Section A.3) along with results for general surfaces. Finally, this work will be placed back into the context of solving surface problems (Section A.4).

[1] only flat layers are supported by SRIM, no curved or "general" surfaces

A.1 Overview

The study of the physics of projectile ions into solids spans over 100 years. Excellent reviews can be found in [204–206]. Ion solid interactions are important for understanding high energy cosmic ray damage of satellites, nuclear reactor walls damaged by neutrons, and nano-scale sputtering and damage in focused ion beam (FIB) milling. This work will focus on the latter, which restricts the energies of interest to less than 50 keV.

Inside the solid, the ion slows continuously due to interactions of its electrons with the solid's electrons, known as *electronic stopping*. When passing close to a nucleus, the ion scatters off, and may knock the nucleus from its position in the crystal, creating an *interstitial vacancy pair*. On average the ion loses energy to these scattering events described as *nuclear stopping*. If all energy is lost the ion becomes *implanted* in the solid, or if it reaches the surface it may emerge as *sputter* and potentially *redeposit* elsewhere on the surface. An atom in the solid matrix must be given more than the *lattice binding energy* to move off-site and more than the *displacement energy* to start on its own trajectory. The collection of trajectories of the incoming ion and all knock-on atoms is known as a *collision-cascade*. An atom leaving the solid must have more than the *surface binding energy* in the direction normal to the surface, see Figure A.1.

When a solid is perfectly crystalline, certain angles and positions for the incoming ion will allow it to *channel* deeply into the material. As damage builds up in the solid, this lattice structure is lost. In general, with typical FIB doses, this happens so quickly that it is reasonable to consider the material as initially *amorphous*. The following discussion is limited to the case of an amorphous substrate.

Signals that emerge from the solid due to these processes include neutral and ionized sputtered atoms, which carry information about the initial composition of the solid, as well as secondary electrons (SE) excited within the surface escape depth. These particles can stimulate further processes with the surface adsorbates, see Chapter 4.

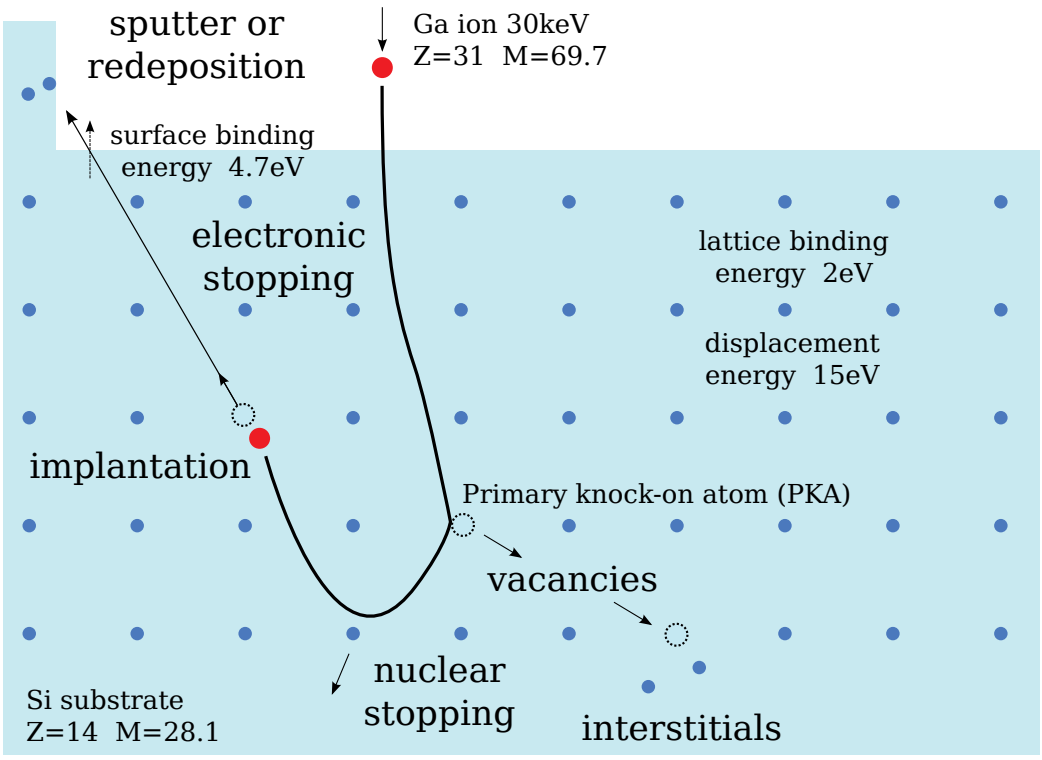

FIGURE A.1: Ion solid interactions illustrated by a Ga^+ ion (red) entering a silicon crystal with nuclei (dark blue) and electron field (light blue).

A.2 Ion solid collision theory

Ion-solid interactions are complex, especially at high energy, as Ziegler notes [204], "*Once the ion penetrates a solid, it is quickly stripped of some of its electrons, and its charge state becomes a function of the target. The target feels the ion coming, and its electrons polarize around the moving ion. The charge state of the ion is modified by the polarized target, which then further affects the target*". This many-body electrodynamic (and even quantum) problem is computationally intractable. Progress can only be made by making reasonable simplifying assumptions.

A.2.1 Total stopping

As an ion moves through a solid it loses kinetic energy as a function of its instantaneous speed. This probabilistic energy loss, characterized as a *stopping force* is often called in the literature the *total stopping cross-section* [204]. The total stopping cross-section exhibits two peaks, a peak

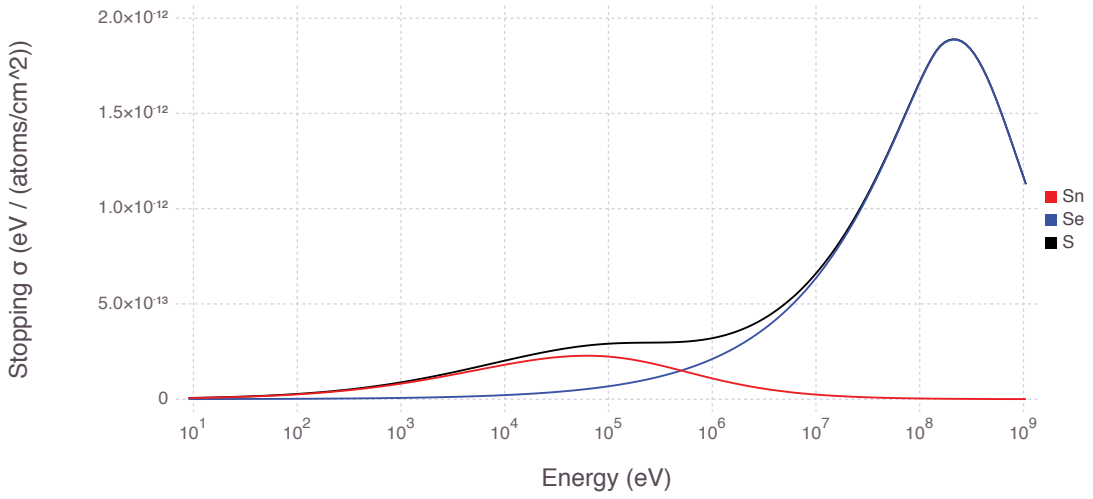

FIGURE A.2: Plots of the nuclear $S_n(E)$, electronic $S_e(E)$ and total stopping cross section $S(E)$ for gallium in silicon.

at high energy due largely to electronic interactions and a peak at lower energy due to nuclear interactions. Bohr was the first to observe that electronic and nuclear stopping could be treated separately [207], by modelling the solid as a continuous electric field with point-like nuclei. Bohr concluded that the energy loss of the ion moving through a solid could be reasonably divided into two components corresponding to the nuclear stopping force, $S_n(E)$, and the electronic stopping force, $S_e(E)$, see Figure A.2 for an example of total, nuclear and electronic stopping. Semi-empirical formulas have been developed for both $S_e(E)$ and $S_n(E)$, which are described next.

A.2.2 Electronic stopping

Electronic stopping arises from inelastic electron-electron interactions between the solid's electrons and the moving ion's electrons. It acts like a drag on the ion, slowing the ion without changing its direction (unlike the nuclear stopping, Subsection A.2.3). The force can strip off additional electrons so that the *effective charge* will vary from neutral to completely ionized depending on the speed; as Möller states [208], "*the actual charge state of a fast ion in matter is continuously fluctuating and determined by a balance between electron loss and electron attachment*". At low energy, electronic stopping is approximately linear with energy. However, with increasing energy (much higher than 50 keV) a peak occurs above which the ion, completely stripped of electrons,

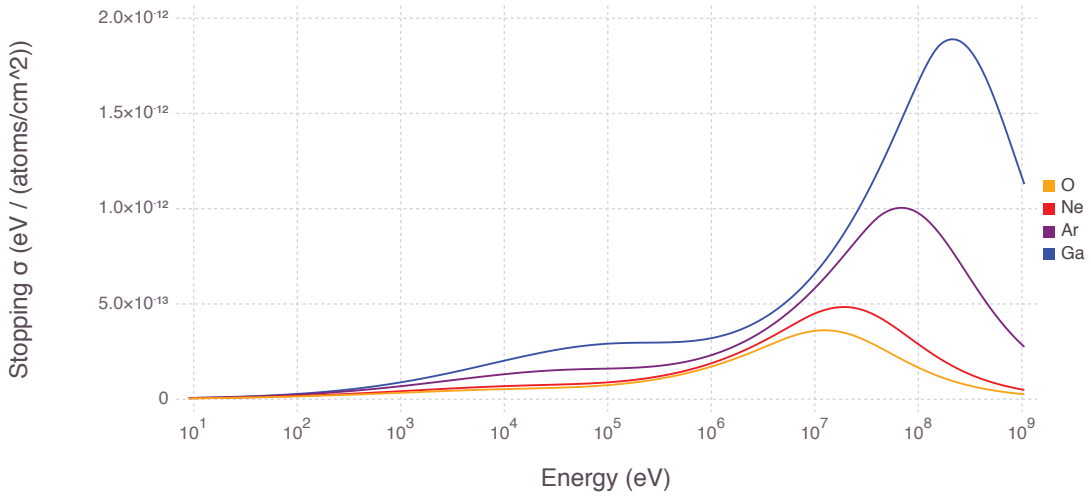

FIGURE A.3: Plots illustrating the total stopping cross section of several ion species in Si. If the x-axis were normalized by ion velocity $v_F Z_1^{2/3}$ the highest (electronic stopping) peaks would be aligned.

has a falling S_e. The exact position of this peak is dependant on the ion speed relative to the Fermi velocity of the solid, $v_F \approx v_B Z_1^{2/3}$ (where v_B is the Bohr electron velocity), see Figure A.3. Loosely interpreted, the ion experiences a peak drag when its speed is comparable to that of the solid's orbiting electrons.

There are two differing models for computing the electronic stopping, applied on either side of this peak (low and high energies). The electronic interactions can be evaluated in the low energy regime by the Lindhard and Scharff model [209], and the high energy regime by the Bethe model. The Lindhard and Scharff (non-local) stopping is

$$S_e = \frac{8\pi e^2 a_0}{4\pi\varepsilon_0} \frac{Z_1^{7/6} Z_2}{\left(Z_1^{2/3} + Z_2^{2/3}\right)^{3/2}} \frac{v}{v_0} \qquad \text{(LS low } v\text{)} \tag{A.1}$$

where a_0 is the Bohr radius, v_0 is the Bohr velocity, and v is the ions velocity, Z_1 and Z_2 are the atomic numbers of the ion and atom. The Bethe stopping is

$$S_e = \frac{4\pi e^4}{(4\pi\varepsilon_0)^2} \frac{Z_1^2 Z_2}{m_e v^2} \log\left(\frac{2m_e v^2}{I}\right) \qquad \text{(Bethe high } v\text{)} \tag{A.2}$$

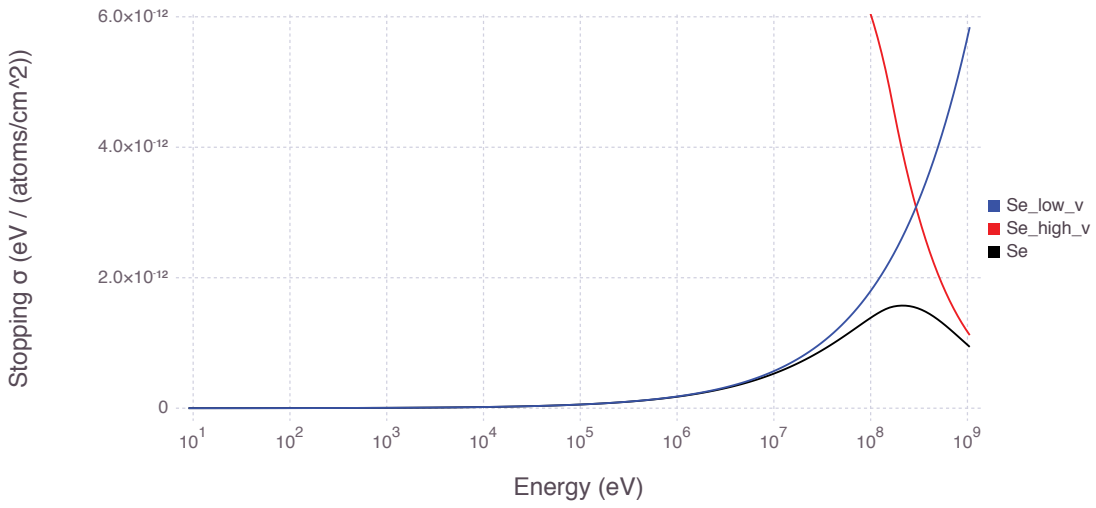

FIGURE A.4: Plots of the electronic stopping cross section models for gallium in silicon at low and high energy, as well as their reciprocal sum, taken to be the electronic stopping.

where m_e is the electron mass and I is the mean ionization potential and is approximated by $I = 10Z_2$ (eV). The value of v for which the switch is applied is $v = v_0 Z_1^{2/3}$.

The two models are combined to give an approximation in the intermediate regime, providing a smooth extension for the high-energy model at lower energies

$$\frac{1}{S_e} = \frac{1}{S_e(\text{LS low } v)} + \frac{1}{S_e(\text{Bethe high } v)} \tag{A.3}$$

which is illustrated in Figure A.4.

While scientific interest in the stopping force ranges from 0 to 10^8 keV, the nanotechnology world of FIB is only concerned with a fraction of this range, up to 50 keV. For the purposes of the binary collision algorithm at lower energies, S_e can be modelled as a velocity proportional drag on the ion (called the *continuous slowing down approximation*) which has been expressed empirically by Oen [210]. This form of S_e accounts for and becomes dependant on the impact parameter p of the collision (see Subsection A.2.4.)

$$\Delta E = \frac{0.045k\sqrt{E}}{\pi a_0^2} \exp\left(\frac{-0.3p}{a_0}\right) \tag{A.4}$$

where k is a function of Z_1, Z_2 and M_1 and the and ion energy E is given in (eV).

A.2.3 Nuclear stopping

The nuclear stopping cross section can be semi-empirically derived from a screened Coulomb potential. Ziegler [204] gives the relationship as

$$S_n(E) = \frac{8.462 \times 10^{-15} Z_1 Z_2 M_1 S_\varepsilon(\varepsilon)}{(M_1 + M_2)(Z_1^{0.23} + Z_2^{0.23})} \tag{A.5}$$

where the units of S_n are (eV/(atom/cm^2)) and where the *reduced energy* ε of the system is given by

$$\varepsilon(E) = \frac{32.53 M_2 E}{Z_1 Z_2 (M_1 + M_2)(Z_1^{0.23} + Z_2^{0.23})} \tag{A.6}$$

where for $\varepsilon \leq 30$

$$S_\varepsilon(\varepsilon) = \frac{\ln(1 + 1.1383\varepsilon)}{2(\varepsilon + 0.01321\varepsilon^{0.21226} + 0.19593\varepsilon^{0.5})} \tag{A.7}$$

and for $\varepsilon \geq 30$

$$S_\varepsilon(\varepsilon) = \frac{\ln(\varepsilon)}{2\varepsilon} \tag{A.8}$$

Nuclear stopping dominates over electronic stopping at the low energies at which FIB is performed. The relative magnitudes at all energies can be seen in Figure A.2.

The nuclear stopping of (A.5) does not yield details about the trajectory or sputter from ion-solid interactions. A Monte Carlo evaluation of a series of classical scattering events is instead used to build up trajectories and cascades in the solid. Next we review how one scattering event can be solved, a core piece of the binary collision algorithm.

A.2.4 Classical scattering event

An atomic scattering event can be solved analytically. Momentum and energy are both conserved. Given the masses of the two particles M_1 and M_2, their interaction potential $V(r)$, the impact parameter p (the distance of the initial asymptotic trajectory of M_1 to M_2) and the energy E of the incoming particle (with M_2 initially at rest), the resulting energy transfer and scattering angles can be derived. Without loss of generality, the event can be reduced to two dimensions and aligned with the incoming particle velocity. Furthermore, it is useful to change from lab frame to centre of

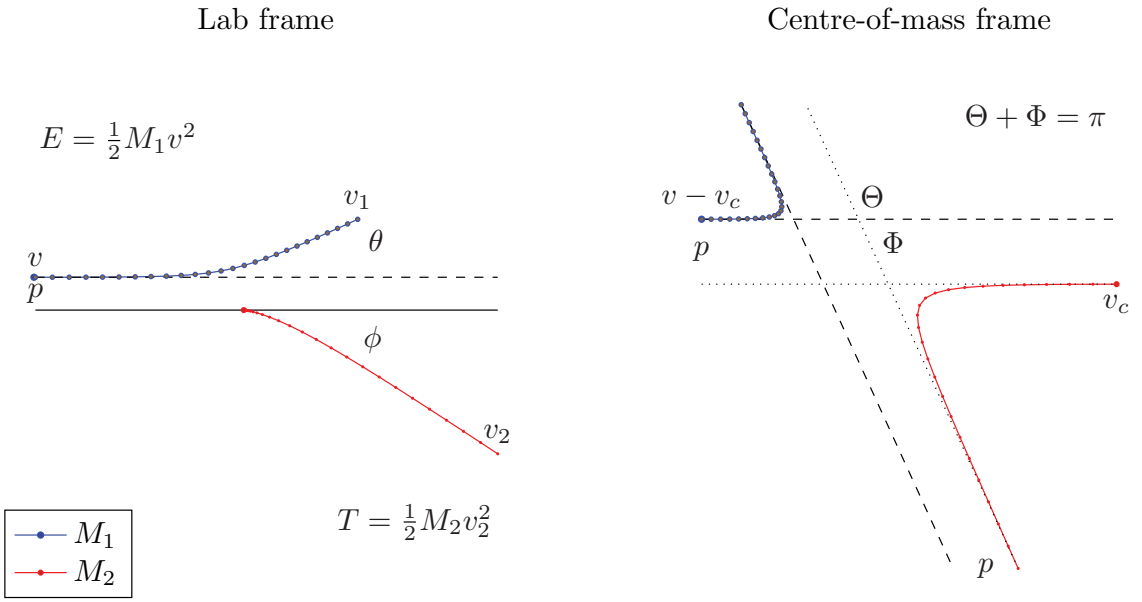

FIGURE A.5: A gallium ion at 30 keV scattering off of a silicon atom at rest. Here $M_1 = 69.723$ a.m.u., $M_2 = 28.085$ a.m.u., and the impact parameter $p = 7.75$ pm. The velocity Verlet algorithm using the appropriate universal Ziegler, Biersack, and Littmark (ZBL) potential was integrated to yield the trajectory. Timesteps taken are indicated by dots on the trajectory. **Left** shows the scattering event in the lab frame which is completely determined by the (input) energy E, impact parameter p, and masses M_1, M_2. The resulting (output) transferred kinetic energy $T = 17.7$ keV (gained by M_2, lost by M_1), and the scattering angles $\theta = 24.38°, \phi$. The distance at the apsis (distance of closest approach) is 20.0 pm. **Right** shows the same scattering event in the centre-of-mass reference frame. Note that in the CM frame there is only one scattering angle, which defines both particles' opposite exit directions. Right and left are on different scales.

mass (CM) frame by adding the system's centre of mass velocity, $-v_C$, to both particles. Under this transformation, the CM is at rest, and symmetry of the trajectories is induced, see Figure A.5.

We will now review the derivation[2] of the kinetic energy transferred, $T(\Theta)$, as a function of scattering angle Θ, and then the scattering angle itself, $\Theta(p, E, V(r))$, as a function of impact parameter p, initial energy, E, and potential of the system V.

A.2.4.1 Derivation of kinetic energy as a function of scattering angle

Applying conservation of energy and momentum for an elastic collision yields the relations

$$E = \frac{M_1v^2}{2} = \frac{M_1v_1^2}{2} + \frac{M_2v_2^2}{2} \tag{A.9}$$

[2]This most closely follows Ziegler [204].

$$M_1 v = M_1 v_1 \cos(\theta) + M_2 v_2 \cos(\phi) \tag{A.10}$$

$$0 = M_1 v_1 \sin(\theta) + M_2 v_2 \sin(\phi) \tag{A.11}$$

Define new vector coordinates X and x for centre of mass and inter-particle distance

$$X = \frac{M_1 x_1 + M_2 x_2}{M_1 + M_2} \qquad x = x_1 - x_2 \tag{A.12}$$

and the transformation between lab to CM frame becomes

$$x_1 = X + \frac{M_2}{M_1 + M_2} x \qquad x_2 = X - \frac{M_1}{M_1 + M_2} x \tag{A.13}$$

Define the velocity of the centre of mass as

$$v_C = \frac{v M_C}{M_2} \tag{A.14}$$

where

$$M_C = \frac{M_1 M_2}{M_1 + M_2} \tag{A.15}$$

By subtracting the centre of mass velocity from both particles' initial velocities, we transform the system from the lab frame to the CM frame. In the CM frame the total momentum is always zero. The total energy of the system in the CM frame is given by

$$E_C = \frac{M_1 (v - v_C)^2}{2} + \frac{M_2 v_C^2}{2} = \frac{M_C v^2}{2} \tag{A.16}$$

The relationship of the angles in lab and CM frames is geometric, see Figure A.6. The second particle M_2 has zero velocity initially in the lab frame, but $-v_C$ in the CM frame and ends with velocity v_C. By equal angles between parallel lines, and the isosceles triangle property (two equal sides yield two equal angles) we have

$$\phi = \frac{\Phi}{2} = \frac{\pi - \Theta}{2} \tag{A.17}$$

and applying the law of cosines

$$v_2^2 = v_C^2 + v_C^2 - 2 v_C^2 \cos(\pi - \Phi) = 2 v_C^2 (1 - \cos \Theta) \tag{A.18}$$

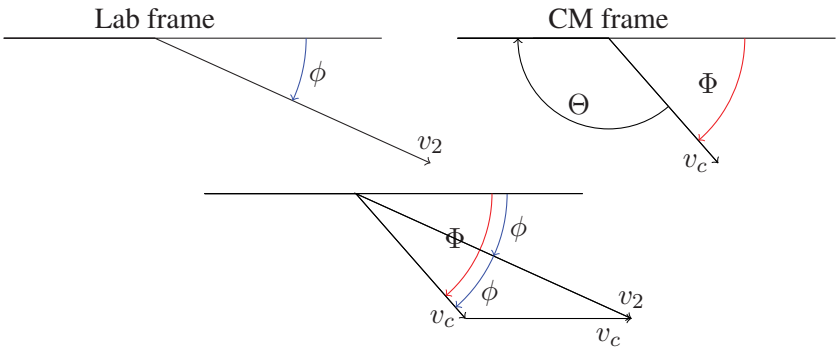

FIGURE A.6: Geometric relationship of the angles between the reference frames for the M_2 velocities, illustrating $\Phi = 2\phi$ and $\Phi = \pi - \Theta$ (image derived from Ziegler [204] pg. 2-5.)

yields

$$v_2 = 2v\frac{M_C}{M_2}\cos\phi \tag{A.19}$$

and

$$\tan\theta = \frac{(v - v_C)\sin\Theta}{v_C + (v - v_C)\cos\Theta} = \frac{M_2\sin\Theta}{M_1 + M_2\cos\Theta} \tag{A.20}$$

We can now derive the energy transferred to the second particle in the lab frame from

$$T = \frac{M_2 v_2^2}{2} \tag{A.21}$$

Using the angle relationships above, algebraic manipulation yields

$$\boxed{T(\Theta) = \frac{4EM_1M_2}{(M_1 + M_2)^2}\sin^2\left(\frac{\Theta}{2}\right) = E\gamma\sin^2\left(\frac{\Theta}{2}\right)} \tag{A.22}$$

where γ is the *mass mismatch* coefficient [205].

$$\boxed{\gamma = \frac{4M_1M_2}{(M_1 + M_2)^2}} \tag{A.23}$$

Observe that when $M_1 = M_2$, $\gamma = 1$, otherwise, $\gamma < 1$. The mass-mismatch coefficient by itself can predict characteristics of the ion's trajectory, see Subsection A.2.4.4.

A.2.4.2 Derivation of scattering integral

The total energy in the CM frame is given in polar coordinates by

$$E_C = \frac{1}{2} M_C \left(\dot{r}^2 + r^2 \dot{\Theta}^2 \right) + V(r) \tag{A.24}$$

Remembering that at $t = 0$ $E_C = \frac{1}{2} M_C v_0^2$ we can eliminate M_C

$$E_C = \frac{E_C}{v^2} \left(\dot{r}^2 + r^2 \dot{\Theta}^2 \right) + V(r) \tag{A.25}$$

Now the angular momentum is constant as

$$J_C = M_C r^2 \dot{\Theta} \tag{A.26}$$

and at $t = 0$, in terms of the impact parameter p is

$$J_C = M_C v p \tag{A.27}$$

Setting these equal yields the relation

$$\dot{\Theta} = \frac{vp}{r^2} \tag{A.28}$$

which can be substituted into (A.25), yielding

$$E_C = \frac{E_C}{v^2} \left(\dot{r}^2 + r^2 \left(\frac{vp}{r^2} \right)^2 \right) + V(r) \tag{A.29}$$

This can be rearranged to solve for dr/dt as

$$\dot{r} = v \sqrt{1 - \frac{V(r)}{E_C} - \left(\frac{p}{r} \right)^2} \tag{A.30}$$

Note that the trajectory reaches its *apsis*, where r is minimum (r_{min}) at the turning point $\dot{r} = 0$. By evaluating

$$\frac{\dot{\Theta}}{\dot{r}} = \frac{d\Theta}{dr} = \frac{p}{r^2 \sqrt{1 - \frac{V(r)}{E_C} - \left(\frac{p}{r} \right)^2}} \tag{A.31}$$

and integrating (noting $\Theta = \pi$ initially) we have the scattering angle

$$\Theta = \pi - \int_{-\infty}^{\infty} \frac{p}{r^2\sqrt{1 - \frac{V(r)}{E_C} - \left(\frac{p}{r}\right)^2}} dr \tag{A.32}$$

which can be simplified by noting the symmetry of the trajectories around the apsis (r_{min})

$$\boxed{\Theta = \pi - 2p \int_{r_{min}}^{\infty} \frac{1}{r^2\sqrt{1 - \frac{V(r)}{E_C} - \left(\frac{p}{r}\right)^2}} dr} \tag{A.33}$$

where the distance of closest approach, r_{min}, is given by r such that

$$1 - \frac{V(r)}{E_C} - \frac{p^2}{r^2} = 0 \tag{A.34}$$

All parameters in the integral above have been described except for the potential $V(r)$, which is discussed next.

A.2.4.3 Screened coulomb potential

As the ion approaches the target atom, there is a weak repulsive coulomb force between the two nuclei, which is modelled as a columbic potential reduced by a screening function Φ

$$V(r) = \Phi\left(\frac{Z_1 Z_2 e^2}{r}\right) \tag{A.35}$$

Many inter-atomic screening functions have been proposed to reduce the coulomb potential, see Figure A.7. The "universal" function Φ_U empirically specified by Ziegler, Biersack, and Littmark (ZBL) [211], yields a potential that agrees with experimental results within 5%.

A.2.4.4 Implications of mass mismatch

One consequence of the classical scattering is that the energy transfer and scattering angles are limited by γ given in (A.23). This mass mismatch limits [205] the amount of energy transfer possible when $M_1 > M_2$ and consequently the final scattering angle of M_1. When the mass

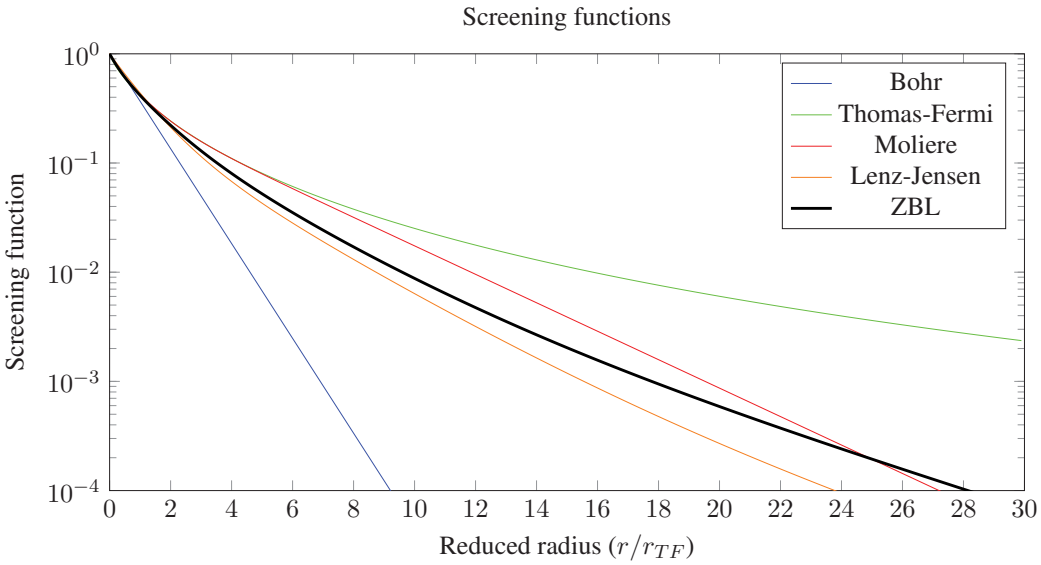

FIGURE A.7: Various screened potentials proposed in the literature, expressed on a dimensionless plot. The Thomas-Fermi screening length r_{TF}, is a function of atomic number and defines a radial spread of electronic charge about the nucleus.

mismatch limits the angles possible, the cumulative effect over multiple scattering events results in different trajectories of the implanted ion, see Figure A.8.

A.3 Binary collision algorithm

In general, nuclear interactions are evaluated as classical elastic scattering events, using a screened Coulomb potential, see Ziegler [204]. The computation of the nuclear stopping essentially becomes a atom-atom screened-Coulomb interaction, which alters the trajectory of the ion's path through the solid. Only the ion and target atom are considered, making this a *binary collision*, the fundamental assumption in the binary collision algorithm (BCA).

The assumption of a binary collision breaks down in certain energy regimes. Eckstein [212] notes that the highest lower limit for BCA accuracy comes from the length needed for asymptotic trajectories versus the lattice constant of the solid, and this is in many cases about 20 eV. There are other physical arguments given by Robinson [213] limiting BCA at lower energies: many body effects creep in at 10 eV which corresponds to the velocity of sound in metals; quantum mechanically at 1 eV, the deBroglie wavelength of a proton rivals the lattice dimension as well. Smith [214] notes

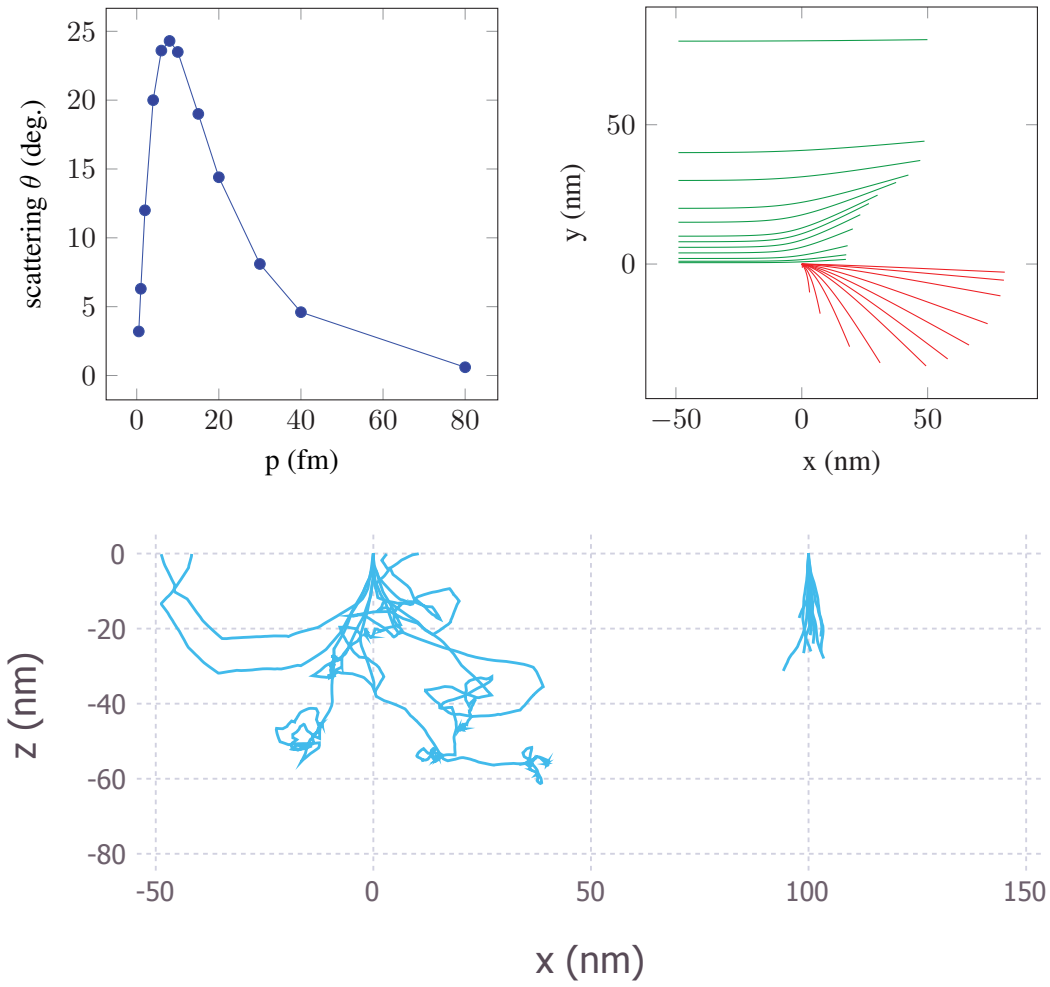

FIGURE A.8: Implications of mass mismatch, (A.23). **Top** illustrates scattering for different impact parameters. Example shows Ga (M_1=69.7) atom onto a Si atom (M_2=28.0) at 30 keV for a range of impact parameters. Left shows the resulting scattering angle as a function of impact parameter, and right shows the family of trajectories taken by the ion (green) and the target silicon atom (red). **Bottom** illustrates the impact on implantation trajectories entering a solid ($z < 0$) for carbon (M=12.01) and tungsten (M=183.84) at 30 keV. Left is carbon ions entering at (0,0) into solid tungsten, and right is tungsten ions entering at (100,0) into solid carbon. In the former (light ion into heavy solid) several of the trajectories return to the surface indicating ion re-entry into the vacuum, in the latter (heavy ion into light solid) very little deviation from the original trajectory is experienced.

that typically the deBroglie wavelength is small compared to thermal vibration in atoms so that quantum mechanics only plays a role in discussing the interatomic function.

The binary collision algorithm also assumes a series of single scattering events, no "change" to the solid during the interactions, and enough relaxation time in between events such that the solid has time to relax. The last condition is also known as the *linear cascade regime*.

The procedure for computing the ion path through the solid begins with a given initial position, velocity and energy. The distance, or *path length*, to the next scattering event is determined from the local atomic number and material density. An impact parameter p is selected from a random distribution related to the path length. The scattering integral is computed and the resulting velocity of the ion and target is determined. The ion's kinetic energy is reduced by the nuclear collision and by an energy given from the empirical electronic stopping. This is repeated until the ion's energy is small and the ion is implanted, or it leaves the solid as sputter. The entire *trajectory* is recorded with bookkeeping done to note all energy lost in the solid and damage created. Targets which are given enough energy to start their own trajectory are also all evaluated if desired. All data from the trajectories is collated in a *cascade*. This algorithm for computing cascades is expressed in pseudo-code in Algorithm 1. There are subtleties that different programs have implemented, for full details, see [204, 206, 213, 214].

The key in this implementation which allows for general surfaces is that the BCA algorithm accepts a function which decides where and if a moving atom has escaped the surface. By passing in the function *isOutsideVolume()* the BCA can refer to any surface at runtime. The surface can even be dynamically changing with every call. This change is required when interfacing with a surface evolution technique, such as the level set method, see Chapter 3.

Additionally, dynamic compositional changes can be added (as is done in TRIDYN) if the target is specified by a function.

A.3.1 Biersack's "scattering triangle"

The scattering integral, (A.2.4.2), can be evaluated computationally in several ways, ordered below from most CPU intensive to least:

Data: ion, E, target, **x**, **v**, isOutsideVolume(), gen, t, doRecoils
Result: cascade data structure
E_{min} = minimum surface binding energy of target;
while $E > E_{min}$ **do**
    determine next nuclei for scattering event;
    $p = \sqrt{\frac{-\log(R_N)}{\pi N \lambda}}$;
    Θ, T, r_0 = computeScatteringIntegral();
    advance **x**, **v**;
    if $T >$*nuclei displacement energy AND doRecoils* **then**
        recursive call for atom with T - lattice binding energy;
        append subcascade to cascade
    end
    record step in trajectory in cascade;
    if *isOutsideVolume()* **then**
        return cascade
    end
end

Algorithm 1: Recursive algorithm to compute a series of binary collisions down to a minimum energy, returning the resulting cascade of events from ion passing through an amorphous solid.

- numerical evolution of trajectory (velocity Verlet algorithm)
- numerical quadrature on the scattering integral
- Biersack's fitting formula "magic formula"

In 1980, Biersack published [215] a method which can be used to approximate the classical scattering integral. Biersack claimed that this algorithm works to 1% but never published the proof[3]. The software package SRIM and MARLOWE claim to use this algorithm, though experimentation seems to indicate that SRIM does not apply this approximation for non-high energy ions. The algorithm (also known as the "magic algorithm") uses the concept of a *scattering triangle* constructed from the tangential curves at the apsis and its orientation to the asymptotic approach of the two masses in the CM reference frame, see Figure A.9.

Geometrically, the triangle relates the scattering angle to the characteristic distances in the binary collision.

$$\cos\left(\frac{\Theta}{2}\right) = \frac{\rho + p + \delta}{\rho + r_0} \tag{A.36}$$

[3] In Biersack's paper [215] reference 15 is *"J.P. Biersack, L.G. Haggmark and M.I. Baskes, to be published"*, however, online searches do not show any publication.

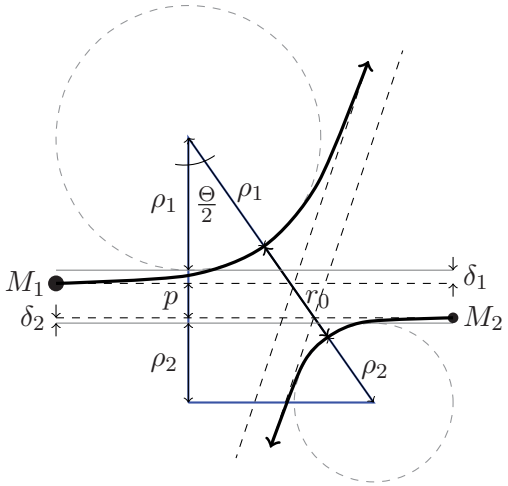

FIGURE A.9: Definition of Biersack's scattering triangle (blue) in terms of the trajectories of the two masses interacting in a screened coulomb potential in the CM reference frame. Here M_1 and M_2 are the masses of the ion and atom respectively, p is the impact parameter, r_0 is the distance of closest approach, ρ_1 and ρ_2 are radii of curvature of trajectory of closest approach, and δ_1 and δ_2 are "correction terms". Figure derived from Smith [214] pg. 20

with $\rho = \rho_1 + \rho_2$ and $\delta = \delta_1 + \delta_2$. Given the impact parameter p, the apsis r_0 is found from (A.34) (by, for example, Newton's method). The radii of curvature ρ_1 and ρ_2 can be found by computing the centrifugal force. The remaining term δ is typically much smaller than the other distances. A fit with five degrees of freedom is then made for δ against numerical integration of the scattering integral.

This approach is computationally faster (on the order of x50 in cases tried), but the ISM implementation shows that it underestimates the scattering angle. For example, in a binary collision for gallium ions at 30 keV on silicon, see Figure A.10. Others have also noted differences [216]. For this reason, the scattering triangle approach was avoided. Similar speed increases in the code can be achieved by creating lookup tables of the precisely computed scattering angles.

A.3.2 Implementation

The implementation was performed initially in python [217] and plotted by Matplotlib [218]. However, it was quickly ported to the Julia programming language [219], see Appendix C, to more easily take advantage of multi-core environments and 2D/3D plotting with the Gadfly package [220] and ParaView [179], see Figure A.11 for an example of ParaView output. The program

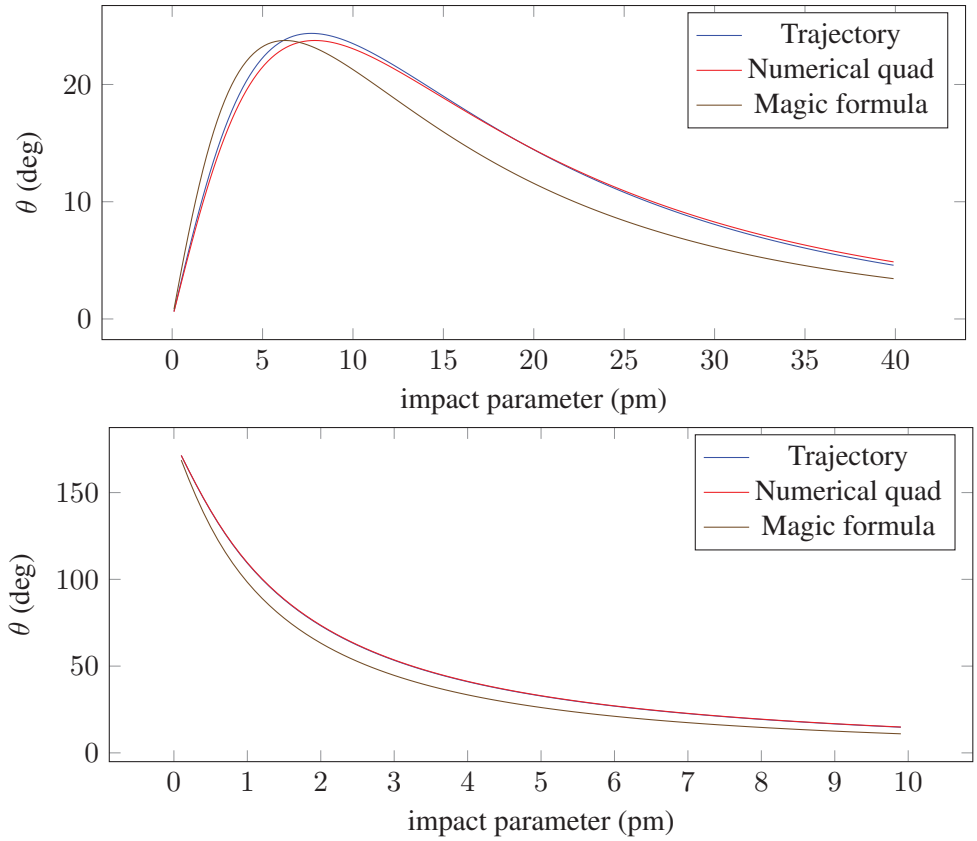

FIGURE A.10: Biersack's approach ("magic formula") poorly estimates the scattering angles of gallium (**top**) and carbon (**bottom**) ions at 30 keV on Si over a wide range of impact parameters. Plotted here are the three techniques listed in Subsection A.3.1.

features the ability to handle any type of amorphous material volume (with mixes of different densities in 3D) and any surface definition (spheres, cylinders, irregular, etc.). These features are not provided by the most common package available, SRIM [211].

A.3.3 Validation and Results

The ISM code was first compared against the results from SRIM in the case of a flat plane. The results are not compared with experiment, as SRIM itself has deficiencies in comparing with experiment [221, 222]. Thereafter, the ISM code was run to generate results in non-flat conditions, which SRIM cannot reproduce.

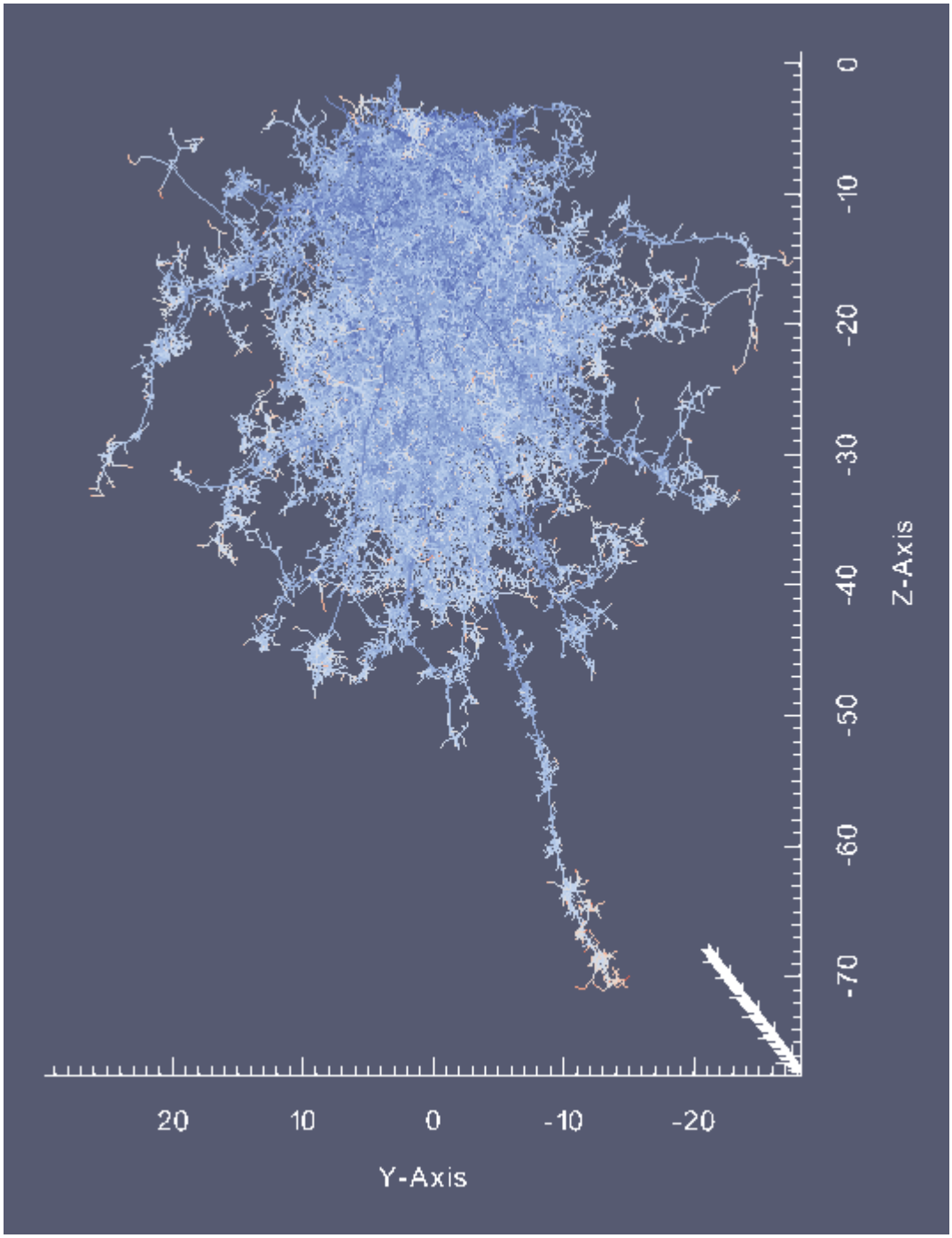

FIGURE A.11: Example of snapshot from 3D scientific visualization software, ParaView, displaying several collision cascades coloured by time in femtoseconds from early (blue) to late (red) in the cascade.

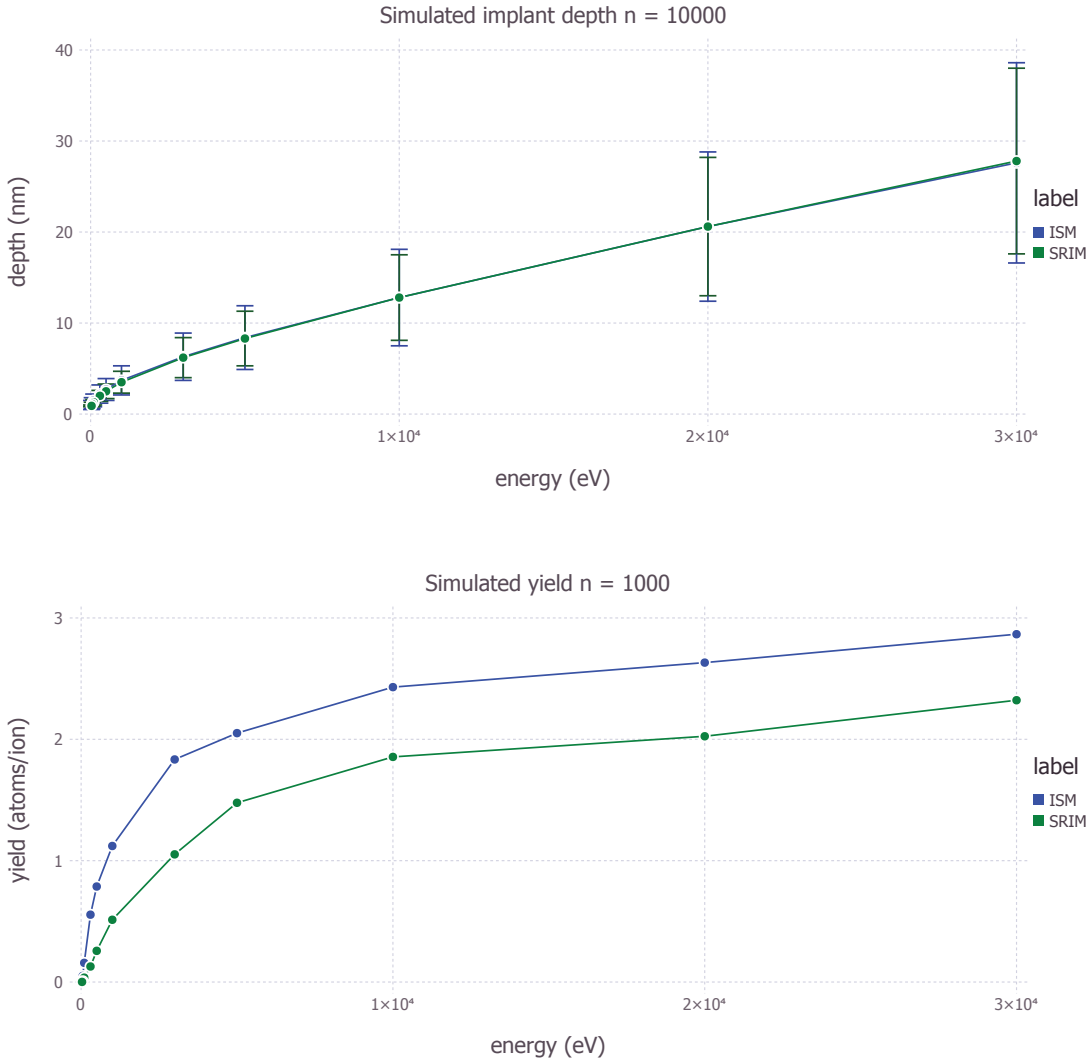

FIGURE A.12: ISM results show excellent agreement with SRIM for implantation (**top**) and the correct trend (but not absolute agreement) for sputter yield (**bottom**). The latter can be brought into agreement with SRIM for some versions of electronic stopping. The error bars indicate the standard deviation of the scatter in the z implantation depth.

A.3.3.1 Flat surfaces

The results for implantation agree closely. Results for sputter yield do not match exactly, due to inadequate documentation detail on how SRIM handles the surface but can be tuned to agreement with various reasonable choices of electronic stopping, see Figure A.12. These results allow for running simulations for implantation, or for studying sputter yield ratios. This code can also give

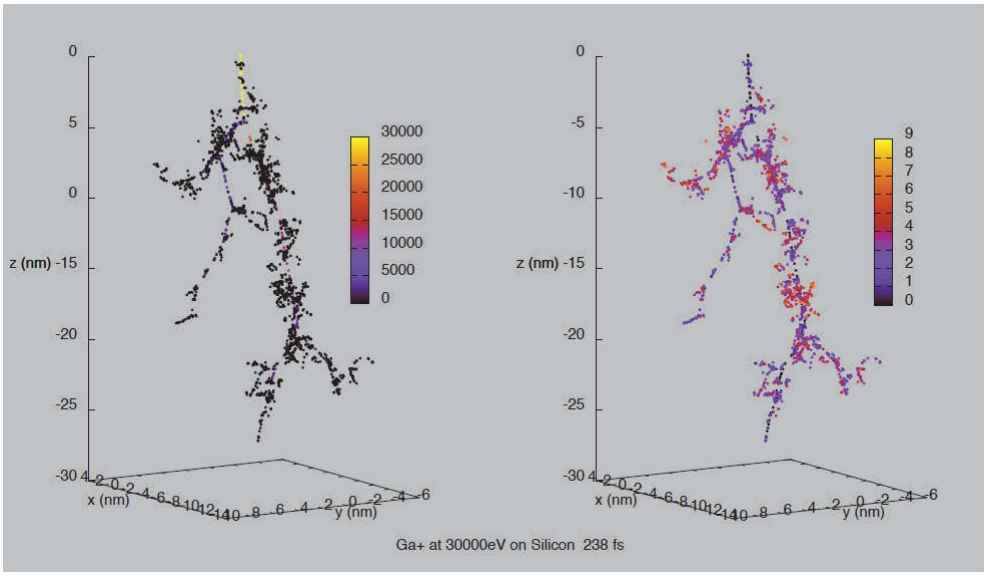

FIGURE A.13: Example results from ISM code showing multiple cascades arising from 30 keV Ga ions entering silicon at the origin. **Left** coloured by energy, **Right** coloured by generation of knock-on.

detailed pictures of the intermediate calculations, see Figure A.13.

A.3.3.2 Curved surfaces

Sputter yield enhancement for Ga^+ at 30 keV into silicon was studied on half-cylinder and half-sphere solids of various radii, see Figures A.14 and A.15. This type of simulation is not possible with SRIM because the surface curves out of the plane, however other work is available [223, 224]. Here we can observe that for half-cylinders the radius of curvature does not affect the sputter yield as the angle of incidence is tilted along the axis of the cylinder. When the curvature rivals the interaction volume there is more sputter yield at all angles. For hemispheres, the mean (shown) and standard deviation (not shown) peak at different angles, the sputter peak shifts to lower angles as the hemisphere shrinks and that sputter is enhanced by 30% for even some larger hemispheres. Finally, the largest hemisphere is most similar to the half-space (an infinite flat plane). These results indicate successfully running code and trends, but deviate grossly from experimental data see [225].

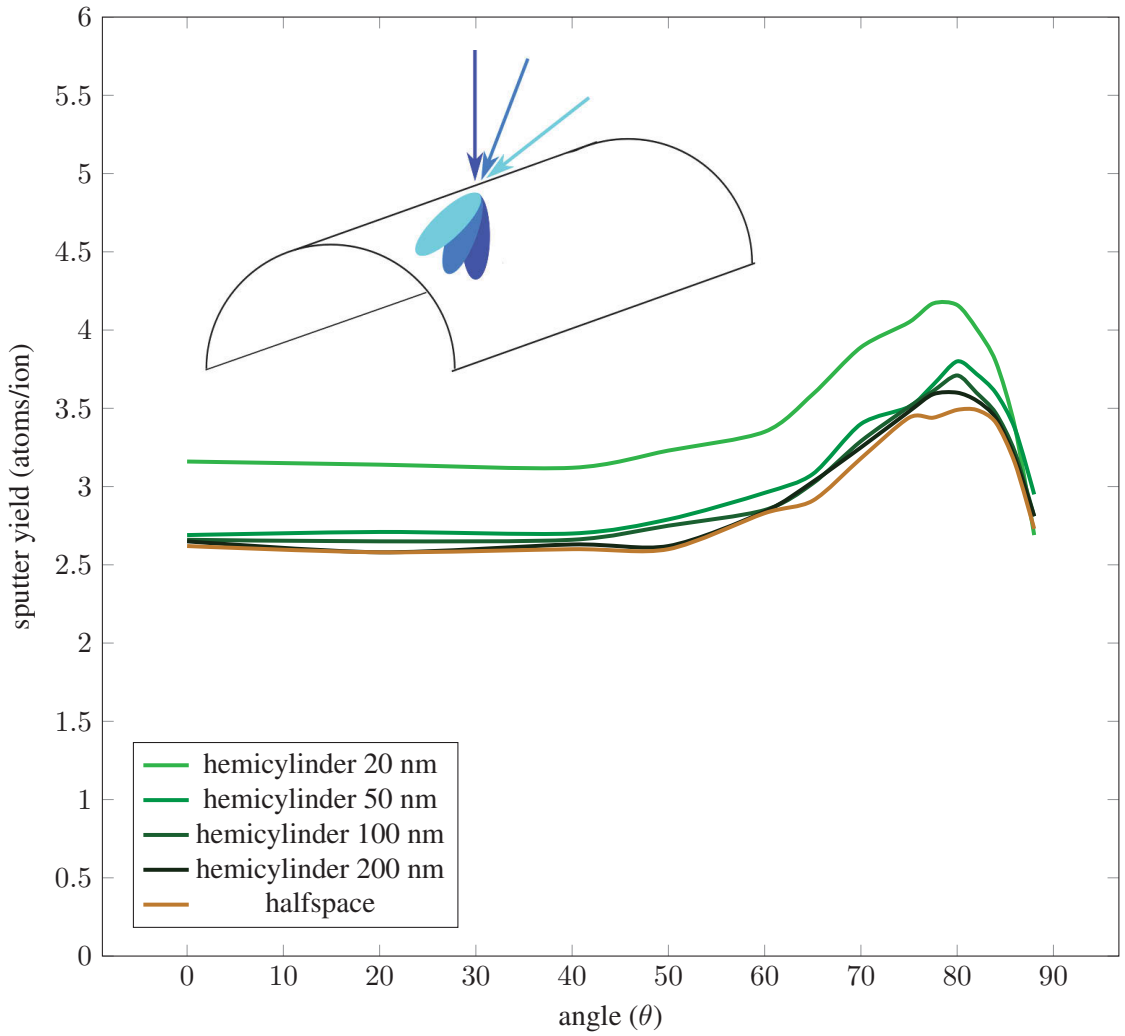

FIGURE A.14: ISM results of sputter yields from hemicylinders at different radii of curvature. **Inset** Illustration of simulation of interaction volumes on a half-cylinder at various angles.

A.4 Conclusions

A new implementation of a BCA has been written which allows for an arbitrary surface definition, allowing for simulation of curved and otherwise generalized surfaces. The code, named ISM, has been verified for flat surfaces against SRIM. Simulations have then been run for curved surfaces, and produced reasonable results.

This development effort was absolutely necessary in the face of tackling surfaces which defy conventional (flat) geometries, or surfaces which are evolving in time. The level set method for representing the surface (see Chapter 3), provides a natural definition which can be used for the

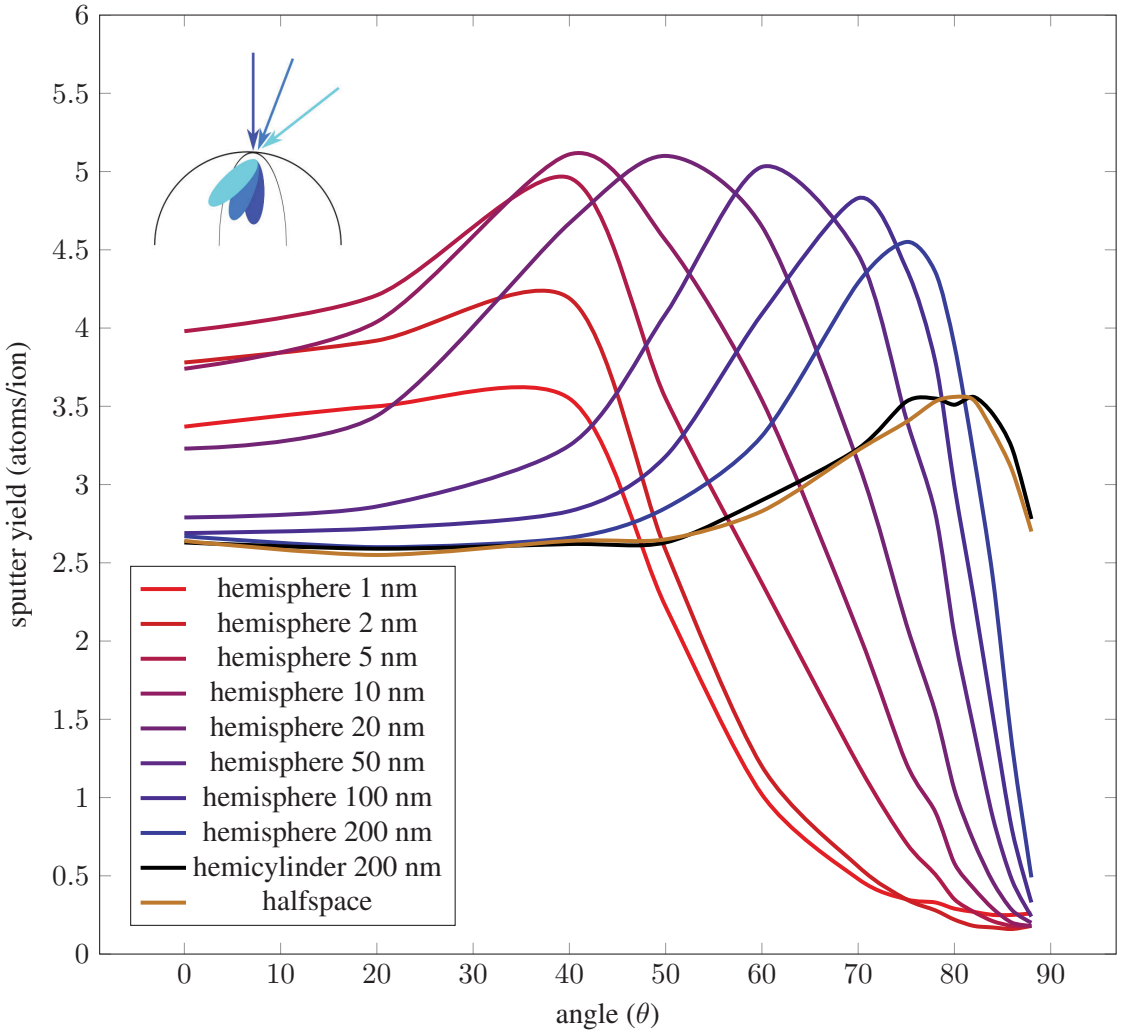

FIGURE A.15: ISM results of sputter yields from hemispheres at different radii of curvature. **Inset** Illustration of simulation of interaction volumes on a half-sphere at various angles.

function *isOutsideVolume()*. The level set method and the Monte Carlo method can be combined to produce a simulation of dynamically evolving surfaces in 3D.

An additional benefit is that the code base also can be extended in many directions, e.g., tracking volumetric changes (as does TRIDYN), as well as adding channelling or crystalline effects. The addition of ion generated secondary electrons (iSE) would be of value, as has been accomplished in IONiSE [226, 227] and EnvizION [228].

Appendix B

Framework for EBIED / IBIED adsorbate continuum equations

This appendix takes the best of electron beam induced etching and deposition (EBIED) adsorbate continuum models, generalizes and frames it for reuse in wider situations. This is accomplished by defining a mathematical framework for modelling EBIED adsorbate kinetics which:

1. lists various "elemental" surface processes which affect adsorbate concentration,
2. gathers these different physical processes into three main groups, and,
3. organizes them into a square system of partial differential equations.

By mathematically grounding the EBIED adsorbates kinetics with this approach, the ion beam induced etching and deposition (IBIED) situation is recognized to be largely the same with only the addition of sputtering and redeposition. This framework then forms a full "template" to guide the modelling of any EBIED / IBIED system.

In EBIED work, a number of phenomena have been identified and studied in isolation, either not modelled at all or focused to model one effect and ignoring others, leaving it unrealistic, and consequently unphysical. There has been no unified framework. The situation is even worse in IBIED, where only a few effects have even been modelled (sputtering, redeposition), despite the fact that all the same chemical mechanisms of precursor and substrate exist. IBIED is essentially

a superset of the physics going on in EBIED. It adds sputtering, redeposition, damage and also implantation, but the adsorbate kinetics must follow the same rules.

The following sections generalize and clarify the EBIED and IBIED precursor kinetics into a unified model. This proceeds first by fundamental definitions of a species i (Section B.1), a concentration N (Section B.2), and electron/ion/neutral flux (Section B.3). Then a list of the non-three body processes [1] is made, and grouped into transport (Section B.4), addition (Section B.5) and removal (Section B.6), as in Figure B.1.

B.1 Species i

The surface has material upon it that we distinguish by species. The term *species* carries the traditional meaning, i.e., a molecule or atomic adsorbate, such as H_2O or XeF_2. But additionally, in our model, it distinguishes the type of bond with the surface (i.e., identical molecules can still be classified as different species depending upon whether they are chemisorbed or physisorbed). Notationally, we identify the species by the index i. If it is necessary to distinguish between two species we use i and j. If there is only one species in an equation, we will drop the subscript i.

B.2 Species concentration N

Consider an adsorbate species concentration, N, on the surface. The change in concentration of N on the surface with time, $\frac{\partial N}{\partial t}$, is governed simply by a sum of fluxes (units of [particles time^{-1} length^{-2}]). These fluxes are: the additional material arriving or being created, $\mathcal{A}$, the material being removed or destroyed, $\mathcal{R}$, and the material diffusion[2] along the surface, $\mathcal{D}$.

$$\frac{\partial N}{\partial t} = \mathcal{D} + \mathcal{A} - \mathcal{R} \tag{B.1}$$

There is implicit dependence in all variables on (x, y, z, t).

[1] Throughout, three body processes are excluded as low probability.
[2] Later diffusion is recognized as a form of transport and is subsumed in $\mathcal{T}$

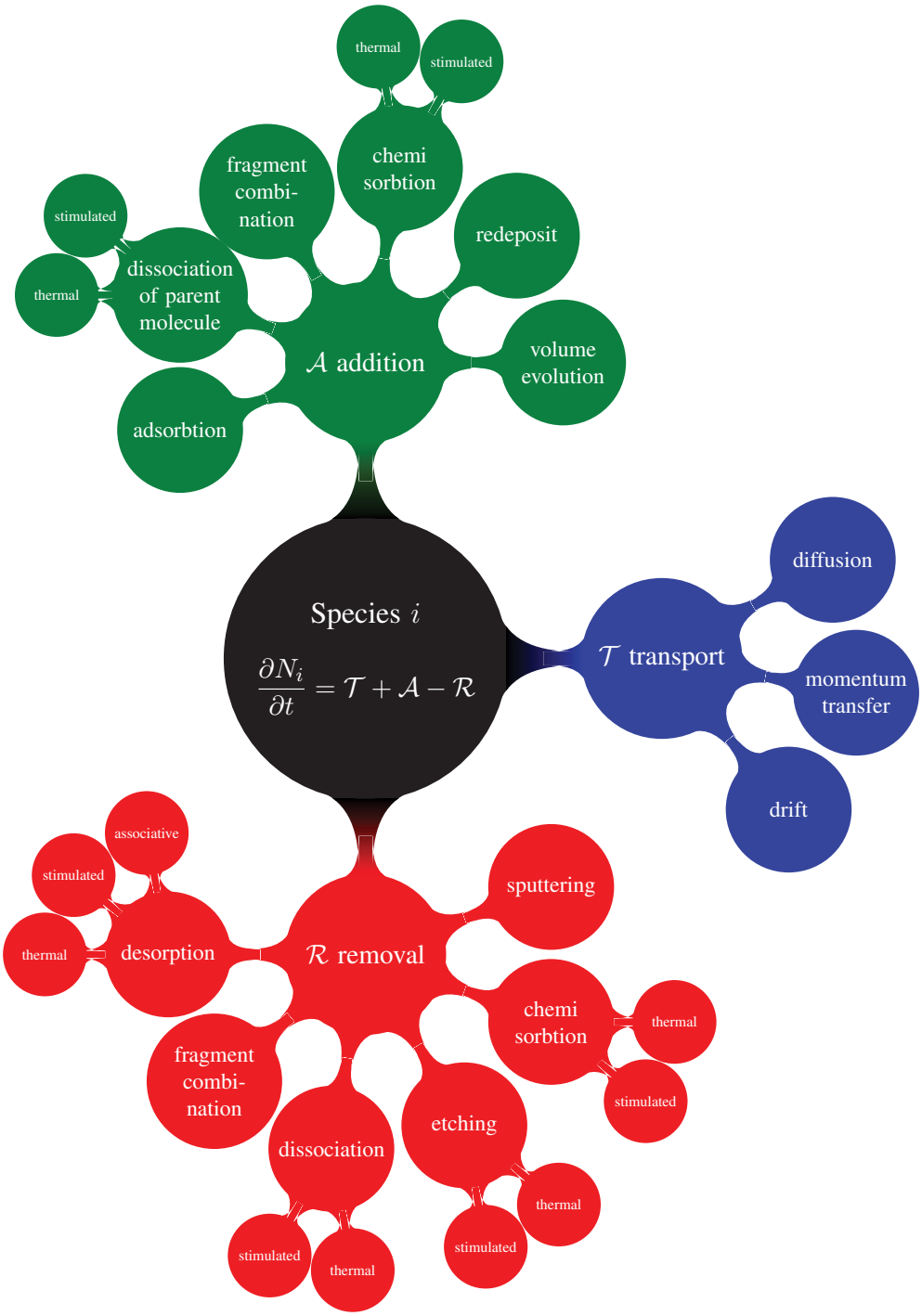

FIGURE B.1: Processes included in the precursor kinetics model that can take place on the surface. Three-body processes are excluded as low probability. Any thermal process may also be activated (stimulated) by an energetic particle (electron, ion, neutral) or photon.

Multiple species yield a set of equations of the form of (B.1) indexed by i. Fragments from adsorbates are included in this index. Species which have more than one type of surface interaction (physisorbed or chemisorbed) are treated distinctly by this index as well.

It is worth noting that (B.1) is a reaction-diffusion equation, where $+\mathcal{A}-\mathcal{R}$ account for the reaction component. This hints at the possibility of exploring nanopattering by chemical effects driven by the charged particle beam.

Addition, removal, and diffusion themselves consist of component fluxes from different processes, see Figure B.1. These categories are itemized and expanded below.

B.3 Flux of electrons, ions, and neutrals

Some processes acting on surface species populations are strongly affected by electrons (and ions and neutrals) passing the surface boundary in either direction (bulk to vacuum, or vacuum to bulk.) Photons are not included here, although they can affect surface species, as can be seen in examples of laser induced etching and deposition [229–231].

Dissociation or fragmentation by a flux of particles through the surface requires some bookkeeping. The electrons interacting with the surface have a distribution of energies. E.g. primary electrons have a narrow range of high energies, while secondary electrons have a broad range of lower energies. We define the flux distribution of electrons as f_e and note that it is comprised of primary, secondary and backscattered electrons

$$f_e = f_{PE} + f_{BSE} + f_{SE_1} + f_{SE_2} \tag{B.2}$$

Implicitly, these flux distributions all vary with energy of the particle, $f = f(E)$, and they have units [particles time^{-1} energy^{-1} length^{-2}]. A flux would be given by integrating over energy fdE, and a number of electrons by further integrating over an area $fdEdA$.

Similarly, we define the flux of neutral atoms/molecules as the sum of the backscattered ions (which are all assumed to be neutral after first interaction with the surface), sputtered material

(typically neutral [232] such that $\alpha \approx 0.95$), and redepositing atoms

$$f_{neutral} = f_{BS} + \alpha f_S + f_R \tag{B.3}$$

and the ion flux as the primary ion beam, and

$$f_{ion} = f_{PI} + (1 - \alpha) f_S \tag{B.4}$$

where ion and $neutral$ must be replaced with the specific ion, atom or molecule, e.g., f_{Ga^+} or f_{Si} or f_{XeF_2} .

These fluxes are evaluated with an effective cross-section σ of units [length^2], yielding a rate distribution over energy. This follows notation used in the literature, originally by Allen in 1988 [233], and then by Utke [25], Botman [234] and Dorp [22]. The total number of interactions for a species depends on the concentration N and integrated over energy

$$N \int_0^\infty f(E)\sigma(E)dE \tag{B.5}$$

The cross-section is specific to the species, type of flux, type of process (desorption or fragmentation). In relations below, we will not notate the cross-section with all three, but only with mechanism, since the species and flux will be obvious from surrounding terms. E.g., we will later write for the electron desorption cross-section,

$$\mathcal{R}_{esd} = N_i \int_0^\infty f_e \sigma_d dE \tag{B.6}$$

understanding from context this is specific to electron flux with species i, rather than the more cumbersome triply sub-scripted $\sigma_{i,e,d}$. This form assumes that each electron can contribute to every electron-induced process (i.e., all dissociation and desorption processes). Thus there is no bookkeeping done to prevent a single electron (or ion or neutral) from contributing to multiple pathways.

To refer to all fluxes with their attendant cross-sections we will use the $\bullet$ notation as a "wildcard", so that

$$\mathcal{R}_{\bullet sd} = \mathcal{R}_{esd} + \mathcal{R}_{nsd} + \mathcal{R}_{isd} \tag{B.7}$$

where n and i represent neutral and ion.[3]

Finally, it should be noted that shot noise in the electron or ion beam may be a significant source of surface roughening. Adding this noise to the flux term f may restrict simulation numerically, requiring the timestep resolution to be small. It would be challenging to simulate but could indicate how the physics acts.

B.4 Transport $\mathcal{T}$

The main mechanism of transport is diffusion, though there are other processes that can be beam driven, such as momentum transfer [33]. Diffusion acts to equalize concentrations over the surface [75]. When the diffusion coefficient D is constant over surface it allows Fick's second law to yield $D\nabla^2 N$.

$$\mathcal{D} = D_i \nabla^2 N_i \tag{B.8}$$

Here (B.8) contains a second order spatial derivative (the Laplacian $\nabla^2 \equiv \triangle$) which takes care of the local surface curvature and will vary with coordinate system. When implementing a simulation of surface evolution, the discretization of the diffusion must be performed carefully.

The diffusion speed of each species will vary based on natural diffusion rates. A species which has chemisorbed to the surface will have a higher activation barrier than a physisorbed molecule, but can still diffuse. If different species interact, this will influence the diffusion, causing it to depart from "free" diffusion. In more complex situations, the diffusion of one species may compete with another, and hence may depend on the total coverage, $D_i = D_i(\Theta)$.

Transport speeds are critical to interesting behaviour. Turing [235] observed that the only necessity for patterns to arise in Reaction-Diffusion systems (RD systems) is that the diffusion rates of different species differ.

[3] Note that this briefly introduces a naming collision, but the intent should be clear from the context. Only with processes will we specify i for "ion", and in the majority of the chapter uses i for species.

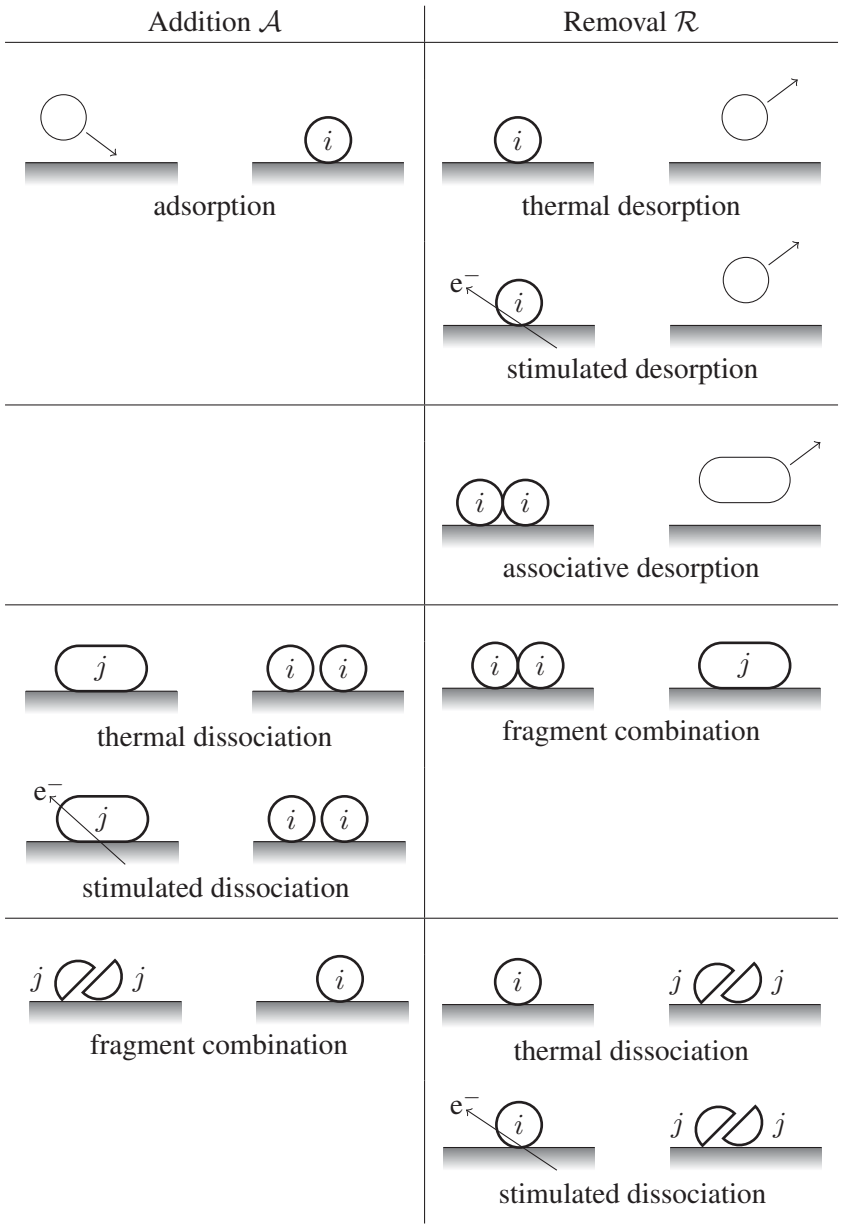

FIGURE B.2: Schematics of elemental surface interactions with respect to species i, arranged to reveal their symmetry. Three body interactions are excluded as low probability (e.g., there is no "stimulated associative desorption", as it would require two adsorbates and an electron.) Any process that can happen thermally can also be stimulated. "Stimulation" may come from flux of (e^-, i^+, n).

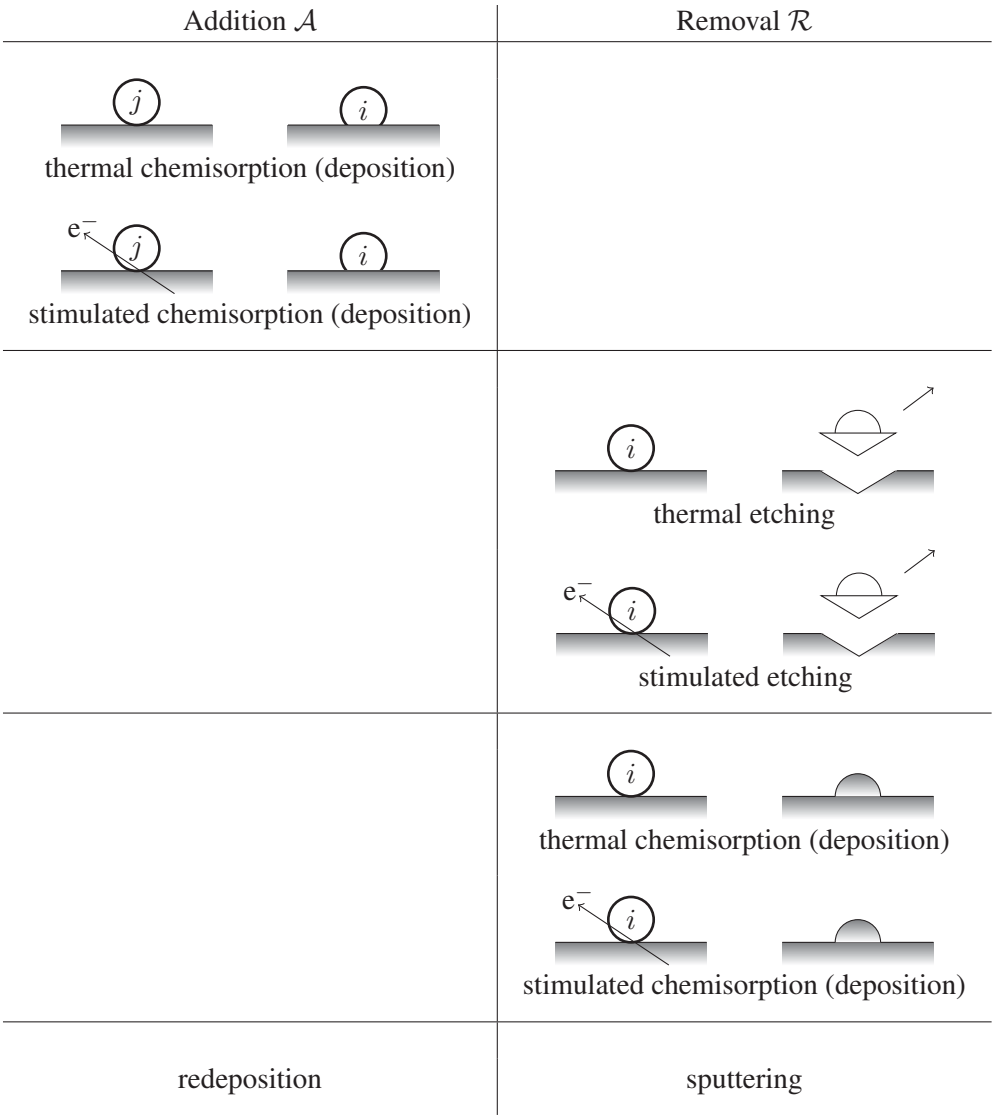

FIGURE B.3: Schematics of elemental surface interactions (continued).

B.5 Addition $\mathcal{A}$

Addition of material on the surface comes from a sum of flux terms each illustrated in Figures B.2 and B.3. Each process is explained in a subsection below.

B.5.1 Adsorption

Flux of adsorbates, $\mathcal{A}_a$, attaching to surface sites depends on the models for gas flux and coverage.

The gas flux, F, might be modelled as simply as a constant uniform pressure (constant flux), or might include a distribution based on gas nozzle effects, or a trajectory model based on a clear path into a recessed part of the surface (e.g., Clausing model into an etch pit [26]). The sticking coefficient s in the range 0 to 1, is combined with gas flux to yield the flux of sticking particles sF.

The surface coverage, Θ, is the fraction of adsorption sites occupied and is given by the area of adsorption site multiplied by the concentration of the adsorbate AN. When multiple species are present, the total coverage is calculated by summing over all species,

$$\Theta = \sum_i \Theta_i = \sum_i A_i N_i \tag{B.9}$$

A choice of surface coverage model determines the adsorption isotherm. Specifying that only one monolayer (ML) adsorbs is a common choice, which specifies the Langmuir isotherm. In this case we calculate $\mathcal{A}_a$ as

$$\mathcal{A}_a = sF(1 - \Theta) \tag{B.10}$$

Different isotherms can be specified, for example, specifying that molecules can form multiple layers is treated by the Brunauer–Emmett–Teller (BET) isotherm.

Adsorbate-adsorbate interaction may be accounted for in the diffusion terms, but can be excluded here as it requires a higher than 2-body interaction at the time of landing. After landing onto the surface, the diffusion process can account for adsorbate-adsorbate interactions.

Finally, there may be more than one adsorbate per gas molecule, as in the case of dissociative chemisorption (observed for H_2 onto Cu(111)) [236].

B.5.2 Thermal dissociation

If a species on the surface, j, thermally dissociates into one or more of the species of interest i, then we have

$$\mathcal{A}_{td} = n_{ij} \frac{N_j}{\tau_{td}} \tag{B.11}$$

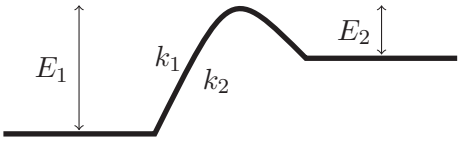

FIGURE B.4: A reaction-coordinate diagram showing the different energies E_1 and E_2 needed to cross a barrier and the transition rates $k_1 = A_1 e^{-E_1/k_B T}$ (moving from the lower to higher energy level) and $k_2 = A_2 e^{-E_2/k_B T}$ (higher to lower). Heat or energetic particles can drive this reaction either way.

where n_{ij} is the number of fragments of i which come from j. This can also be expressed as a rate $k = 1/\tau$, whichever is more relevant to experiment. The rate factor k is typically assumed to be of an Arrhenius form, describing a transition between two energy levels over a barrier, see Figure B.4.

B.5.3 Stimulated dissociation

If the species i under consideration is a long-lived fragment of a parent molecule j, then it does not arrive at the surface by adsoprtion at all, but is only created by (say, electron) dissociation of the "parent" molecule j under by electron flux. This dissociation is a product of the flux distribution and the cross-section for the probability of occurring,

$$\mathcal{A}_{esd} = n_{ij} N_j \int_0^\infty f_e \sigma_{sd} dE \tag{B.12}$$

where n_{ij} is the number of fragments of i which come from j. Of course, generally, this activation may also arise from ion or neutral atom, as described in Section B.3

$$\mathcal{A}_{isd} = n_{ij} N_j \int_0^\infty f_{ion} \sigma_{sd} dE \tag{B.13}$$

$$\mathcal{A}_{nsd} = n_{ij} N_j \int_0^\infty f_{neutral} \sigma_{sd} dE \tag{B.14}$$

incorporating all terms that are stimulated by a particle $\bullet$ requires a sum so that

$$\mathcal{A}_{\bullet sd} = \mathcal{A}_{esd} + \mathcal{A}_{isd} + \mathcal{A}_{nsd} \tag{B.15}$$

B.5.4 Fragment combination

If the species of adsorbate i, can be fragmented into another species j, on the surface by the flux of energy, these fragments spontaneously recombine with half-life, τ_r, yielding another "source" term

$$\mathcal{A}_{fc} = \frac{1}{n_j}\frac{N_j}{\tau_r} \tag{B.16}$$

where n_j is the number of molecules of type j that must combine.

B.5.5 Thermal chemisorption

If the species interacting with the surface allows for a chemisorbed state, i, as well as a physisorbed state, j, then instead of only arriving from the gas phase, it might also arrive from the physisorbed state. A particle physisorbed to the surface may become chemisorbed with some rate

$$\mathcal{A}_{tc} = k_{tc}N_i \tag{B.17}$$

We neglect the complementary process "thermal physisorption" as the probability of the precise energy to leave the deep potential well of chemisorption, with not too much energy to also leave physisorption, is negligible.

B.5.6 Stimulated chemisorption

This physisorption to chemisorption transition may also be activated (or "stimulated") by a passing electron,

$$\mathcal{A}_{esc} = N_j \int_0^\infty f_e \sigma_{ac} dE \tag{B.18}$$

As before (Section B.5.3) this activation may be by electron, ion or neutral particles, so we reuse the notation introduced in Section B.3 for the term $\mathcal{A}_{\bullet sc}$. As above, we neglect the complementary process of "stimulated physisorption".

B.5.7 Redeposition of sputtered material

In the case of the focused ion beam (FIB), material will be sputtered from surfaces under the beam, and redeposit elsewhere on the surface. This is the main **non-local** aspect introduced by FIB. Redeposition is a non-linear process [237] involving the geometry of the whole surface, and must be computed by an external model. We denote this flux by $\mathcal{A}_R$.

B.5.8 Volume evolution

Volume evolution can happen specifically with the ion beam, as the ion species is implanted over time into the substrate. Milling away top layers can expose this evolved volume to the surface, and contribute to the concentration of a species on the surface. Milling can also induce a stoichiometric imbalance by driving different species deeper into the bulk, or preferentially milling other species. When ions are implanted under the surface, they may eventually contribute to a surface species if the volume above is sputtered away, or if the implanted species migrate to the surface. Additionally, a stoichiometric imbalance can be generated in situations where preferential sputtering occurs, or the ion frees up certain species more than others, as in the recently studied growth of GaF pillars [35]. These situations involve models of volume evolution, with no simple analytic form. A model must couple with the species tracker and we represent it by $\mathcal{A}_{VE}$.

B.5.9 Total addition

Finally the total addition term $\mathcal{A}$ can be expressed as the sum of the possible components

$$\mathcal{A} = \mathcal{A}_a + \mathcal{A}_{td} + \mathcal{A}_{\bullet sd} + \mathcal{A}_{fc} + \mathcal{A}_{tc} + \mathcal{A}_{\bullet sc} + \mathcal{A}_R + \mathcal{A}_{VE} \tag{B.19}$$

B.6 Removal $\mathcal{R}$

Removal of material on the surface comes from a sum of flux terms each illustrated in Figures B.2 and B.3. Each process is explained in a subsection below.

B.6.1 Thermal desorption

The adsorbate can desorb from the surface through several mechanisms; thermal desorption, associated desorption, exothermic desorption, and stimulated desorption. Thermal desorption, $\mathcal{R}_t$, acts at a rate specified by k_t, and is given by

$$\mathcal{R}_t = k_t N_i \tag{B.20}$$

Thermal desorption promoted by exothermicity of reaction may also occur as in the XeF_2 reaction with Si [238].

B.6.2 Stimulated desorption

Electron stimulated desorption, as previously described by (B.6), is

$$\mathcal{R}_{esd} = N_i \int_0^\infty f_e \sigma_d dE \tag{B.21}$$

while neutral stimulated desorption takes the atomic Z dependent form

$$\mathcal{R}_{nsd} = N_i \int_0^\infty f_{neutral} \sigma_d dE \tag{B.22}$$

and ion stimulated desorption takes the atomic Z dependent form

$$\mathcal{R}_{isd} = N_i \int_0^\infty f_{ion} \sigma_d dE \tag{B.23}$$

As before (Section B.3) we sum these terms into $\mathcal{R}_{\bullet sd} = \mathcal{R}_{esd} + \mathcal{R}_{nsd} + \mathcal{R}_{isd}$.

B.6.3 Associative desorption

The associative desorption mechanism requires two adsorbates to meet, kinetically overcome an energy barrier to bond, and desorb. This takes the form of the energetic probability condition k times the positional probability condition $N_i \Theta_i$

$$\mathcal{R}_a = k_a N_i \Theta_i = k_a N_i (A_i N_i) \tag{B.24}$$

and we neglect three body associations as too small to occur.

B.6.4 Fragment combination

If there are associative mechanisms other than desorption, they also represent a negative flux on the adsorbate species under consideration. The form is just the same as above in Section B.5.4,

$$\mathcal{R}_{fc} = \frac{N_j}{\tau_r} \tag{B.25}$$

and this is the "sink" term for the "source" term (and so mass is conserved).

B.6.5 Thermal dissociation

It is possible for a species i to spontaneously dissociate on the surface (into one or more js). This is given by

$$\mathcal{R}_{tdi} = \frac{N_i}{\tau_{tdi}} \tag{B.26}$$

B.6.6 Stimulated dissociation

The contribution to removal of adsorbates by electron, ion, neutral dissociation parallels stimulated desorption and is treated as before (see Section B.6.2). It is given by $\mathcal{R}_{\bullet sdi}$.

B.6.7 Thermal etching

A species i on the surface may spontaneously alter the surface by chemisorbing and volatilizing a part of the surface (a.k.a. etching). In both cases the species is removed from the model and the surface geometry is incrementally updated accordingly. The term for thermal modification of the surface is

$$\mathcal{R}_{te} = k_{te} N_i \tag{B.27}$$

B.6.8 Stimulated etching

Etching of the surface can be stimulated as well, and is given by the summation term $\mathcal{R}_{\bullet se}$.

B.6.9 Thermal chemisorption

In exactly the same process as in Section B.5.5 we might "lose" concentration to chemisorption. A species i is removed from the model and the surface geometry is incrementally updated accordingly. The term for thermal chemisorption is

$$\mathcal{R}_{tc} = k_{tc} N_i \tag{B.28}$$

B.6.10 Stimulated chemisorption

This process can be stimulated as well, and complementary to Section B.5.6, is given by the summation term $\mathcal{R}_{\bullet sc}$.

B.6.11 Sputtering

Material given enough momentum can overcome the surface's binding energy, and can exit the bulk as *sputter*. This is most commonly seen as a FIB-specific process, although it is possible for carbon and most other atoms to be sputtered in a high energy transmission electron microscope (TEM) [239]. Sputter can be computed in detail by models like binary collision algorithms (BCA), such as TRIM, or molecular dynamics simulations (MD). We term this component $\mathcal{R}_S$.

B.6.12 Consumption in surface reactions

The adsorbate can interact with one or more surface sites, creating a volatile species (etching the surface) or bonding (depositing onto the surface). In either case, the concentration of species i is depleted at the rate given by

$$\mathcal{R}_i = k_i (A_i N_i)^{\zeta_i} \tag{B.29}$$

where $\zeta_i = 1$ if the reaction is elementary. Surface modification over time leads to new topography and influences the diffusion supply rate. The velocity of surface growth, normal to the surface, is given by

$$\frac{\partial x}{\partial t} = \omega V_i \mathcal{R}_i \tag{B.30}$$

where $\omega = \pm 1$ for deposition or etching, and V_i is the volume of a single molecule removed from or added to the substrate as a result of a reaction between species i and surface site.

B.6.13 Total removal

Finally the total removal term $\mathcal{R}$ can be expressed as the sum of the possible components

$$\mathcal{R} = \mathcal{R}_t + \mathcal{R}_{\bullet sd} + \mathcal{R}_a + \mathcal{R}_{fc} + \mathcal{R}_{tdi} + \mathcal{R}_{\bullet sdi} + \mathcal{R}_{te} + \mathcal{R}_{\bullet se} + \mathcal{R}_{tc} + \mathcal{R}_{\bullet sc} + \mathcal{R}_S + \mathcal{R}_i \tag{B.31}$$

B.7 Conclusions

This mathematical model can provide order to the building up of adsorbate continuum equations for EBIED / IBIED processes. Many physical processes can be included, and many species. The form of the resulting model will be a linear set of coupled PDE equations, where negligible terms are zeroed.

Appendix C

Modelling code

Source code will not be listed in the thesis for brevity, instead, summary statistics are included, see table C.1. The Julia language [202] was chosen because it is expressive and fast. Powerful code can be written rapidly. Libraries were available for solving well-known numerical problems (optimization, root finding, sparse matrix evaluation, etc.). All algorithms below have low cyclomatic complexity, making them easy to maintain, and they were profiled for targeted optimizations [240].

Simulation output in two-dimensions was plotted with the Julia package called Gadfly [220]. Three-dimensional output was analysed and rendered with ParaView [179]. The most difficult part of implementing the level set method is the fast marching method. The sparse field method also requires careful bookkeeping to achieve its promised optimizations.

Contact the author `alanbahm@gmail.com` for questions about the source code.

Filename	# functions	# lines	size (kB)
GaN pillar simulation			
_simulate_growth.py	2	474	21
fit_data.py	1	162	5
load_data.py	2	39	2
plot_data.py	2	476	18
run_model.py	0	116	5
run_plot.py	0	24	0.5
	9	**1291**	**51.5**
BCA simulation			
material.jl	2	110	4
scatter.jl	26	428	13
trajectory.jl	7	752	30
trim.jl	10	334	11
	48	**1624**	**58**
Level set method			
levelset_2d.jl	16	826	21
levelset_2d_test.jl	20	764	21
levelset_3d.jl	16	991	27
levelset_3d_test.jl	13	299	7
sparsefield_2d.jl	9	590	13
sparsefield_2d_test.jl	13	448	11
	87	**3918**	**100**
Closest point method			
cpm.jl	4	110	10
cpm_2d.jl	11	706	21
cpm_3d.jl	10	673	19
cpm_paraview.jl	2	239	7
	27	**1728**	**57**
Mass limited transport simulation			
mtl_deposition_2d.jl	7	639	29
mtl_deposition_3d.jl	12	630	27
	19	**1269**	**56**

TABLE C.1: Statistics on the simulation code written for this thesis. The primary language was Julia, and python was also used. The expressiveness of these languages and available libraries allowed the total code sizes to be quite small.

Appendix D

Arrhenius form

The presence of the Arrhenius form in physical reactions is not surprising as it can be arrived at by several natural steps.

1. Assuming symmetry of space
2. Equipartitioning of energy in system
3. Boltzmann distribution $\rho = Axe^{-x^2/B}$ (not symmetric about maximum, see Figure D.1)
4. Assume a threshold E_a for activation of something to happen
5. Integrate ρ as $\int_{E_a}^{\infty} \rho(E)dE$ for probability to activate
6. Yields an Arrhenius form $k = k_o e^{-E_a/kT}$

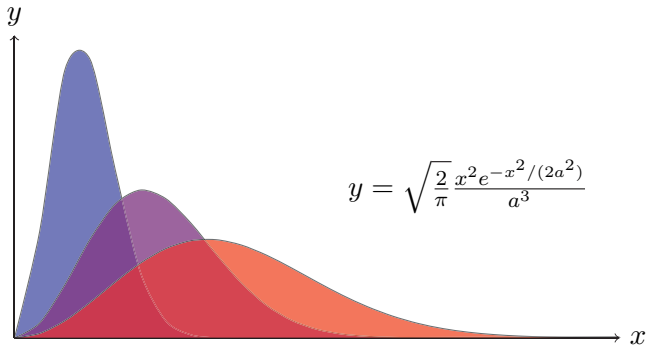

FIGURE D.1: Example of Maxwell-Boltzmann distributions which govern the amount of particles with a given energy (or velocity). Three different "temperatures" are shown.

Bibliography

[1] T M Mayer. “Simulation of plasma-assisted etching processes by ion-beam techniques”. In: *Journal of Vacuum Science and Technology* 21.3 (Sept. 1982), p. 757. DOI: 10.1116/1.571821.

[2] L R Harriott. “Digital scan model for focused ion beam induced gas etching”. In: *Journal of Vacuum Science and Technology B: Microelectronics and Nanometer Structures* 11.6 (Nov. 1993), p. 2012. DOI: 10.1116/1.586535.

[3] F. G. Rüdenauer. “Localized ion beam induced deposition of Al-containing layers”. In: *Journal of Vacuum Science and Technology B: Microelectronics and Nanometer Structures* 6.5 (Sept. 1988), p. 1542. DOI: 10.1116/1.584211.

[4] A D Dubner and A Wagner. “The role of gas adsorption in ion-beam-induced deposition of gold”. In: *Journal of Applied Physics* 66.2 (1989), p. 870. DOI: 10.1063/1.343512.

[5] Patricia G Blauner. “Focused ion beam fabrication of submicron gold structures”. In: *Journal of Vacuum Science and Technology B: Microelectronics and Nanometer Structures* 7.4 (July 1989), p. 609. DOI: 10.1116/1.584803.

[6] P.J. Heard and P.D. Prewett. “Focused ion beam deposition of carbon for photomask repair”. In: *Microelectronic Engineering* 11.1-4 (Apr. 1990), pp. 421–425. DOI: 10.1016/0167-9317(90)90143-H.

[7] Anil Gandhi. “Parametric modeling of focused ion beam induced etching”. In: *Journal of Vacuum Science and Technology B: Microelectronics and Nanometer Structures* 8.6 (Nov. 1990), p. 1814. DOI: 10.1116/1.585165.

[8] H.-C. Petzold. “Ion-induced deposition for x-ray mask repair: Rate optimization using a time-dependent model”. In: *Journal of Vacuum Science and Technology B: Microelectronics and Nanometer Structures* 9.5 (Sept. 1991), p. 2664. DOI: 10.1116/1.585668.

[9] R J Young. “Characteristics of gas-assisted focused ion beam etching”. In: *Journal of Vacuum Science and Technology B: Microelectronics and Nanometer Structures* 11.2 (Mar. 1993), p. 234. DOI: 10.1116/1.586708.

[10] Klaus Edinger and Thomas Kraus. “Modeling of focused ion beam induced surface chemistry”. In: *Journal of Vacuum Science and Technology B: Microelectronics and Nanometer Structures* 18.6 (2000), p. 3190. DOI: 10.1116/1.1321761.

[11] Klaus Edinger and Thomas Kraus. “Modeling of focused ion beam induced chemistry and comparison with experimental data”. In: *Microelectronic Engineering* 57-58 (2001), pp. 263–268. DOI: 10.1016/S0167-9317(01)00487-7.

[12] Christoph Ebm, Gerhard Hobler, Simon Waid, and Heinz D Wanzenboeck. “Modeling of precursor coverage in ion-beam induced etching and verification with experiments using XeF$_2$ on SiO$_2$”. In: *Journal of Vacuum Science and Technology B: Microelectronics and Nanometer Structures* 28.5 (2010), p. 946. DOI: 10.1116/1.3481139.

[13] Christoph Ebm, Gerhard Hobler, Simon Waid, and Heinz D Wanzenboeck. “Quantitative simulation of ion-beam induced deposition of nanostructures”. In: *Journal of Vacuum Science and Technology B: Microelectronics and Nanometer Structures* 29.1 (2011), p. 011031. DOI: 10.1116/1.3533951.

[14] Heung-Bae Kim, Gerhard Hobler, Andreas Steiger, Alois Lugstein, and Emmerich Bertagnolli. “Level set approach for the simulation of focused ion beam processing on the micro/nano scale”. In: *Nanotechnology* 18.26 (June 2007), pp. 265307–6. DOI: 10.1088/0957-4484/18/26/265307.

[15] Heung-Bae Kim. “Design, simulation and fabrication of micro/nano functional structures using ion beams”. PhD thesis. Vienna University of Technology: Vienna University of Technology, Apr. 2007.

[16] N Silvis-Cividjian, C.W. Hagen, L.H.A. Leunissen, and P. Kruit. “The role of secondary electrons in electron-beam-induced-deposition spatial resolution”. In: *Microelectronic Engineering* 61-62 (2002), pp. 693–699. DOI: 10.1016/S0167-9317(02)00515-4.

[17] Z Q Liu, Kazutaka Mitsuishi, and Kazuo Furuya. “A dynamic Monte Carlo study of the in situ growth of a substance deposited using electron-beam-induced deposition”. In: *Nanotechnology* 17.15 (July 2006), pp. 3832–3837. DOI: 10.1088/0957-4484/17/15/038.

[18] S J Randolph, J D Fowlkes, and P D Rack. “Focused, Nanoscale Electron-Beam-Induced Deposition and Etching”. In: *Critical Reviews in Solid State and Materials Sciences* 31.3 (Sept. 2006), pp. 55–89. DOI: 10.1080/10408430600930438.

[19] J D Fowlkes, S J Randolph, and P D Rack. “Growth and simulation of high-aspect ratio nanopillars by primary and secondary electron-induced deposition”. In: *Journal of Vacuum Science and Technology B: Microelectronics and Nanometer Structures* 23.6 (2005), p. 2825. DOI: 10.1116/1.2101732.

[20] D A Smith, J D Fowlkes, and P D Rack. “A nanoscale three-dimensional Monte Carlo simulation of electron-beam-induced deposition with gas dynamics.” In: *Nanotechnology* 18.26 (June 2007), p. 265308. DOI: 10.1088/0957-4484/18/26/265308.

[21] Milos Toth, Charlene J Lobo, Gavin Hartigan, and W Ralph Knowles. “Electron flux controlled switching between electron beam induced etching and deposition”. In: *Journal of Applied Physics* 101.5 (2007), p. 54309. DOI: 10.1063/1.2437667.

[22] W F van Dorp and Cornelis W Hagen. “A critical literature review of focused electron beam induced deposition”. In: *J. Appl. Phys.* 104.8 (2008), p. 081301. DOI: 10.1063/1.2977587.

[23] Charlene J Lobo, Milos Toth, Raymond Wagner, Bradley L Thiel, and Michael Lysaght. “High Resolution Radially Symmetric Nanostructures from Simultaneous Electron Beam Induced Etching and Deposition”. In: *Nanotechnology* 19.2 (Dec. 2007), p. 25303. DOI: 10.1088/0957-4484/19/02/025303.

[24] Ivo Utke, Vinzenz Friedli, Martin Purrucker, and Johann Michler. “Resolution in focused electron- and ion-beam induced processing”. In: *Journal of Vacuum Science and Technology B: Microelectronics and Nanometer Structures* 25.6 (2007), pp. 2219–2223. DOI: 10.1116/1.2789441. arXiv: 0703539 [cond-mat].

[25] Ivo Utke, Patrik Hoffmann, and John Melngailis. “Gas-assisted focused electron beam and ion beam processing and fabrication”. In: *Journal of Vacuum Science and Technology B: Microelectronics and Nanometer Structures* 26.4 (2008), p. 1197. DOI: 10.1116/1.2955728.

[26] Steven Randolph, Milos Toth, Jared Cullen, Clive Chandler, and Charlene Lobo. “Kinetics of gas mediated electron beam induced etching”. In: *Applied Physics Letters* 99.21 (2011), p. 213103. DOI: 10.1063/1.3662928.

[27] Charlene J Lobo, Aiden Martin, Matthew R Phillips, and Milos Toth. “Electron beam induced chemical dry etching and imaging in gaseous NH$_3$ environments.” In: *Nanotechnology* 23.37 (Aug. 2012), p. 375302. DOI: 10.1088/0957-4484/23/37/375302.

[28] Michael Huth, Fabrizio Porrati, Christian Schwalb, Marcel Winhold, Roland Sachser, Maja Dukic, Jonathan Adams, and Georg Fantner. “Focused electron beam induced deposition: A perspective”. In: *Beilstein Journal of Nanotechnology* 3 (Aug. 2012), pp. 597–619. DOI: 10.3762/bjnano.3.70.

[29] James Bishop, Milos Toth, Matthew Phillips, and Charlene Lobo. “Effects of oxygen on electron beam induced deposition of SiO$_2$ using physisorbed and chemisorbed tetraethoxysilane”. In: *Applied Physics Letters* 101.21 (2012), p. 211605. DOI: 10.1063/1.4767521.

[30] James Bishop, Charlene J Lobo, Aiden Martin, Mike Ford, M R Phillips, and Milos Toth. “The role of activated chemisorption in electron beam induced deposition”. In: *Physical Review Letters* 109.14 (Oct. 2012), p. 146103. DOI: 10.1103/PhysRevLett.109.146103.

[31] Konrad Rykaczewski, William B White, and Andrei G Fedorov. “Analysis of electron beam induced deposition (EBID) of residual hydrocarbons in electron microscopy”. In: *Journal of Applied Physics* 101.5 (2007), pp. 54307–1. DOI: 10.1063/1.2437065.

[32] Jared Craig Cullen. “Localised Probing of Precursor Coefficients Using Electron Beam Induced Deposition and Etching”. PhD thesis. University of Technology, Sydney, May 2015.

[33] R Mark Bradley and Patrick D Shipman. “Spontaneous Pattern Formation Induced by Ion Bombardment of Binary Compounds”. In: *Physical Review Letters* 105.14 (Oct. 2010), p. 145501. DOI: 10.1103/PhysRevLett.105.145501.

[34] Qiangmin Wei, Jie Lian, Wei Lu, and Lumin Wang. “Highly ordered Ga nanodroplets on a GaAs surface formed by a focused ion beam”. In: *Physical Review Letters* 100.7 (Feb. 2008), p. 76103. DOI: 10.1103/PhysRevLett.100.076103.

[35] Aurelien Botman, Alan Bahm, Steven Randolph, Marcus Straw, and Milos Toth. “Spontaneous Growth of Gallium-Filled Microcapillaries on Ion-Bombarded GaN”. In: *Physical Review Letters* 111.13 (Sept. 2013), p. 135503. DOI: 10.1103/PhysRevLett.111.135503.

[36] Xin Ou, Adrian Keller, Manfred Helm, Jürgen Fassbender, and Stefan Facsko. “Reverse Epitaxy of Ge: Ordered and Faceted Surface Patterns”. In: *Physical Review Letters* 111.1 (July 2013), p. 16101. DOI: 10.1103/PhysRevLett.111.016101. arXiv: arXiv:1303.5133v1.

[37] Steven J Randolph, Aurelien Botman, and Milos Toth. “Deposition of highly porous nanocrystalline platinum on functionalized substrates through fluorine-induced decomposition of Pt(PF$_3$)$_4$ adsorbates”. In: *Particle and Particle Systems Characterization* 30.8 (June 2013), pp. 672–677. DOI: 10.1002/ppsc.201300036.

[38] Toby W Shanley, Aiden A Martin, Igor Aharonovich, and Milos Toth. “Localized chemical switching of the charge state of nitrogen-vacancy luminescence centers in diamond”. In: *Applied Physics Letters* 105.6 (Aug. 2014), p. 63103. DOI: 10.1063/1.4883229. arXiv: 1406.0987.

[39] Laurent Bernau, Mihai Gabureac, Rolf Erni, and Ivo Utke. “Tunable Nanosynthesis of Composite Materials by Electron-Impact Reaction”. In: *Angewandte Chemie International Edition* 49.47 (Nov. 2010), pp. 8880–8884. DOI: 10.1002/anie.201004220.

[40] Ivo Utke, Stanislav Moshkalev, and Phillip Russel. *Nanofabrication using focused ion and electron beams: principles and applications*. Oxford University Press, USA, 2012, p. 840.

[41] Marco Esposito, Vittorianna Tasco, Massimo Cuscunà, Francesco Todisco, Alessio Benedetti, Iolena Tarantini, Milena De Giorgi, Daniele Sanvitto, and Adriana Passaseo. "Nanoscale 3D Chiral Plasmonic Helices with Circular Dichroism at Visible Frequencies". In: *ACS Photonics* 2.1 (Jan. 2015), pp. 105–114. DOI: 10.1021/ph500318p.

[42] Eun-Khwang Lee, Jung-Hwan Song, Kwang-Yong Jeong, Ju-Hyung Kang, Hong-Gyu Park, and Min-Kyo Seo. "Resonant light scattering from a single dielectric nano-antenna formed by electron beam-induced deposition". In: *Scientific Reports* 5 (May 2015), p. 10400. DOI: 10.1038/srep10400.

[43] Hakkı Acar, Toon Coenen, Albert Polman, and Laurens Kobus Kuipers. "Dispersive Ground Plane Core–Shell Type Optical Monopole Antennas Fabricated with Electron Beam Induced Deposition". In: *ACS Nano* 6.9 (Sept. 2012), pp. 8226–8232. DOI: 10.1021/nn302907j.

[44] Aleksandar P Ivanov, Kevin J Freedman, Min Jun Kim, Tim Albrecht, and Joshua B Edel. "High Precision Fabrication and Positioning of Nanoelectrodes in a Nanopore". In: *ACS Nano* 8.2 (Feb. 2014), pp. 1940–1948. DOI: 10.1021/nn406586m.

[45] Amalio Fernández-Pacheco, Luis Serrano-Ramón, Jan M Michalik, M Ricardo Ibarra, José M De Teresa, Liam O'Brien, Dorothée Petit, Jihyun Lee, and Russell P Cowburn. "Three dimensional magnetic nanowires grown by focused electron-beam induced deposition". In: *Scientific Reports* 3 (Mar. 2013), p. 1492. DOI: 10.1038/srep01492.

[46] Martin Günter Jenke, Damiana Lerose, Christoph Niederberger, Johann Michler, Silke Christiansen, and Ivo Utke. "Toward Local Growth of Individual Nanowires on Three-Dimensional Microstructures by Using a Minimally Invasive Catalyst Templating Method". In: *Nano Letters* 11.10 (Oct. 2011), pp. 4213–4217. DOI: 10.1021/nl2021448.

[47] L J McGilly, L Feigl, T Sluka, P Yudin, A K Tagantsev, and N Setter. "Velocity Control of 180 degree Domain Walls in Ferroelectric Thin Films by Electrode Modification". In: *Nano Letters* 16.1 (Jan. 2016), pp. 68–73. DOI: 10.1021/acs.nanolett.5b02798.

[48] Ivo Utke and Armin Gölzhäuser. "Small, Minimally Invasive, Direct: Electrons Induce Local Reactions of Adsorbed Functional Molecules on the Nanoscale". In: *Angewandte Chemie International Edition* 49.49 (Dec. 2010), pp. 9328–9330. DOI: 10.1002/anie.201002677.

[49] Christopher R. Arumainayagam, Hsiao-Lu Lee, Rachel B. Nelson, David R. Haines, and Richard P. Gunawardane. “Low-energy electron-induced reactions in condensed matter”. In: *Surface Science Reports* 65.1 (Jan. 2010), pp. 1–44. DOI: 10.1016/j.surfrep.2009.09.001.

[50] Toan Trong Tran, Christopher Elbadawi, Daniel Totonjian, Charlene J. Lobo, Gabriele Grosso, Hyowon Moon, Dirk R. Englund, Michael J. Ford, Igor Aharonovich, and Milos Toth. “Robust Multicolor Single Photon Emission from Point Defects in Hexagonal Boron Nitride”. In: *ACS Nano* (July 2016), acsnano.6b03602. DOI: 10.1021/acsnano.6b03602.

[51] Chung-Soo Kim, Sung-Hoon Ahn, and Dong-Young Jang. “Review: Developments in micro/nanoscale fabrication by focused ion beams”. In: *Vacuum* 86.8 (Feb. 2012), pp. 1014–1035. DOI: 10.1016/j.vacuum.2011.11.004.

[52] Reo Kometani and Sunao Ishihara. “Nanoelectromechanical device fabrications by 3-D nanotechnology using focused-ion beams”. In: *Science and Technology of Advanced Materials* 10.3 (June 2009), p. 034501. DOI: 10.1088/1468-6996/10/3/034501.

[53] Shinji Matsui and Yukinori Ochiai. “Focused ion beam applications to solid state devices”. In: *Nanotechnology* 7.3 (Sept. 1996), pp. 247–258. DOI: 10.1088/0957-4484/7/3/013.

[54] Ampere A Tseng. “Recent developments in micromilling using focused ion beam technology”. In: *Journal of Micromechanics and Microengineering* 14.4 (Apr. 2004), R15–R34. DOI: 10.1088/0960-1317/14/4/R01.

[55] Ampere A. Tseng. “Recent Developments in Nanofabrication Using Focused Ion Beams”. In: *Small* 1.10 (Oct. 2005), pp. 924–939. DOI: 10.1002/smll.200500113.

[56] Khattiya Chalapat, Nikolai Chekurov, Hua Jiang, Jian Li, Babak Parviz, and G. S. Paraoanu. “3D Self-Assembly: Self-Organized Origami Structures via Ion-Induced Plastic Strain (Adv. Mater. 1/2013)”. In: *Advanced Materials* 25.1 (Jan. 2013), pp. 1–1. DOI: 10.1002/adma.201370001.

[57] George M Whitesides. “Self-Assembly at All Scales”. In: *Science* 295.5564 (2002), pp. 2418–2421. DOI: 10.1126/science.1070821. arXiv: arXiv:1011.1669v3.

[58] Stefan Facsko. “Formation of Ordered Nanoscale Semiconductor Dots by Ion Sputtering”. In: *Science* 285.5433 (Jan. 1999), pp. 1551–1553. DOI: 10.1126/science.285.5433.1551.

[59] Johannes V Barth, Giovanni Costantini, and Klaus Kern. “Engineering atomic and molecular nanostructures at surfaces”. In: *Nature* 437.7059 (Sept. 2005), pp. 671–679. DOI: 10.1038/nature04166.

[60] Wei Lu and Charles M Lieber. “Nanoelectronics from the bottom up”. In: *Nature Materials* 6.11 (Nov. 2007), pp. 841–850. DOI: 10.1038/nmat2028.

[61] Kurt W Kolasinski. “Catalytic growth of nanowires: Vapor-liquid-solid, vapor-solid-solid, solution-liquid-solid and solid-liquid-solid growth”. In: *Current Opinion in Solid State and Materials Science* 10.3-4 (June 2006), pp. 182–191. DOI: 10.1016/j.cossms.2007.03.002.

[62] S.O Kucheyev, J.S Williams, and S.J Pearton. “Ion implantation into GaN”. In: *Materials Science and Engineering: R: Reports* 33.2-3 (May 2001), pp. 51–108. DOI: 10.1016/S0927-796X(01)00028-6.

[63] A Datta, S Dhara, S Muto, C W Hsu, C T Wu, C H Shen, T Tanabe, T Maruyama, K H Chen, L C Chen, and Y L Wang. “Formation and in situ dynamics of metallic nanoblisters in Ga$ˆ+$ implanted GaN nanowires”. In: *Nanotechnology* 16.12 (Oct. 2005), pp. 2764–2769. DOI: 10.1088/0957-4484/16/12/003.

[64] J H Wu, W Ye, B L Cardozo, D Saltzman, K. Sun, H Sun, J F Mansfield, and R S Goldman. “Formation and coarsening of Ga droplets on focused-ion-beam irradiated GaAs surfaces”. In: *Applied Physics Letters* 95.15 (2009), p. 153107. DOI: 10.1063/1.3229889.

[65] K. A. Grossklaus and J. M. Millunchick. “Mechanisms of nanodot formation under focused ion beam irradiation in compound semiconductors”. In: *Journal of Applied Physics* 109.1 (2011), p. 014319. DOI: 10.1063/1.3530839.

[66] L A Christel and J. F. Gibbons. “Stoichiometric disturbances in ion implanted compound semiconductors”. In: *Journal of Applied Physics* 52.8 (1981), pp. 5050–5055. DOI: 10.1063/1.329448.

[67] S O Kucheyev, J S Williams, C Jagadish, J Zou, V S J Craig, and G Li. “Ion-beam-induced porosity of GaN”. In: *Applied Physics Letters* 77.10 (2000), p. 1455. DOI: 10.1063/1.1290722.

[68] S O Kucheyev, J S Williams, J Zou, C Jagadish, and G Li. “Ion-beam-induced dissociation and bubble formation in GaN”. In: *Applied Physics Letters* 77.22 (2000), p. 3577. DOI: 10.1063/1.1330221.

[69] S S Elovikov, I K Khrustachev, A S Mosunov, and V E Yurasova. “Mass dependence of nitride sputtering”. In: *Radiation Effects and Defects in Solids* 158.8 (Aug. 2003), pp. 573–582. DOI: 10.1080/1042015031000078297.

[70] B K Chakraverty. “Grain size distribution in thin films—2. Non-conservative systems”. In: *Journal of Physics and Chemistry of Solids* 28.12 (1967), pp. 2413–2421. DOI: 10.1016/0022-3697(67)90027-3.

[71] Shang-En Wu, Chuan-Pu Liu, Tao-Hung Hsueh, Hung-Chin Chung, Chih-Chin Wang, and Cheng-Yu Wang. “Anomalous formation of InGaN/GaN multiple-quantum-well nanopillar arrays by focused ion beam milling”. In: *Nanotechnology* 18.44 (Oct. 2007), p. 445301. DOI: 10.1088/0957-4484/18/44/445301.

[72] A.S. Barrière, G Couturier, G Gevers, H. Guégan, T Seguelond, A. Thabti, and D Bertault. “Preparation and characterization of gallium(III) fluoride thin films”. In: *Thin Solid Films* 173.2 (June 1989), pp. 243–252. DOI: 10.1016/0040-6090(89)90140-5.

[73] Y. Wang and S. Lin. “Spatial and temporal scaling of oxide cluster aggregation on a liquid-gallium surface”. In: *Physical Review B* 53.10 (1996), pp. 6152–6157. DOI: 10.1103/PhysRevB.53.6152.

[74] I Danaila, P Joly, S M Kaber, and M Postel. *An Introduction to Scientific Computing*. Ed. by Ionut Danaila, Pascal Joly, Sidi Mahmoud Kaber, and Marie Postel. New York, NY: Springer New York, Nov. 2007. DOI: 10.1007/978-0-387-49159-2.

[75] Richard Ghez. *Diffusion Phenomena*. Boston, MA: Springer US, 2001. DOI: 10.1007/978-1-4757-3361-7.

[76] Travis E Oliphant. “Python for Scientific Computing”. In: *Computing in Science and Engineering* 9.3 (2007), pp. 10–20. DOI: 10.1109/MCSE.2007.58.

[77] Stefan Van Der Walt, S Chris Colbert, and Gael Varoquaux. “The NumPy array: A structure for efficient numerical computation”. In: *Computing in Science and Engineering* 13.2 (2011), pp. 22–30. DOI: 10.1109/MCSE.2011.37. arXiv: 1102.1523.

[78] H Riedl, T Persson, and P.-E. Eriksson. “The preparation of metallic $ˆ{67}$Ga and its application in tracer diffusion studies in liquid gallium”. In: *The International Journal of Applied Radiation and Isotopes* 30.8 (Aug. 1979), pp. 481–484. DOI: 10.1016/0020-708X(79)90034-6.

[79] M. Baskes, S. Chen, and F. Cherne. “Atomistic model of gallium”. In: *Physical Review B* 66.10 (Sept. 2002), p. 104107. DOI: 10.1103/PhysRevB.66.104107.

[80] James Albert Sethian. *Level Set Methods and Fast Marching Methods: Evolving Interfaces in Computational Geometry, Fluid Mechanics, Computer Vision, and Materials Science*. Cambridge university press, 1999.

[81] Stanley Osher and Ronald Fedkiw. *Level Set Methods and Dynamic Implicit Surfaces*. Applied Mathematical Sciences. New York: Springer, 2003, p. 273. DOI: 10.1007/b98879.

[82] Stanley Osher. “Level Set Methods”. In: *Geometric Level Set Methods in Imaging, Vision, and Graphics*. New York: Springer-Verlag, pp. 3–20. DOI: 10.1007/0-387-21810-6_1.

[83] T.J. Hubbard. “MEMS design: the geometry of silicon micromachining”. In: *Area* 1994 (1994).

[84] Branislav Radjenović, Jae Koo Lee, and Marija Radmilović-Radjenović. “Sparse field level set method for non-convex Hamiltonians in 3D plasma etching profile simulations”. In: *Computer Physics Communications* 174.2 (Jan. 2006), pp. 127–132. DOI: 10.1016/j.cpc.2005.09.010.

[85] Branislav Radjenović and Marija Radmilović-Radjenović. “Hamilton-Jacobi equation with non-convex Hamiltonians in three dimensional level set simulations of the wet etching of silicon”. In: *Int. Conf. on COMPUTATIONAL CHEMISTRY* (2007), pp. 48–51.

[86] B Radjenovic, M Radmilovic-Radjenovic, and M Mitric. “Application of the level set method on the non-convex Hamiltonians”. In: *Facta universitatis - series: Physics, Chemistry and Technology* 7.1 (2009), pp. 33–44. DOI: 10.2298/FUPCT0901033R.

[87] Marija Radmilović-Radjenović, Branislav Radjenović, and Z.L.J. Petrović. “Application of level set method in simulation of surface roughness in nanotechnologies”. In: *Thin Solid Films* 517.14 (May 2009), pp. 3954–3957. DOI: 10.1016/j.tsf.2009.01.123.

[88] Branislav Radjenović and Marija Radmilović-Radjenović. “Three-Dimensional Simulations of the Anisotropic Etching Profile Evolution for Producing Nanoscale Devices”. In: *Acta Physica Polonica A* 119.3 (Mar. 2011), pp. 447–450. DOI: 10.12693/APhysPolA.119.447.

[89] Branislav Radjenović. “Application of the Level Set Method in Three-Dimensional Simulations of the Profile Evolution”. In: *International Research Journal of Pure and Applied Chemistry* 4.5 (Oct. 2014), pp. 562–567. DOI: 10.9734/IRJPAC/2014/8704.

[90] Steven J Ruuth and Barry Merriman. “A simple embedding method for solving partial differential equations on surfaces”. In: *Journal of Computational Physics* 227.3 (Jan. 2008), pp. 1943–1961. DOI: 10.1016/j.jcp.2007.10.009.

[91] Colin B. MacDonald and Steven J Ruuth. “Level set equations on surfaces via the closest point method”. In: *Journal of Scientific Computing* 35.2-3 (Mar. 2008), pp. 219–240. DOI: 10.1007/s10915-008-9196-6.

[92] Colin B Macdonald. “The Closest Point Method for Time-dependent Processes on Surfaces”. PhD thesis. Simon Fraser Univerisity, Aug. 2008.

[93] Colin B Macdonald, Barry Merriman, and Steven J Ruuth. “Simple computation of reaction-diffusion processes on point clouds.” In: *Proceedings of the National Academy of Sciences of the United States of America* 110.23 (June 2013), pp. 9209–14. DOI: 10.1073/pnas.1221408110.

[94] Aiden A Martin, Alan Bahm, James Bishop, Igor Aharonovich, and Milos Toth. “Dynamic Pattern Formation in Electron-Beam-Induced Etching”. In: *Physical Review Letters* 115.25 (Dec. 2015), p. 255501. DOI: 10.1103/PhysRevLett.115.255501.

[95] Milos Toth. “Advances in gas-mediated electron beam-induced etching and related material processing techniques”. In: *Applied Physics A: Materials Science and Processing* 117.4 (2014), pp. 1623–1629. DOI: 10.1007/s00339-014-8596-8.

[96] Aiden A Martin, Milos Toth, and Igor Aharonovich. “Subtractive 3D printing of optically active diamond structures.” In: *Scientific reports* 4 (2014), p. 5022. DOI: 10.1038/srep05022. arXiv: 1403.4067.

[97] J Britt Lassiter, Mark W Knight, Nikolay A Mirin, and Naomi J Halas. “Reshaping the plasmonic properties of an individual nanoparticle”. In: *Nano Letters* 9.12 (2009), pp. 4326–4332. DOI: 10.1021/nl9025665.

[98] John M Perry, Zachary D Harms, and Stephen C Jacobson. “3D Nanofluidic Channels Shaped by Electron-Beam-Induced Etching”. In: *Small* 8.10 (May 2012), pp. 1521–1526. DOI: 10.1002/smll.201102240.

[99] M. C. Cross and P. C. Hohenberg. “Pattern formation outside of equilibrium”. In: *Reviews of Modern Physics* 65.3 (July 1993), pp. 851–1112. DOI: 10.1103/RevModPhys.65.851.

[100] Shigeru Kondo and Takashi Miura. “Reaction-Diffusion Model as a Framework for Understanding Biological Pattern Formation”. In: *Science* 329.September (2010), pp. 1616–1620. DOI: 10.1126/science.1179047.

[101] A Lehmann, C Bradac, and R P Mildren. “Two-photon polarization-selective etching of emergent nano-structures on diamond surfaces.” In: *Nature communications* 5 (2014), p. 3341. DOI: 10.1038/ncomms4341.

[102] Milos Toth, Charlene Lobo, Vinzenz Friedli, Aleksandra Szkudlarek, and Ivo Utke. “Continuum models of focused electron beam induced processing”. In: *Beilstein Journal of Nanotechnology* 6.1 (2015), pp. 1518–1540. DOI: 10.3762/bjnano.6.157.

[103] Aiden A Martin and Milos Toth. “Cryogenic electron beam induced chemical etching.” In: *ACS applied materials and interfaces* 6.21 (Nov. 2014), pp. 18457–60. DOI: 10.1021/am506163w.

[104] F J Schoenaker, R Córdoba, R Fernández-Pacheco, C Magén, O Stéphan, C Zuriaga-Monroy, M R Ibarra, and J M De Teresa. “Focused electron beam induced etching of titanium with XeF$_2$.” In: *Nanotechnology* 22.26 (May 2011), p. 265304. DOI: 10.1088/0957-4484/22/26/265304.

[105] N Vanhove, P Lievens, and W Vandervorst. “Electron beam induced etching of silicon with SF$_6$”. In: *Journal of Vacuum Science and Technology B: Microelectronics and Nanometer Structures* 28.6 (2010), p. 1206. DOI: 10.1116/1.3504594.

[106] Hiroyuki Miyazoe, Ivo Utke, Johann Michler, and Kazuo Terashima. “Controlled focused electron beam-induced etching for the fabrication of sub-beam-size nanoholes”. In: *Applied Physics Letters* 92.4 (2008), p. 43124. DOI: 10.1063/1.2839334.

[107] Matthew G Lassiter and Philip D Rack. “Nanoscale electron beam induced etching: a continuum model that correlates the etch profile to the experimental parameters.” In: *Nanotechnology* 19.45 (Oct. 2008), p. 455306. DOI: 10.1088/0957-4484/19/45/455306.

[108] Young R Choi, Philip D Rack, Bernhard Frost, and David C Joy. “Effect of electron beam-induced deposition and etching under bias”. In: *Scanning* 29.4 (2007), pp. 171–176. DOI: 10.1002/sca.20060.

[109] P D Rack, S Randolph, Y Deng, J Fowlkes, Y Choi, and D C Joy. “Nanoscale electron-beam-stimulated processing”. In: *Applied Physics Letters* 82.14 (2003), pp. 2326–2328. DOI: 10.1063/1.1565696.

[110] Jun Taniguchi, Iwao Miyamoto, Naoto Ohno, Ken’ichi Kantani, Masanori Komuro, and Hiroshi Hiroshima. “Electron Beam Assisted Chemical Etching of Single-Crystal Diamond Substrates with Hydrogen Gas”. In: *Japanese Journal of Applied Physics* 36.Part 1, No. 12B (Dec. 1997), pp. 7691–7695. DOI: 10.1143/JJAP.36.7691.

[111] H Fujioka, K Nakamae, M Hirota, K Ura, N Tamura, and T Takagi. “Measurements of the energy dependence of electron beam assisted etching of, and deposition on, silica”. In: *Journal of Physics D: Applied Physics* 23.2 (Feb. 1990), pp. 266–268. DOI: 10.1088/0022-3727/23/2/023.

[112] Ruth Klauser, Jin-Ming Chen, T.J. Chuang, L.M. Chen, M.C. Shih, and J.-C. Lin. “The interaction of oxygen and hydrogen on a diamond C(111) surface: a synchrotron radiation photoemission, LEED and AES study”. In: *Surface Science* 356.1-3 (June 1996), pp. L410–L416. DOI: 10.1016/0039-6028(96)00673-5.

[113] M Frenklach, D Huang, R E Thomas, R A Rudder, and R J Markunas. “Activation energy and mechanism of CO desorption from (100) diamond surface”. In: *Applied Physics Letters* 63.22 (1993), pp. 3090–3092. DOI: 10.1063/1.110217.

[114] Zeev Shpilman, Irina Gouzman, Eitan Grossman, Linhan Shen, Timothy K Minton, Jeffrey T Paci, George C Schatz, Rozalia Akhvlediani, and Alon Hoffman. “Oxidation and etching of CVD diamond by thermal and hyperthermal atomic oxygen”. In: *Journal of Physical Chemistry C* 114.44 (2010), pp. 18996–19003. DOI: 10.1021/jp1073208.

[115] Paolo Olivero, Sergey Rubanov, Patrick Reichart, Brant C Gibson, Shane T Huntington, James Rabeau, Andrew D Greentree, Joseph Salzman, David Moore, David N Jamieson, and Steven Prawer. “Ion-beam-assisted lift-off technique for three-dimensional micromachining of freestanding single-crystal diamond”. In: *Advanced Materials* 17.20 (2005), pp. 2427–2430. DOI: 10.1002/adma.200500752.

[116] J Schwartz, S Aloni, D F Ogletree, and T Schenkel. “Effects of low-energy electron irradiation on formation of nitrogen–vacancy centers in single-crystal diamond”. In: *New Journal of Physics* 14.4 (Apr. 2012), p. 043024. DOI: 10.1088/1367-2630/14/4/043024.

[117] Aiden A Martin, Steven Randolph, Aurelien Botman, Milos Toth, and Igor Aharonovich. “Maskless milling of diamond by a focused oxygen ion beam”. In: *Scientific Reports* 5 (2015), p. 8958. DOI: 10.1038/srep08958.

[118] Aiden A Martin, Matthew R Phillips, and Milos Toth. “Dynamic surface site activation: A rate limiting process in electron beam induced etching”. In: *ACS Applied Materials and Interfaces* 5.16 (Aug. 2013), pp. 8002–8007. DOI: 10.1021/am402083n.

[119] Chunming Li, Rui Huang, Zhaohua Ding, J Chris Gatenby, Dimitris N Metaxas, and John C Gore. “A level set method for image segmentation in the presence of intensity inhomogeneities with application to MRI”. In: *IEEE Transactions on Image Processing* 20.7 (July 2011), pp. 2007–2016. DOI: 10.1109/TIP.2011.2146190.

[120] Martin Wo. “Numerical modeling of multiphase flows in microfluidics and micro process engineering : a review of methods and applications”. In: *Microfluid Nanofluid* 12.6 (Mar. 2012), pp. 841–886. DOI: 10.1007/s10404-012-0940-8.

[121] Mark Sussman, Peter Smereka, and Stanley Osher. “A Level Set Approach for Computing Solutions to Incompressible Two-Phase Flow”. In: *Journal of Computational Physics* 114.1 (Sept. 1994), pp. 146–159. DOI: 10.1006/jcph.1994.1155.

[122] Li Wang, Chunming Li, Quansen Sun, Deshen Xia, and Chiu-Yen Kao. “Computerized Medical Imaging and Graphics Active contours driven by local and global intensity fitting energy with application to brain MR image segmentation”. In: *Computerized Medical Imaging and Graphics* 33.7 (Oct. 2009), pp. 520–531. DOI: 10.1016/j.compmedimag.2009.04.010.

[123] Frank Losasso, Frédéric Gibou, and Ron Fedkiw. “Simulating water and smoke with an octree data structure”. In: *ACM Transactions on Graphics* 23.3 (2004), p. 457. DOI: 10.1145/1015706.1015745.

[124] Xiao-Feng Wang, De-Shuang Huang, and Huan Xu. “An efficient local Chan-Vese model for image segmentation”. In: *Pattern Recognition* 43.3 (Mar. 2010), pp. 603–618. DOI: 10.1016/j.patcog.2009.08.002.

[125] Ethan S Brown, Tony F Chan, and Xavier Bresson. “Completely convex formulation of the Chan-Vese image segmentation model”. In: *International Journal of Computer Vision* 98.1 (Oct. 2012), pp. 103–121. DOI: 10.1007/s11263-011-0499-y.

[126] C Ratsch and J A Venables. “Nucleation Theory and the Early Stages of Thin Film Growth”. In: *Journal of Vacuum Science and Technology A* 21.5 (2003), S96–S109. DOI: Doi10.1116/1.1600454.

[127] Peter Smereka, Xingquan Li, Giovanni Russo, and D J Srolovitz. “Simulation of faceted film growth in three dimensions: Microstructure, morphology and texture”. In: *Acta Materialia* 53.4 (Feb. 2005), pp. 1191–1204. DOI: 10.1016/j.actamat.2004.11.013.

[128] James A Sethian and John Straint. “Crystal growth and dendritic solidification”. In: *Journal of Computational Physics* 98.2 (1992), pp. 231–253. DOI: 10.1016/0021-9991(92)90140-T.

[129] Giovanni Russo and Peter Smereka. “A Level-Set Method for the Evolution of Faceted Crystals”. In: *SIAM Journal on Scientific Computing* 21.6 (Jan. 2000), pp. 2073–2095. DOI: 10.1137/S1064827599351921.

[130] Colin Ophus, Erik Luber, and David Mitlin. “Simulations of faceted polycrystalline thin films: Asymptotic analysis”. In: *Acta Materialia* 57.5 (Mar. 2009), pp. 1327–1336. DOI: 10.1016/j.actamat.2008.11.014.

[131] Z.J. Liu, J Ouyang, W Zhou, and X.D. Wang. “Numerical simulation of the polymer crystallization during cooling stage by using level set method”. In: *Computational Materials Science* 97.C (Feb. 2015), pp. 245–253. DOI: 10.1016/j.commatsci.2014.10.038.

[132] Grégoire Allaire, François Jouve, and Anca-Maria Toader. “A level-set method for shape optimization”. In: *Comptes Rendus Mathematique* 334.12 (2002), pp. 1125–1130. DOI: 10.1016/S1631-073X(02)02412-3.

[133] Qi Xia, Tielin Shi, Shiyuan Liu, and Michael Yu Wang. “A level set solution to the stress-based structural shape and topology optimization”. In: *Computers and Structures* 90-91.C (Jan. 2012), pp. 55–64. DOI: 10.1016/j.compstruc.2011.10.009.

[134] Daniel Haley, Michael P Moody, and George D.W. Smith. “Level Set Methods for Modelling Field Evaporation in Atom Probe”. In: *Microscopy and Microanalysis* 19.06 (Aug. 2013), pp. 1709–1717. DOI: 10.1017/S1431927613013299.

[135] JA Sethian and David Adalsteinsson. “An overview of level set methods for etching, deposition, and lithography development”. In: *IEEE Transactions on Semiconductor Manufacturing* 10.1 (1997), pp. 167–184. DOI: 10.1109/66.554505.

[136] Heung-Bae Kim, Gerhard Hobler, Andreas Steiger, Alois Lugstein, and Emmerich Bertagnolli. “Full three-dimensional simulation of focused ion beam micro/nanofabrication”. In: *Nanotechnology* 18.245303 (May 2007), p. 245303.

[137] B. Radenovic, SJ Kim, and JK Lee. “3D etching profile evolution simulation using sparse field level set method”. In: *Arxiv preprint physics/0409130* 1 (Sept. 2004), pp. 3–6. arXiv: 0409130 [physics].

[138] B Radjenovic and J K Lee. “3D feature profile evolution simulation for SiO$_2$ etching in fluorocarbon plasma”. In: *Proc. 17 th ICPIG* 17 (2005), p. 142.

[139] Branislav Radjenović, Marija Radmilović-Radjenović, and Miodrag Mitrić. “Nonconvex Hamiltonians in three dimensional level set simulations of the wet etching of silicon”. In: *Applied Physics Letters* 89.21 (2006), p. 213102. DOI: 10.1063/1.2388860.

[140] Branislav Radjenović and Marija Radmilović-Radjenović. “Top down nano technologies in surface modification of materials”. In: *Central European Journal of Physics* 9.2 (Nov. 2011), pp. 19–24. DOI: 10.2478/s11534-010-0096-7.

[141] Branislav Radjenović, Marija Radmilović-Radjenović, and Miodrag Mitrić. *Level set approach to anisotropic wet etching of silicon.* May 2010. DOI: 10.3390/s100504950.

[142] Branislav Radjenović and Marija Radmilović-Radjenović. “An approach to the three-dimensional simulations of the Bosch process”. In: *Journal of Materials Research* 27.05 (Dec. 2012), pp. 793–798. DOI: 10.1557/jmr.2011.416.

[143] Branislav Radjenović and Marija Radmilović-Radjenović. “Application of the Level Set Method in Three-Dimensional Simulation of the Roughening and Smoothing of Substrates in Nanotechnologies”. In: *World Journal of Nano Science and Engineering* 04.02 (2014), pp. 84–89. DOI: 10.4236/wjnse.2014.42011.

[144] Alireza Sheikholeslami, Clemens Heitzinger, T Grasser, and Siegfried Selberherr. “Three-dimensional topography simulation for deposition and etching processes using a level set method”. In: *2004 24th International Conference on Microelectronics (IEEE Cat. No.04TH8716)*. Vol. 1. IEEE, 2004, pp. 241–244. DOI: 10.1109/ICMEL.2004.1314606.

[145] Alireza Sheikholeslami, F Parhami, R Heinzl, E Al-Ani, C Heitzinger, Fuad Badrieh, Helmut Puchner, T Grasser, and S Selberherr. “Applications of Three-Dimensional Topography Simulation in the Design of Interconnect Lines”. In: *2005 International Conference On Simulation of Semiconductor Processes and Devices*. IEEE, Dec. 2005, pp. 187–190. DOI: 10.1109/SISPAD.2005.201504.

[146] Alireza Sheikholeslami. “Topography Simulation of Deposition and Etching Processes”. PhD thesis. Technical University Vienna, 2006.

[147] Otmar Ertl, Clemens Heitzinger, and Siegfried Selberherr. “Efficient Coupling of Monte Carlo and Level Set Methods for Topography Simulation”. In: *Simulation of Semiconductor Processes and Devices 2007*. Vol. 12. September. Vienna: Springer Vienna, 2007, pp. 417–420. DOI: 10.1007/978-3-211-72861-1_101.

[148] Otmar Ertl and Siegfried Selberherr. “Three-dimensional topography simulation using advanced level set and ray tracing methods”. In: *2008 International Conference on Simulation of Semiconductor Processes and Devices* 3 (2008), pp. 3–6. DOI: 10.1109/SISPAD.2008.4648303.

[149] Otmar Ertl and Siegfried Selberherr. “A fast level set framework for large three-dimensional topography simulations”. In: *Computer Physics Communications* 180.8 (Aug. 2009), pp. 1242–1250. DOI: 10.1016/j.cpc.2009.02.002.

[150] Otmar Ertl and Siegfried Selberherr. “A Fast Void Detection Algorithm for Three-Dimensional Deposition Simulation”. In: *2009 International Conference on Simulation of Semiconductor Processes and Devices*. IEEE, Sept. 2009, pp. 1–4. DOI: 10.1109/SISPAD.2009.5290221.

[151] Jin Han, Hiwon Lee, Byung-Kwon Min, and Sang Jo Lee. “Prediction of nanopattern topography using two-dimensional focused ion beam milling with beam irradiation intervals”. In: *Microelectronic Engineering* 87.1 (Jan. 2010), pp. 1–9. DOI: 10.1016/j.mee.2009.05.010.

[152] Otmar Ertl. “Numerical Methods for Topography Simulation”. PhD thesis. Technical University Vienna, 2010.

[153] Otmar Ertl, Lado Filipovic, and Siegfried Selberherr. “Three-dimensional simulation of focused ion beam processing using the level set method”. In: *2010 International Conference on Simulation of Semiconductor Processes and Devices*. 3. IEEE, Sept. 2010, pp. 49–52. DOI: 10.1109/SISPAD.2010.5604573.

[154] Xiao-Qian Li, Zai-Fa Zhou, Wei-Hua Li, and Qing-An Huang. “Three-dimensional modeling and simulation of the Bosch process with the level set method”. In: *IEEE SENSORS 2014 Proceedings*. c. IEEE, Nov. 2014, pp. 570–573. DOI: 10.1109/ICSENS.2014.6985062.

[155] N I Borgardt, R L Volkov, A V Rumyantsev, and Yu A Chaplygin. “Simulation of material sputtering with a focused ion beam”. In: *Technical Physics Letters* 41.6 (July 2015), pp. 610–613. DOI: 10.1134/S106378501506019X.

[156] J.A Sethian. “Tracking Interfaces with Level Sets: An “act of violence” helps solve evolving interface problems in geometry, fluid mechanics, robotic navigation and materials sciences”. In: *American Scientist* 85 (1997), p. 10.

[157] M.G. Crandall and P.L. Lions. “Viscosity solutions of Hamilton-Jacobi equations”. In: *Transactions of the American Mathematical Society* 277.1 (1983), pp. 1–42. DOI: 10.1090/S0002-9947-1983-0690039-8.

[158] M G Crandall and P.L. Lions. “Two approximations of solutions of Hamilton-Jacobi equations”. In: *Mathematics of Computation* 43.167 (1984), pp. 1–1. DOI: 10.1090/S0025-5718-1984-0744921-8.

[159] Michael Bang Nielsen. “Efficient and High Resolution Level Set Simulations”. PhD thesis. University of Aarhus, Aug. 2006.

[160] David Adalsteinsson and J.A Sethian. “The Fast Construction of Extension Velocities in Level Set Methods”. In: *Journal of Computational Physics* 148.1 (Jan. 1999), pp. 2–22. DOI: 10.1006/jcph.1998.6090.

[161] Branislav Radjenović and Alan Bahm. “email with Branislov Radjenovic”. 2014.

[162] Sigal Gottlieb, David Ketcheson, and Chi-Wang Shu. *Strong Stability Preserving Runge-Kutta and Multistep Time Discretizations*. WORLD SCIENTIFIC, Jan. 2011, p. 176. DOI: 10.1142/7498.

[163] Ross Whitaker. “A level-set approach to 3D reconstruction from range data”. In: *Intl. J. of Comp. Vision* 29.3 (1998), pp. 203–231. DOI: 10.1023/A:1008036829907.

[164] Ross T Whitaker. “Isosurfaces and level-sets”. In: *Visualization Handbook*. Elsevier Inc., 2005, pp. 97–123. DOI: 10.1016/B978-012387582-2/50008-3.

[165] Ross T Whitaker and Josh Cates. *VISPACK*. May 2015.

[166] James A Sethian. “Fast Marching Methods”. In: *SIAM Review* 41.2 (1999), pp. 199–235. DOI: 10.1137/S0036144598347059.

[167] Hongkai Zhao. “A fast sweeping method for Eikonal equations”. In: *Mathematics of Computation* 74.250 (May 2004), pp. 603–628. DOI: 10.1090/S0025-5718-04-01678-3.

[168] David F Richards, Max O Bloomfield, Suchira Sen, and Timothy S Cale. “Extension velocities for level set based surface profile evolution”. In: *Journal of Vacuum Science and Technology A: Vacuum, Surfaces, and Films* 19.4 (2001), p. 1630. DOI: 10.1116/1.1380230.

[169] D. Chopp. “Another Look at Velocity Extensions in the Level Set Method”. In: *SIAM Journal on Scientific Computing* 31.5 (Jan. 2009), pp. 3255–3273. DOI: 10.1137/070686329.

[170] David L Chopp and Alan Bahm. “email with David Chopp”. Dec. 2014.

[171] Danping Peng, Barry Merriman, Stanley Osher, Hongkai Zhao, and Myungjoo Kang. “A PDE-Based Fast Local Level Set Method”. In: *Journal of Computational Physics* 155.2 (Nov. 1999), pp. 410–438. DOI: 10.1006/jcph.1999.6345.

[172] Ian M Mitchell. “The Flexible, Extensible and Efficient Toolbox of Level Set Methods”. In: *Journal of Scientific Computing* 35.2-3 (June 2008), pp. 300–329. DOI: 10.1007/s10915-007-9174-4.

[173] Ian M Mitchell and Alan Bahm. “email with Ian Mitchell”. Apr. 2015.

[174] H J Johnson, Matthew M McCormick, and Luis Ibanez. *The ITK Software Guide Book 1: Introduction and Development Guidelines Fourth Edition Updated for ITK version 4.7*. 4.7. Feb. 2015.

[175] James A Sethian. “A fast marching level set method for monotonically advancing fronts.” In: *Proceedings of the National Academy of Sciences of the United States of America* 93.4 (1996), pp. 1591–1595. DOI: 10.1073/pnas.93.4.1591.

[176] D. Adalsteinsson and J.A. Sethian. “A Level Set Approach to a Unified Model for Etching, Deposition, and Lithography II: Three-Dimensional Simulations”. In: *Journal of Computational Physics* 122.2 (Dec. 1995), pp. 348–366. DOI: 10.1006/jcph.1995.1221.

[177] D. Adalsteinsson and J.A. Sethian. “A Level Set Approach to a Unified Model for Etching, Deposition, and Lithography”. In: *Journal of Computational Physics* 138.1 (Nov. 1997), pp. 193–223. DOI: 10.1006/jcph.1997.5817.

[178] Keshra Sangwal, S Amelinckx, and J Nihoul. *Etching of crystals. Theory, experiment, and application*. Ed. by S Amelinckx and J Nihoul. Institute of Physics Technical University of Lodz, 1987. DOI: 10.1002/bbpc.19870911149.

[179] Utkarsh Ayachit, Berk Geveci, Kenneth Moreland, John Patchett, and Jim Ahrens. “The ParaView Visualization Application”. In: Kitware, Inc., Nov. 2012. DOI: 10.1201/b12985-23.

[180] Philip Martineau, Mike Gaukroger, Riz Khan, and Dave Evans. “Effect of steps on dislocations in CVD diamond grown on {001} substrates”. In: *physica status solidi (c)* 6.8 (Aug. 2009), pp. 1953–1957. DOI: 10.1002/pssc.200881465.

[181] Gerhard Dziuk and Charles M Elliott. “Finite element methods for surface PDEs”. In: *Acta Numerica* 22 (May 2013), pp. 289–396. DOI: 10.1017/S0962492913000056.

[182] A Madzvamuse and R Barreira. “Exhibiting cross-diffusion-induced patterns for reaction-diffusion systems on evolving domains and surfaces”. In: *Physical Review E - Statistical, Nonlinear, and Soft Matter Physics* 90.4 (Oct. 2014), p. 43307. DOI: 10.1103/PhysRevE.90.043307.

[183] Andreas Dedner and Pravin Madhavan. “Adaptive discontinuous Galerkin methods on surfaces”. In: *Numerische Mathematik* 132.2 (Feb. 2016), pp. 369–398. DOI: 10.1007/s00211-015-0719-4.

[184] Vít Dolejší and Miloslav Feistauer. “Inviscid Compressible Flow”. In: Springer Series in Computational Mathematics. Cham, Switzerland: Springer, Jan. 2015, pp. 401–475. DOI: 10.1007/978-3-319-19267-3_8.

[185] Marcelo Bertalmio, Li-Tien Cheng, Stanley Osher, and Guillermo Sapiro. “Variational Problems and Partial Differential Equations on Implicit Surfaces”. In: *Journal of Computational Physics* 174.2 (Dec. 2001), pp. 759–780. DOI: 10.1006/jcph.2001.6937.

[186] S Chen, B Merriman, S Osher, and P Smereka. “A Simple Level Set Method for Solving Stefan Problems”. In: *Journal of Computational Physics* 135.1 (1997), pp. 8–29. DOI: 10.1006/jcph.1997.5721.

[187] John B Greer. “An improvement of a recent Eulerian method for solving PDEs on general geometries”. In: *Journal of Scientific Computing* 29.3 (Dec. 2006), pp. 321–352. DOI: 10.1007/s10915-005-9012-5.

[188] Colin B Macdonald and Steven J Ruuth. “The Implicit Closest Point Method for the Numerical Solution of Partial Differential Equations on Surfaces”. In: *SIAM Journal on Scientific Computing* 31.6 (Jan. 2009), p. 4330. DOI: 10.1137/080740003.

[189] Mark Kim and Charles Hansen. “Surface flow visualization using the closest point embedding”. In: *2015 IEEE Pacific Visualization Symposium (PacificVis)*. IEEE, Apr. 2015, pp. 17–23. DOI: 10.1109/PACIFICVIS.2015.7156351.

[190] Harry Biddle, Ingrid von Glehn, Colin B Macdonald, and Thomas Marz. “A volume-based method for denoising on curved surfaces”. In: *2013 IEEE International Conference on Image Processing*. IEEE, Sept. 2013, pp. 529–533. DOI: 10.1109/ICIP.2013.6738109.

[191] Emma Naden, Thomas März, and Colin B Macdonald. “Anisotropic Diffusion on Curved Surfaces”. In: *arXiv* (Mar. 2014). arXiv: 1403.2131.

[192] Li Tian, Colin B Macdonald, and Steven J. Ruuth. “Segmentation on surfaces with the Closest Point Method”. In: *2009 16th IEEE International Conference on Image Processing (ICIP)*. IEEE, Nov. 2009, pp. 3009–3012. DOI: 10.1109/ICIP.2009.5414447.

[193] T A März. “The Closest Point Method for Surfaces PDEs and Applications to Thin Film Flow”. In: *14th International Conference on Hyperbolic Problems: Theory, Numerics, Applications*. Padova, Italy, June 2012.

[194] Ebrahim M Kolahdouz and David Salac. “A numerical model for the trans-membrane voltage of vesicles”. In: *Applied Mathematics Letters* 39 (Jan. 2015), pp. 7–12. DOI: 10.1016/j.aml.2014.08.001.

[195] D Salac and M Miksis. “A level set projection model of lipid vesicles in general flows”. In: *Journal of Computational Physics* 230.22 (Sept. 2011), pp. 8192–8215. DOI: 10.1016/j.jcp.2011.07.019.

[196] Ebrahim M Kolahdouz and David Salac. “Electrohydrodynamics of Three-Dimensional Vesicles: A Numerical Approach”. In: *SIAM Journal on Scientific Computing* 37.3 (Jan. 2015), B473–B494. DOI: 10.1137/140988966.

[197] Ingrid von Glehn, Thomas März, and Colin B Macdonald. “An embedded method-of-lines approach to solving partial differential equations on surfaces”. In: *arXiv* (July 2013), pp. 1–19. arXiv: 1307.5657.

[198] Yujia Chen and Colin B Macdonald. “The Closest Point Method and Multigrid Solvers for Elliptic Equations on Surfaces”. In: *SIAM Journal on Scientific Computing* 37.1 (Jan. 2015), A134–A155. DOI: 10.1137/130929497.

[199] Edward J Fuselier and Grady B Wright. “A High-Order Kernel Method for Diffusion and Reaction-Diffusion Equations on Surfaces”. In: *Journal of Scientific Computing* 56.3 (Sept. 2013), pp. 535–565. DOI: 10.1007/s10915-013-9688-x.

[200] S Auer, C. B. MacDonald, M Treib, J Schneider, and R Westermann. “Real-time fluid effects on surfaces using the closest point method”. In: *Computer Graphics Forum* 31.6 (May 2012), pp. 1909–1923. DOI: 10.1111/j.1467-8659.2012.03071.x.

[201] Yujia Chen. “Surface Computing”. In: *Oriel CBL course*. University of Oxford. Oxford, Aug. 2014, pp. 1–43.

[202] Jeff Bezanson, Stefan Karpinski, Viral B Shah, and Alan Edelman. “Julia: A Fast Dynamic Language for Technical Computing”. In: *arXiv:1209.5145* (Sept. 2012), pp. 1–27. arXiv: 1209.5145.

[203] Yong Gang Li, Yang Yang, Michael P. Short, Ze Jun Ding, Zhi Zeng, and Ju Li. “IM3D: A parallel Monte Carlo code for efficient simulations of primary radiation displacements and damage in 3D geometry”. In: *Scientific Reports* 5 (Dec. 2015), p. 18130. DOI: 10.1038/srep18130.

[204] J F Ziegler, J P Biersack, and M D Ziegler. *SRIM: The Stopping and Range of Ions in Matter*. 7th ed. SRIM Co., Mar. 2008.

[205] Michael Nastasi and James W Mayer. *Ion Implantation and Synthesis of Materials*. Vol. 80. Berlin, Heidelberg: Springer Berlin Heidelberg, 2006, p. 277. DOI: 10.1007/978-3-540-45298-0.

[206] Wolfgang Eckstein and Herbert M Urbassek. “Computer Simulation of the Sputtering Process”. In: *Sputtering by Particle Bombardment*. Berlin, Heidelberg: Springer Berlin Heidelberg, Jan. 2007, pp. 21–31. DOI: 10.1007/978-3-540-44502-9_2.

[207] Niels Bohr. “II. On the theory of the decrease of velocity of moving electrified particles on passing through matter”. In: *Philosophical Magazine Series 6* 25.145 (Jan. 1913), pp. 10–31. DOI: 10.1080/14786440108634305.

[208] Wolfhard Möller. “Fundamentals of Ion-Surface Interaction”. In: *Fundamentals of Ion-Surface Interaction*. Technical University of Dresden. 2004.

[209] J Lindhard and M Scharff. “Energy dissipation by ions in the kev region”. In: *Physical Review* 124.1 (1961), pp. 128–130. DOI: 10.1103/PhysRev.124.128.

[210] Ordean S. Oen and Mark T. Robinson. “Computer studies of the reflection of light ions from solids”. In: *Nuclear Instruments and Methods* 132.C (1976), pp. 647–653. DOI: 10.1016/0029-554X(76)90806-5.

[211] James F. Ziegler, M.D. Ziegler, and J.P. Biersack. “SRIM - The stopping and range of ions in matter (2010)”. In: *Nuclear Instruments and Methods in Physics Research Section B: Beam Interactions with Materials and Atoms* 268.11-12 (June 2010), pp. 1818–1823. DOI: 10.1016/j.nimb.2010.02.091.

[212] Wolfgang Eckstein. *Computer Simulation of Ion-Solid Interactions*. Vol. 10. Springer Series in Materials Science. Berlin, Heidelberg: Springer Berlin Heidelberg, Jan. 1991. DOI: 10.1007/978-3-642-73513-4.

[213] Mark Robinson and Ian Torrens. “Computer simulation of atomic-displacement cascades in solids in the binary-collision approximation”. In: *Physical Review B* 9.12 (June 1974), pp. 5008–5024. DOI: 10.1103/PhysRevB.9.5008.

[214] Roger Smith. *Atomic and Ion Collisions in Solids and at Surfaces*. Ed. by Roger Smith. Cambridge: Cambridge University Press, 1997. DOI: 10.1017/CBO9780511524325.

[215] J.P. Biersack and L.G. Haggmark. “A Monte Carlo computer program for the transport of energetic ions in amorphous targets”. In: *Nuclear Instruments and Methods* 174.1-2 (Aug. 1980), pp. 257–269. DOI: 10.1016/0029-554X(80)90440-1.

[216] Andreas Mutzke, Ralf Schneider, Wolfgang Eckstein, and Renate Dohmen. *SDTrimSP Version 5.00 IPP Report 12/8*. Tech. rep. Max-Planck-Institut fur Plasmaphysik, 2011.

[217] Guido Van Rossum and Fred L Drake. “Python Tutorial”. In: *History* 42.4 (May 2010), pp. 1–122. DOI: 10.1111/j.1094-348X.2008.00203_7.x.

[218] John D Hunter. “Matplotlib: A 2D graphics environment”. In: *Computing in Science and Engineering* 9.3 (2007), pp. 99–104. DOI: 10.1109/MCSE.2007.55.

[219] Jeff Bezanson, Alan Edelman, Stefan Karpinski, and Viral B Shah. “Julia: A fresh approach to numerical computing”. In: *arXiv* (Nov. 2015), pp. 1–37. arXiv: arXiv:1411.1607v4.

[220] Daniel C Jones. *Gadfly.jl*. Dec. 2012.

[221] Klaus Wittmaack. “Reliability of a popular simulation code for predicting sputtering yields of solids and ranges of low-energy ions”. In: *Journal of Applied Physics* 96.5 (2004), p. 2632. DOI: 10.1063/1.1776318.

[222] R.E. Stoller, M.B. Toloczko, G.S. Was, A.G. Certain, S. Dwaraknath, and F.A. Garner. “On the use of SRIM for computing radiation damage exposure”. In: *Nuclear Instruments and Methods in Physics Research Section B: Beam Interactions with Materials and Atoms* 310 (Sept. 2013), pp. 75–80. DOI: 10.1016/j.nimb.2013.05.008.

[223] Maureen L. Nietiadi, Luis Sandoval, Herbert M. Urbassek, and Wolfhard Möller. “Sputtering of Si nanospheres”. In: *Physical Review B* 90.4 (July 2014), p. 045417. DOI: 10.1103/PhysRevB.90.045417.

[224] Herbert M. Urbassek, R. Mark Bradley, Maureen L. Nietiadi, and Wolfhard Möller. “Sputter yield of curved surfaces”. In: *Physical Review B* 91.16 (Apr. 2015), p. 165418. DOI: 10.1103/PhysRevB.91.165418.

[225] S. Lindsey and G. Hobler. “Sputtering of silicon at glancing incidence”. In: *Nuclear Instruments and Methods in Physics Research Section B: Beam Interactions with Materials and Atoms* 303 (May 2013), pp. 142–147. DOI: 10.1016/j.nimb.2012.12.087.

[226] R Ramachandra, BJ Griffin, and D Joy. “A Study of Helium Ion Induced Secondary Electron Emission”. In: *Microscopy and Microanalysis* 14.S2 (Aug. 2008), pp. 1192–1193. DOI: 10.1017/S1431927608081427.

[227] Ranjan Ramachandra. “A Study of Helium Ion Induced Secondary Electron Production”. PhD thesis. University of Tennessee - Knoxville, 2009.

[228] Daryl A Smith, David C Joy, and Philip D Rack. “Monte Carlo simulation of focused helium ion beam induced deposition.” In: *Nanotechnology* 21.17 (Apr. 2010), p. 175302. DOI: 10.1088/0957-4484/21/17/175302.

[229] C G Dupuy, D B Beach, J. E. Hurst, and Joseph M. Jasinski. “Laser induced deposition of copper from (triethylphosphine)cyclopentadienylcopper(I)”. In: *Chemistry of Materials* 1.1 (1989), pp. 16–18. DOI: 10.1021/cm00001a008.

[230] Nicholas A Roberts, Jason D Fowlkes, Gregory A Magel, and Philip D Rack. “Enhanced material purity and resolution via synchronized laser assisted electron beam induced deposition of platinum.” In: *Nanoscale* 5.1 (2013), pp. 408–15. DOI: 10.1039/c2nr33014h.

[231] Ilya I Tumkin, Vladimir A Kochemirovsky, Mikhail D Bal'makov, Sergey V Safonov, Elvira S Zhigley, Lev S Logunov, and Ekaterina V Shishkova. "Laser-induced deposition of nanostructured copper microwires on surfaces of composite materials". In: *Surface and Coatings Technology* 264.C (Feb. 2015), pp. 187–192. DOI: 10.1016/j.surfcoat.2014.09.030.

[232] Rainer Behrisch and Wolfgang Eckstein. "Sputtering by Particle Bombardment: Experiments and Computer Calculations from Theshold to MeV energies". In: *Topics in Applied Physics*. Vol. 110. Berlin/Heidelberg: Springer-Verlag, Jan. 2007, pp. 1–526. DOI: 10.1016/0030-3992(77)90116-5.

[233] T E Allen. "Monte Carlo calculation of low-energy electron emission from surfaces". In: *Journal of Vacuum Science and Technology B: Microelectronics and Nanometer Structures* 6.1988 (Nov. 1988), p. 2057. DOI: 10.1116/1.584111.

[234] Aurelien Botman. "Towards high purity nanostructures from electron beam induced deposition of platinum". PhD thesis. Delft University of Technology, Nov. 2009.

[235] A M Turing. "The Chemical Basis of Morphogenesis". In: *Philosophical Transactions of the Royal Society B: Biological Sciences* 237.641 (Aug. 1952), pp. 37–72. DOI: 10.1098/rstb.1952.0012.

[236] C. T. Rettner, D. J. Auerbach, J. C. Tully, and A. W. Kleyn. "Chemical Dynamics at the Gas-Surface Interface". In: *The Journal of Physical Chemistry* 100.31 (Jan. 1996), pp. 13021–13033. DOI: 10.1021/jp9536007.

[237] R Mark Bradley. "Redeposition of sputtered material is a nonlinear effect". In: *Physical Review B* 83.7 (Feb. 2011), p. 075404. DOI: 10.1103/PhysRevB.83.075404.

[238] R. C. Hefty, J. R. Holt, M. R. Tate, D. B. Gosalvez, M. F. Bertino, and S. T. Ceyer. "Dissociation of a product of a surface reaction in the gas phase: XeF$_2$ reaction with Si". In: *Physical Review Letters* 92.18 (May 2004), pp. 188302–1. DOI: 10.1103/PhysRevLett.92.188302.

[239] Jannik Meyer, Franz Eder, Simon Kurasch, Viera Skakalova, Jani Kotakoski, Hye Park, Siegmar Roth, Andrey Chuvilin, Sören Eyhusen, Gerd Benner, Arkady Krasheninnikov, and Ute Kaiser. "Accurate Measurement of Electron Beam Induced Displacement Cross

Sections for Single-Layer Graphene". In: *Physical Review Letters* 108.19 (May 2012), p. 196102. DOI: 10.1103/PhysRevLett.108.196102. arXiv: 1203.2372.

[240] Greg Wilson, D A Aruliah, C. Titus Brown, Neil P. Chue Hong, Matt Davis, Richard T. Guy, Steven H. D. Haddock, Kathryn D. Huff, Ian M. Mitchell, Mark D. Plumbley, Ben Waugh, Ethan P. White, and Paul Wilson. "Best Practices for Scientific Computing". In: *PLoS Biology* 12.1 (Jan. 2014). Ed. by Jonathan A. Eisen, e1001745. DOI: 10.1371/journal.pbio.1001745.

PhD theses only

[15] Heung-Bae Kim. “Design, simulation and fabrication of micro/nano functional structures using ion beams”. PhD thesis. Vienna University of Technology: Vienna University of Technology, Apr. 2007.

[32] Jared Craig Cullen. “Localised Probing of Precursor Coefficients Using Electron Beam Induced Deposition and Etching”. PhD thesis. University of Technology, Sydney, May 2015.

[92] Colin B Macdonald. “The Closest Point Method for Time-dependent Processes on Surfaces”. PhD thesis. Simon Fraser Univerisity, Aug. 2008.

[146] Alireza Sheikholeslami. “Topography Simulation of Deposition and Etching Processes”. PhD thesis. Technical University Vienna, 2006.

[152] Otmar Ertl. “Numerical Methods for Topography Simulation”. PhD thesis. Technical University Vienna, 2010.

[159] Michael Bang Nielsen. “Efficient and High Resolution Level Set Simulations”. PhD thesis. University of Aarhus, Aug. 2006.

[227] Ranjan Ramachandra. “A Study of Helium Ion Induced Secondary Electron Production”. PhD thesis. University of Tennessee - Knoxville, 2009.

[234] Aurelien Botman. “Towards high purity nanostructures from electron beam induced deposition of platinum”. PhD thesis. Delft University of Technology, Nov. 2009.

Books only

[40] Ivo Utke, Stanislav Moshkalev, and Phillip Russel. *Nanofabrication using focused ion and electron beams: principles and applications*. Oxford University Press, USA, 2012, p. 840.

[74] I Danaila, P Joly, S M Kaber, and M Postel. *An Introduction to Scientific Computing*. Ed. by Ionut Danaila, Pascal Joly, Sidi Mahmoud Kaber, and Marie Postel. New York, NY: Springer New York, Nov. 2007. DOI: 10.1007/978-0-387-49159-2.

[75] Richard Ghez. *Diffusion Phenomena*. Boston, MA: Springer US, 2001. DOI: 10.1007/978-1-4757-3361-7.

[80] James Albert Sethian. *Level Set Methods and Fast Marching Methods: Evolving Interfaces in Computational Geometry, Fluid Mechanics, Computer Vision, and Materials Science*. Cambridge university press, 1999.

[81] Stanley Osher and Ronald Fedkiw. *Level Set Methods and Dynamic Implicit Surfaces*. Applied Mathematical Sciences. New York: Springer, 2003, p. 273. DOI: 10.1007/b98879.

[162] Sigal Gottlieb, David Ketcheson, and Chi-Wang Shu. *Strong Stability Preserving Runge-Kutta and Multistep Time Discretizations*. WORLD SCIENTIFIC, Jan. 2011, p. 176. DOI: 10.1142/7498.

[174] H J Johnson, Matthew M McCormick, and Luis Ibanez. *The ITK Software Guide Book 1: Introduction and Development Guidelines Fourth Edition Updated for ITK version 4.7*. 4.7. Feb. 2015.

[204] J F Ziegler, J P Biersack, and M D Ziegler. *SRIM: The Stopping and Range of Ions in Matter*. 7th ed. SRIM Co., Mar. 2008.

[205] Michael Nastasi and James W Mayer. *Ion Implantation and Synthesis of Materials*. Vol. 80. Berlin, Heidelberg: Springer Berlin Heidelberg, 2006, p. 277. DOI: 10.1007/978-3-540-45298-0.

[212] Wolfgang Eckstein. *Computer Simulation of Ion-Solid Interactions*. Vol. 10. Springer Series in Materials Science. Berlin, Heidelberg: Springer Berlin Heidelberg, Jan. 1991. DOI: 10.1007/978-3-642-73513-4.

[214] Roger Smith. *Atomic and Ion Collisions in Solids and at Surfaces*. Ed. by Roger Smith. Cambridge: Cambridge University Press, 1997. DOI: 10.1017/CBO9780511524325.